HAL open science

Artificial arrays of magnetic nanostructures

Vojtech Schanilec

To cite this version:

Vojtech Schanilec. Artificial arrays of magnetic nanostructures. Physics [physics]. Université Grenoble Alpes [2020-..]; Brno University of Technology (MAIS), 2023. English. NNT : 2023GRALY033 . tel-04200041

HAL Id: tel-04200041

https://theses.hal.science/tel-04200041v1

Submitted on 8 Sep 2023

HAL is a multi-disciplinary open access archive for the deposit and dissemination of scientific research documents, whether they are published or not. The documents may come from teaching and research institutions in France or abroad, or from public or private research centers.

L'archive ouverte pluridisciplinaire **HAL**, est destinée au dépôt et à la diffusion de documents scientifiques de niveau recherche, publiés ou non, émanant des établissements d'enseignement et de recherche français ou étrangers, des laboratoires publics ou privés.

THÈSE

Pour obtenir le grade de

DOCTEUR DE L'UNIVERSITÉ GRENOBLE ALPES
et BRNO UNIVERSITY OF TECHNOLOGY

École doctorale: PHYS - Physique
Spécialité: Physique des matériaux
Unité de recherche: Institut Néel

Réseaux artificiels de nanostructures magnétiques

Artificial arrays of magnetic nanostructures

Présentée par:

Vojtěch SCHÁNILEC

Direction de thèse:

Nicolas ROUGEMAILLE DIRECTEUR DE RECHERCHE, CNRS – Institut Néel	Directeur de thèse
Tomáš ŠIKOLA DIRECTEUR DE RECHERCHE, CEITEC – Brno University of Technology	Co-Directeur de thèse

Rapporteurs:

Julian CARREY
PROFESSEUR, INSA Toulouse

Alexandra MOUGIN
DIRECTEUR DE RECHERCHE, CNRS - Université Paris-Saclay

Thèse soutenue publiquement le **12 mai 2023**, devant le jury composé de:

Julian CARREY PROFESSEUR, INSA Toulouse	Rapporteur
Alexandra MOUGIN DIRECTEUR DE RECHERCHE, CNRS – Université Paris-Saclay	Rapportrice
Jon Ander ARREGI URIBEETXEBARRIA DOCTEUR EN SCIENCES, CEITEC – Brno University of Technology	Examinateur
Aleš HRABEC DOCTEUR EN SCIENCES, ETH – Paul Scherrer Institut	Examinateur
Daniel LACOUR DIRECTEUR DE RECHERCHE, CNRS – Institut Jean Lamour	Examinateur
Elsa LHOTEL DIRECTEUR DE RECHERCHE, CNRS – Institut Néel	Présidente du jury
Laurent RANNO MAITRE DE CONFERENCES, Université Grenoble Alpes	Examinateur
Radimír VRBA PROFESSEUR, CEITEC – Brno University of Technology	Examinateur

BRNO UNIVERSITY OF TECHNOLOGY

VYSOKÉ UČENÍ TECHNICKÉ V BRNĚ

CENTRAL EUROPEAN INSTITUTE OF TECHNOLOGY BUT

STŘEDOEVROPSKÝ TECHNOLOGICKÝ INSTITUT VUT

ARTIFICIAL ARRAYS OF MAGNETIC NANOSTRUCTURES

UMĚLÉ USPOŘÁDANÉ SOUBORY MAGNETICKÝCH NANOSTRUKTUR

DOCTORAL THESIS

DIZERTAČNÍ PRÁCE

AUTHOR — Ing. Vojtěch Schánilec

AUTOR PRÁCE

SUPERVISOR — prof. RNDr. Tomáš Šikola, CSc.

ŠKOLITEL

SUPERVISOR — Dr. Nicolas Rougemaille

ŠKOLITEL

BRNO 2023

Abstract

Two-dimensional artificial arrays of interacting nanomagnets are a powerful playground for probing the physics of the lattice spin models. Artificially designed spin systems were introduced to mimic the behaviour of the frustrated pyrochlore crystals. Recent improvement in nano-fabrication techniques allows us to fabricate any desired artificial system in the lab control environment. Therefore artificial simulators of the matter can be produced and used for more advanced study of the desired phenomenons.

The advantage of using nanomagnetic objects as building blocks of artificial lattices is that small magnetic structures can effectively be considered giant classical Ising spins. Therefore elevating the problem of frustrated spins in pyrochlore crystals into such dimensions so the system can be studied with real space imaging techniques.

With imaging techniques such as magnetic force microscopy, the ordering of each Ising macrospin can be visualised in real space, enabling us to look not only at the global property of the system as a whole but to see how local interactions are accommodated.

Being able to fabricate artificial systems capturing the desired physics and comparing it to the real nature counterpart measures our understanding of the problem. It can also offer a missing piece of information. Furthermore, there are properties of the systems which are emergent and not encoded in the theoretical Hamiltonians describing the systems. Such properties seem to come out of nowhere, and with artificial systems and the ability to visualise these systems, we can analyse such properties.

This thesis focus on studying two types of systems: kagome and square dipolar spin systems. Both these systems are the results of the projections of the three-dimensional pyrochlore crystals into a plane. Moreover, both systems exhibit rather unusual behaviour, which is still to be measured on a large scale in real space. The dipolar kagome spin system has a low energy phase called *spin liquid 2*, which hosts unusual spin behaviour. The spins in this phase are ordered and disordered simultaneously, a unique emergent property of the system with no equivalent.

On the other hand, the square spin system is a perfect playground for studying the exotic physics of spin liquids, the Columb phase, and the behaviour of magnetic monopole-like quasi-particles.

The usual approach when fabricating artificial spin systems is to build them up out of single-domain nanomagnets which interact via long-range dipolar interactions. Therefore the systems try to minimise the interactions between all pairs of the Ising macrospins. However, the central idea of this thesis is to connect all the nanomagnets into one macro lattice, therefore introducing the micromagnetic effects into the systems. Magnetisation tries to satisfy the micromagnetic energies at the vertex site. Hence, we effectively replace the spin degree of freedom with a micromagnetic knob which can be used to tune each vertex's energy by introducing specially designed topological defects.

Even though both systems have been the focus of researchers for almost twenty years, we believe that our modifications open a gateway to fully accessing the exotic physic yet to uncover.

Résumé

Les réseaux artificiels bidimensionnels de nanoaimants en interaction sont un terrain de jeu puissant pour sonder la physique des modèles de spin du réseau. Des systèmes de spin artificiellement conçus ont été introduits pour imiter le comportement des cristaux de pyrochlore frustrés. L'amélioration récente des techniques de nano-fabrication nous permet de fabriquer n'importe quel système artificiel souhaité dans l'environnement de contrôle du laboratoire. Ainsi, des simulateurs artificiels de la matière peuvent être réalisés et utilisés pour une étude plus poussée du phénomène recherché.

L'avantage d'utiliser des objets nanomagnétiques comme blocs de construction de réseaux artificiels est que de petites structures magnétiques peuvent effectivement être considérées comme des spins d'Ising classiques géants. Par conséquent, élever le problème des spins frustrés dans les cristaux de pyrochlore à de telles dimensions afin que le système puisse être étudié avec des techniques d'imagerie spatiale réelle.

Avec des techniques d'imagerie telles que la microscopie à force magnétique, l'ordre de chaque macrospin d'Ising peut être visualisé dans l'espace réel, ce qui nous permet non seulement d'examiner la propriété globale du système dans son ensemble, mais aussi de voir comment les interactions locales sont adaptées.

Être capable de fabriquer des systèmes artificiels capturant la physique souhaitée et la comparant à la contrepartie réelle de la nature mesure notre compréhension du problème. Il peut également offrir une information manquante. De plus, certaines propriétés des systèmes sont émergentes et non codées dans les hamiltoniens théoriques décrivant les systèmes. De telles propriétés semblent sortir de nulle part, et avec des systèmes artificiels et la capacité de visualiser ces systèmes, nous pouvons analyser ces propriétés.

Cette thèse porte sur l'étude de deux types de systèmes : les systèmes de spin kagome et dipolaire carré. Ces deux systèmes sont le résultat des projections des cristaux tridimensionnels de pyrochlore dans un plan. De plus, les deux systèmes présentent un comportement assez inhabituel, qui reste à mesurer à grande échelle dans l'espace réel. Le système de spin dipolaire kagome a une phase à faible énergie appelée liquide de spin 2, qui héberge un comportement de spin inhabituel. Les spins de cette phase sont ordonnés et désordonnés simultanément, une propriété émergente unique du système sans équivalent.

D'autre part, le système de spin carré est un terrain de jeu parfait pour étudier la physique exotique des liquides de spin et de la phase de Columb et le comportement des quasi-particules magnétiques de type monopôle.

L'approche habituelle lors de la fabrication de systèmes de spin artificiels consiste à les construire à partir de nanoaimants à domaine unique qui interagissent via des interactions dipolaires à longue portée. Par conséquent, les systèmes tentent de minimiser les interactions entre toutes les paires de macrospins d'Ising. Cependant, l'idée centrale de cette thèse est de connecter tous les nanoaimants en un seul réseau macro, introduisant ainsi les effets micromagnétiques dans les systèmes. La magnétisation essaie de satisfaire les énergies micromagnétiques au site du vertex. Par conséquent, nous remplaçons efficacement le degré de liberté de spin par un bouton micromagnétique qui peut être utilisé pour régler l'énergie de chaque sommet en introduisant des défauts topologiques spécialement conçus.

Même si les deux systèmes sont au centre des préoccupations des chercheurs depuis près de vingt ans, nous pensons que nos modifications ouvrent une porte d'entrée pour accéder pleinement à la physique exotique encore à découvrir.

Abstrakt

Uměle vytvořená dvourozměrná pole interagujících nanomagnetů jsou mocným hřištěm pro zkoumání fyziky mřížkových spinových modelů. Tyto umělé spinové systémy byly navrženy tak, aby napodobovaly chování frustrovaných pyrochlorových krystalů. Zdokonalení nanofabrikačních technik nám umožňuje vyrobit jakýkoli požadovaný umělý systém v laboratorně kontrolovaném prostředí. Díky tomu lze vyrábět umělé simulátory hmoty a používat je k pokročilejšímu studiu požadovaných jevů.

Výhodou použití nanomagnetických objektů jako stavebních kamenů umělých mřížek je, že malé magnetické struktury lze efektivně považovat za obří klasické Isingovy spiny. Proto transformují problém frustrovaných spinů v pyrochlorových krystalech do takových rozměrů, aby bylo možné systém studovat pomocí zobrazovacích technik reálného prostoru.

Pomocí zobrazovacích technik, jako je mikroskopie magnetických sil, lze uspořádání každého Isingova makrospinu vizualizovat v reálném prostoru. To nám umožní podívat se nejen na globální vlastnost systému jako celku, ale také na to, jak jsou realizovány lokální interakce.

Schopnost vyrobit umělé systémy zachycující požadovaný fyzikální jev a porovnat jej s reálným přírodním protějškem ukazuje naše porozumění problému. Může také nabídnout chybějící část informací. Existují vlastnosti systémů, které nejsou zakódovány v teoretických Hamiltoniánech popisujících systémy, ale přesto jsou systému vlastní. Takové vlastnosti se zdánlivě objevují odnikud a díky umělým systémům a schopnosti tyto systémy vizualizovat můžeme takové vlastnosti analyzovat.

Tato práce se zaměřuje na studium dvou typů systémů: kagome a čtvercových dipolárních spinových systémů. Oba tyto systémy jsou výsledkem projekcí trojrozměrných pyrochlorových krystalů do roviny. Oba navíc vykazují poměrně neobvyklé chování, které je třeba teprve změřit v reálném prostoru ve velkých měřítcích. Dipolární kagome spinový systém má nízkoenergetickou fázi zvanou *spinová kapalina 2*. Spiny v této fázi jsou uspořádané a neuspořádané současně, což je jedinečná vlastnost systému, která nemá obdoby. Na druhé straně, čtvercový spinový systém je dokonalým hřištěm pro studium exotické fyziky spinových kapalin, Columbovy fáze a chování kvazičástic podobných magnetickým monopólům.

Obvyklý přístup při výrobě umělých spinových systémů spočívá v jejich sestavení z jednodoménových nanomagnetů, které interagují prostřednictvím dipolárních interakcí dlouhého dosahu. Systémy se proto snaží minimalizovat interakce mezi všemi páry Isingových makro-spinů. Ústřední myšlenkou této práce je však propojení všech nanomagnetů do jedné makromřížky, a tedy zavedení mikromagnetických efektů do systémů. Magnetizace se snaží uspokojit mikromagnetické energie v místě spojů. Proto účinně nahrazujeme spinový stupeň volnosti mikromagnetickým regulátorem, který lze použít k vyladění energie každého spoje zavedením speciálně navržených topologických defektů.

Přestože oba systémy jsou předmětem zájmu výzkumníků již téměř dvacet let, věříme, že naše modifikace otevírají bránu ke zkoumání exotické fyziky, kterou je třeba teprve odhalit.

Key words

Artificial spin systems, geometrical frustration, micromagnetism, kagome dipolar spin system, square spin system

Mots clés

Systèmes de spin artificiel, frustration géométrique, micromagnétisme, système de spin dipolaire kagome, système de spin carré

Klíčová slova

Umělé vytvořené spinové systémy, geometrická frustrace, mikromagnetismus, dipolární kagome spinový systém, čtvercový spinový systém

ACKNOWLEDGEMENT

First and foremost, I thank my supervisors, Nicolas Rougemaille and Tomáš Šikola. Without them, it would not be possible for me to start and, most importantly, to finish my PhD study. I cannot emphasise enough how important it was to learn from them and see how patently they were willing to teach me and support me on my way over the past years.

I would also like to extend my gratitude to all my colleagues from *Spin ice consortium* who helped me both with experiment and theory and contributed to the amazing atmosphere in every meeting or tea break. Nico, Benjamin, Johann, Lucien, Luca, Maria and Ondřej, if any of you ever pass through Brno, tea is at four. There is plenty of it. You are welcome anytime. Don't bother knocking.

There are plenty of amazing researchers and young scientists at the CEITEC Brno University of Technology; I would like to namely thank Lukáš, Jakub and Vojta for their support, without which the PhD would be much harder and sadder.

No words could describe how grateful I am to my beloved wife Gabča, my son Erwin and our Verča. Thank you all for being!

Last but not least, I want to express my gratitude to the French government, who granted me the co-tutelle scholarship through which all this was possible.

CzechNanoLab project LM2023051 funded by MEYS CR is gratefully acknowledged for the financial support of the measurements/sample fabrication at CEITEC Nano Research Infrastructure.

DECLARATION

The presented manuscript is the corrected version with the incorporated suggestion of all the defence committee members. Thank you for your advice and all your time with the manuscript.

I hereby declare that I have written my doctoral thesis on the theme of *Artificial arrays of magnetic nanostructures* independently, under the guidance of my thesis supervisors, Dr. Nicolas Rougemaille and prof. RNDr. Tomáš Šikola, CSc., using the technical literature and other sources of information which are all properly quoted in the thesis and detailed in the list of literature at the end of the thesis.

Vojtěch Schánilec

Contents

Chapter 1: Introduction **1**

1.1 Selected basics of micromagnetism . . . 1

1.1.1 Magnetic materials . . . 1

1.1.2 Micromagnetic energies and interactions . . . 3

1.2 Geometrical frustration . . . 5

1.3 From ice to artificial spin ice systems . . . 7

1.3.1 Ice . . . 8

1.3.2 Spin ice . . . 10

1.3.3 Artificial spin ice . . . 10

1.4 Artificial spin liquids . . . 13

1.5 Motivation and overview of the thesis . . . 14

Chapter 2: Methodology **16**

2.1 Simulation techniques . . . 16

2.1.1 Monte Carlo simulations . . . 17

2.1.2 MuMax^3 simulations . . . 17

2.2 Sample fabrication . . . 19

2.2.1 Electron beam lithography . . . 20

2.3 Sample demagnetisation . . . 25

2.4 Measurement and data analysis . . . 28

2.4.1 Magnetic force microscopy . . . 28

2.4.2 Acquiring qualitative data . . . 30

2.4.3 Acquiring quantitative data . . . 32

2.5 Overview of the experimental process . . . 37

Chapter 3: Artificial kagome spin system with notches **39**

3.1 Introduction to the kagome models . . . 39

3.1.1 Short range kagome models . . . 39

3.1.2 Long range kagome models . . . 42

3.2 Artificial realisation of kagome models . . . 45

3.3 Phases of the kagome dipolar spin ice . . . 47

3.4 Dynamical freezing . . . 54

3.5 Modified artificial kagome lattice with notches . . . 55

3.5.1 Magnetostatic effect of the notch 56
3.5.2 Imprinting the phases 57
3.5.3 Disadvantages of the notch presence 62
3.5.4 Breaking of the notch-rule 63
3.5.5 Monte Carlo simulations and the Hamiltonian of kagome spin system with notches 64
3.5.6 Notch-driven domain wall propagation 67
3.6 Discussion and concluding remarks 71

Chapter 4: Modified artificial square ice systems **73**
4.1 Introduction to the square vertex models 73
4.1.1 Sixteen vertex model 74
4.1.2 Six vertex model 75
4.2 Artificial realisation of square models 78
4.2.1 Presence of type III vertices 79
4.3 Tuning the coupling constant 80
4.3.1 Z-shifted square lattice 80
4.3.2 Square lattice with interaction modifiers 81
4.3.3 Square lattice with hole 82
4.4 Experimental realisation of the F model 86
4.4.1 Faraday lines 87
4.4.2 The experimental results 89
4.5 Discussion and concluding remarks 97

Chapter 5: Concluding remarks **99**

Reference list **102**

Appendices **109**
Appendix A - Mumax^3 simulation scripts 109
Appendix B - Fabrication procedure: lattice with holes 114
Appendix C - Type III vertex movement 115

List of abbreviations **116**

Chapter 1: Introduction

The main goal of this thesis is to provide a new point of view on artificial spin systems and how currently used design can be improved by implementing the micromagnetic effects.

For an easier understanding of our experiments, in this chapter, the selected basics of micromagnetism 1.1, and the principle of geometrical frustration 1.2, as well as the origin of artificial spin ice systems 1.3, will be summarised.

1.1. Selected basics of micromagnetism

In our experiments, we use artificially fabricated systems consisting of nanomagnetic structures interacting with each other to mimic the behaviour of natural materials that would be difficult or impossible to study otherwise. The key ingredient in our experiments is micromagnetism, hence the need to explain the classification of magnetic materials 1.1.1 and inner and external interactions 1.1.2.

1.1.1. Magnetic materials

Magnetic materials are classified by their magnetisation $\boldsymbol{M}$[1] response to the exposure of the external magnetic field $\boldsymbol{H}$.

Relation between $\boldsymbol{M}$ and $\boldsymbol{H}$ in the linear regime (i.e. for small fields) is given by the equation:

$$\boldsymbol{M} = \widehat{\chi} \cdot \boldsymbol{H}, \tag{1.1}$$

where $\widehat{\chi}$ is a dimensionless material parameter called *susceptibility tensor*. For isotropic materials, susceptibility is dimensionless constant χ.

Diamagnetism: Each material exposed to the external field shows signs of diamagnetic behaviour. This behaviour is caused by electrons orbiting around a nucleus in an atom. From classical physics, we know that if we put an electric loop[2] into the external field, it will induce a magnetic field aiming anti-parallel with the external field.

Magnetic susceptibility of diamagnetic materials can be derived from the perturbation theory [1], or by classical approach [2, 3]. Both methods lead to the same result:

$$\chi = -\frac{\mu_0 N e^2}{6 m_\mathrm{e}} \sum_i^Z \left\langle r_i^2 \right\rangle, \tag{1.2}$$

where μ_0 is vacuum permeability, m_e is mass of electron e, N is a number of electrons per unite volume and $\langle r_i^2 \rangle$ is given by electron distribution in the material. From equation 1.2, it is clear that χ is always negative, does not depend on temperature T nor external magnetic field H and therefore is constant for a given material.

Paramagnetism: Paramagnetic materials consist of small domains with a random distribution of magnetisation. Without the external field, the magnetisation of the paramagnet

[1] Magnetisation is defined as magnetic moment $\boldsymbol{\mu}$ per volume V.

[2] The electron orbiting the nucleus is the smallest electric loop.

is zero. If the paramagnet is exposed to the external field, the magnetisation of domains will align with the direction of the external field. The higher the field is, the more aligned the domains will be.

Susceptibility of paramagnet is described by *Curie's law* [1,4]:

$$\chi = \frac{C}{T}, \tag{1.3}$$

where C is always positive Curie constant - material constant and T is material temperature. It is evident from equation 1.3 that susceptibility χ will always be positive. With the rising temperature, the magnetisation of paramagnetic material will decrease.

Ferromagnetism: An example of magnetisation response to the external field of the ferromagnet is shown in Figure 1.1. At first, the magnetisation is zero because ferromagnetic materials are composed of small domains (indicated by coloured areas in Figure 1.1) with random magnetisation distribution. As the external field is applied, magnetic domains start to orient parallel to the external field, which leads to an increase of magnetisation as is shown by curve *ab* - this curve is called *the virgin curve*. Once magnetisation of all domains points in the direction of the external field, the ferromagnet reaches its *saturation* and maximum magnetic moment M_s. The field H_s needed to saturate the material is called the *saturation field*. As we decrease the strength of the external field, the magnetisation will evolve as curve *bcd* shows. In zero external field, the magnetisation will not be zero, but M_r - *magnetic remanence*. The domains are slightly misaligned but still point in the direction of the previously applied field. To nullify the magnetisation, the material needs to be exposed to *coercivity field* H_c with the opposite direction. As the strength of the applied field decreases, domains start to point in the direction of the field again to the point where the material is saturated but in the opposite direction. The curve *bcdeb* is called a hysteresis loop.

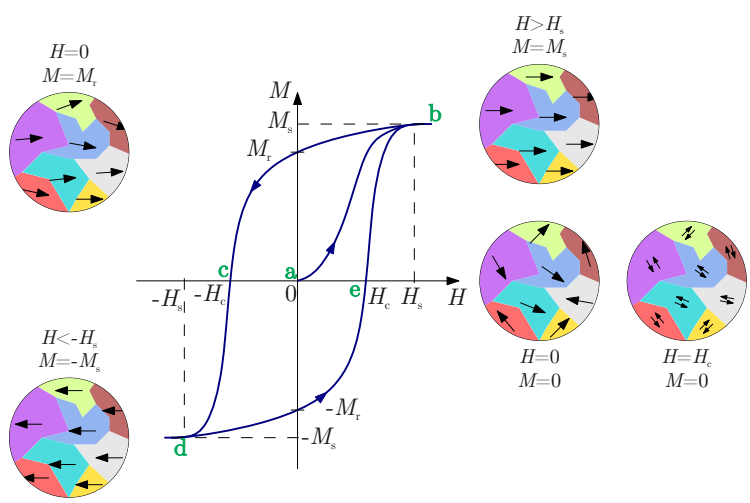

Figure 1.1: Virgin curve *ab* and hysteresis loop *bcdeb* of ferromagnetic material. Circles represent the schema of the orientation of ferromagnetic domains within the material at each given external field strength H with magnetisation M. For educational purpose this example was highly idealised.

If the ferromagnetic structure is fabricated small enough, their are so-called *single domain ferromagnet*, and the magnetisation will be uniform in the structure. The reasons why this phenomenon occurs are described in the following paragraphs.

1.1.2. Micromagnetic energies and interactions

Micromagnetism explores the competition between different energy types at characteristic lengths and scales.

This exploration can be done numerically or analytically, and in most cases, it is based on two assumptions [5]:

- Magnetisation M and other quantities are taken as continuous variables, and the discrete nature of the matter is ignored.
- The norm M_s of the magnetisation vector is taken as constant in any homogeneous matter.

Based on these assumptions, the magnetisation vector can be defined as:

$$\boldsymbol{M}_\mathbf{s}(\boldsymbol{r}) = M_\mathrm{s} \cdot \boldsymbol{m}(\boldsymbol{r}), \tag{1.4}$$

where $\boldsymbol{m}(\boldsymbol{r})$ is unite vector.

There are four basic magnetic energies: *Exchange, Demagnetizing field, Anisotropy* and *Zeeman* energy. The effect of each energy in the nanostructure can be seen in Figure 1.2, where is a schema of the nanomagnetic square and its domains as are all four energies implemented one by one. Each of these energies is discussed in further paragraphs.

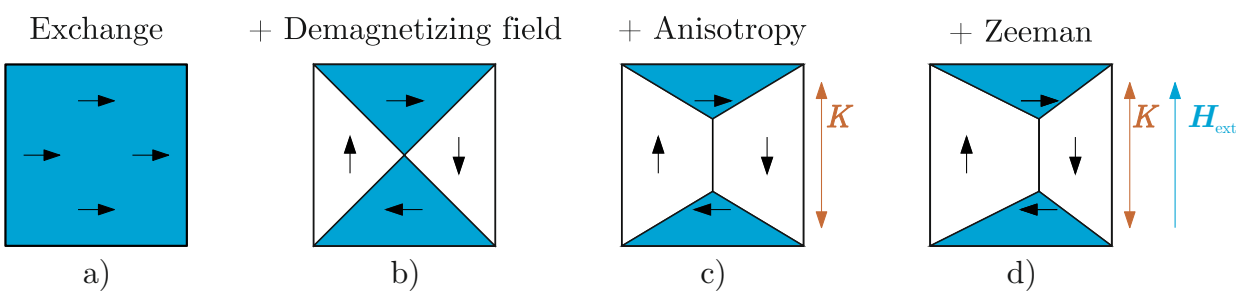

Figure 1.2: Magnetic energies on nanostructure applied one by one: a) Exchange, b) Demagnetisation field, c) Anisotropy, and d) Zeeman. Black arrows indicate magnetisation within the structure domains; brown arrows indicate the axis of anisotropy K; blue arrows show the vector of the applied external field $\boldsymbol{H}_\mathrm{ext}$.

Exchange energy: Exchange interaction Hamiltonian between spins can be described by the equation:

$$\mathcal{H}_\mathrm{exch} = -\frac{1}{2}\sum_{i,j}^{N} J_{ij}\boldsymbol{S}_i \cdot \boldsymbol{S}_j, \tag{1.5}$$

where $\boldsymbol{S}_i$ and $\boldsymbol{S}_j$ are spin vector, and J_{ij} is coupling constant. Suppose $J_{ij} > 0$ system minimizes the energy when its spins are ordered parallel, and such materials are called *ferromagnets*. If $J_{ij} < 0$, the system will have the lowest energy if all the first neighbour spins are anti-parallel, and such materials are called *antiferromagnets*. The origin of this interaction is a competition between The Coulomb force and The Pauli exclusion principle.

In the continuous limit, energy density can be written as:

$$\epsilon_{exch} = \frac{A_{exch}}{V} \iiint_{\Omega} \left[(\nabla M_{\mathrm{x}})^2 + (\nabla M_{\mathrm{y}})^2 + (\nabla M_{\mathrm{z}})^2 \right] \mathrm{d}V, \tag{1.6}$$

where A_{exch} is a material parameter *exchange stiffness*. If the ferromagnetic sample is small enough, the deciding energy is exchange energy. Therefore, all the moments will be oriented parallel, as seen in Figure 1.2 a).

Demagnetising field energy: Also called *dipolar energy*, or *magnetostatic energy* is long range dipolar interaction between magnetic moments in the matter. The density of demagnetising energy in the continuum is given by the equation:

$$\epsilon_{\mathrm{dem}} = -\frac{\mu_0}{2V} \iiint_{\Omega} \boldsymbol{M} \cdot \boldsymbol{H}_{\mathrm{dem}} \mathrm{d}V, \tag{1.7}$$

where $\boldsymbol{H}_{\mathrm{dem}}$ is demagnetisation field that can be calculated as $\boldsymbol{H}_{\mathrm{dem}} = -\hat{N}\boldsymbol{M}$. $\hat{N}$ is the demagnetisation tensor, and it is a specific parameter of the geometry of the sample. When magnetisation reaches a domain wall, either by meeting the edge of the sample or another domain, it must abruptly change. This effect leads to the creation of *surface* (green) or *volume* (red) charges, as can be seen in Figure 1.3. From these charges, the demagnetising field arises. In the mesoscale ferromagnetic sample, demagnetising energy competes with exchange energy. It can be energetically more efficient to transform from a single domain to a multi-domain state. This domain breakdown will increase exchange energy, but it decreases demagnetising energy. This effect is shown in Figure 1.3.

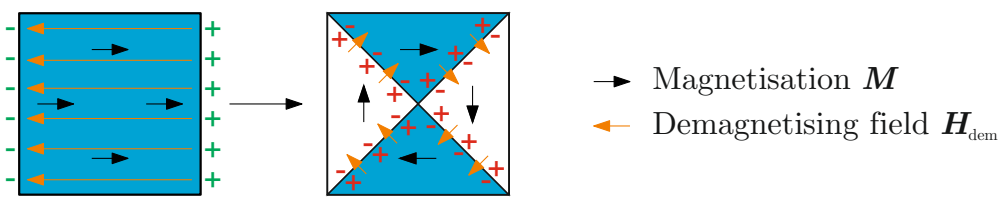

Figure 1.3: The transformation from a single domain to a multi-domain state. The demagnetising energy cost is lowered while the exchange energy increases. However, the total energy of the multi-domain state is lower than the single domain.

Anisotropy energy: In some magnetic materials, magnetisation prefers to aim along a preferential axis. This effect and the axis are called *anisotropy* and *axis of anisotropy*. The density of anisotropy energy is given by the formula:

$$\epsilon_{\mathrm{ani}} = K_{\mathrm{u1}} \sin^2\theta + K_{\mathrm{u2}} \sin^4\theta + \ldots, \tag{1.8}$$

where K_{u1} and K_{u2} are anisotropy constants and θ is an angle between magnetisation and the axis of anisotropy. If the $K_{\mathrm{u1}} > 0$, anisotropy energy is minimised if magnetisation points along the axis and the axis is therefore called *an easy axis*. If $K_{\mathrm{u1}} < 0$, the energy is minimised, if the magnetisation is perpendicular to the axis (thus defining *an easy plane*).

There are materials, e.g. $\mathrm{Ni_{80}Fe_{20}}$ (permalloy), where this energy does not arise because the ferromagnetic grains are oriented randomly, and there is no net anisotropy.

In Figure 1.2 c), the orientation anisotropy axis is indicated by axis K. Materials with anisotropy prefer domains that point their magnetisation along the axis.

Zeeman energy: When magnetic material is put inside the external field, the energy between M and H_{ext}, arises, and it is called Zeeman energy. Its density is described as:

$$\epsilon_{\text{z}} = -\frac{\mu_0}{V} \iiint_{\Omega} \boldsymbol{M} \cdot \boldsymbol{H}_{\text{ext}} \mathrm{d}V, \tag{1.9}$$

Because of the scalar product $\boldsymbol{M} \cdot \boldsymbol{H}_{\text{ext}}$ and the minus, the Zeeman energy is minimised if the magnetisation is oriented parallel to the external field.

In Figure 1.2 d), the effect of the Zeeman energy is shown. The domain with magnetisation parallel to the applied field expands, and the anti-parallel magnetisation orientation shrinks.

Total energy: Since energy is scalar, the total energy of the system is a sum of all energy contributions, and its density is therefore given by:

$$\epsilon_{\text{tot}} = \epsilon_{\text{exch}} + \epsilon_{\text{dem}} + \epsilon_{\text{ani}} + \epsilon_{\text{z}} \tag{1.10}$$

In our experiment, we use permalloy as magnetic material (a material where anisotropy can be neglected), and during measurement, there is no external applied field (no Zeeman energy). Therefore the total energy of our system is caused only by exchange interaction and demagnetising field.

1.2. Geometrical frustration

In condensed matter physics, the term *frustration* is used for the inability of a system to satisfy all interactions simultaneously. While trying to minimise the energy of some interactions, other interactions' energy will be maximised. This competition between systems interactions leads to many interesting physical phenomena, such as non-zero entropy of material at a very low temperature, highly degenerated ground states of a system, etc. The frustration caused by the system's geometry is called *geometrical frustration*.

For a system to be geometrically frustrated, it needs to have the right combination of geometry and interactions between its components. One of the most common examples of geometrically frustrated systems is a system consisting of Ising-like spins.[3] Experimentally, we can construct such a system by fabricating small nanoislands of magnetic materials. These nanoislands are single-domain ferromagnets, and their magnetic moment can point only up or down (in case of out-of-plane magnetisation). Let us consider two types of geometry with out-of-plane magnetisation, triangular and hexagonal, in combination with two types of interactions:

1. The first interaction can be called ferromagnetic (FM). Systems with this type of interaction minimize energy if all first neighbour has the same orientation.

2. The second interaction is called antiferromagnetic (AM). First neighbours of the systems have minimal energy if they have the opposite orientation.

[3] Ising-like spins can only be in one of two opposite states. In our schema, this is represented as two different colours: brown and tan.

The first combination of interactions and geometry we consider is FM within a) hexagonal and b) triangular lattice as shown in Figure 1.4. The lowest possible energy will be reached for both cases if all the first neighbour nanoislands (circles) have the same orientation (colour). These systems have two times degenerated ground state: all spins are brown or tan, but they are not frustrated since all interactions are satisfied.

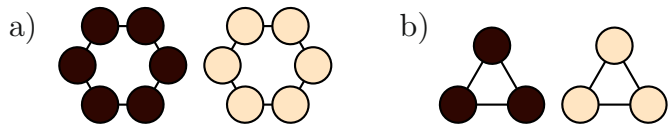

Figure 1.4: Schema of a) hexagonal and b) triangular lattices with ferromagnetic coupling between first neighbours. Both of these systems have two ground state configurations (all vertex brown or all tan).

The function of degeneration, which gives the number of the possible ground states, is directly linked to the entropy of the system[4]. For these systems in their ground state the function of degeneration is given by the expression:

$$g_{\text{hex,FM}} = g_{\text{tri,FM}} = 2, \tag{1.11}$$

and it can be seen that the degeneration function is not size dependent.

When switching from FM to AM interaction between the first neighbours, the system will have the lowest possible energy if the colour of neighbours alternates throughout the system. All AM interactions can be satisfied in the hexagonal geometry as seen in Figure 1.5 a), where both possible ground states are shown. Even if other hexagons are added to the system, the number of possible ground states will not change, and all the interactions can be satisfied, as seen in Figure 1.5 b).

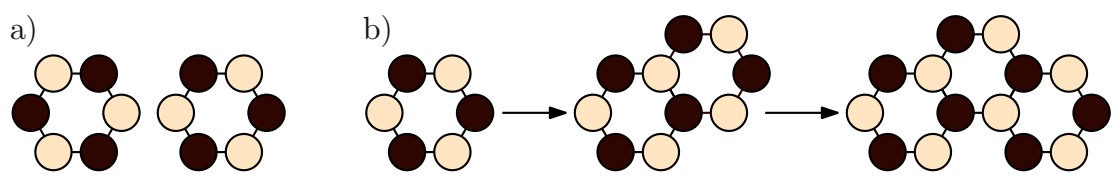

Figure 1.5: Schema of the hexagonal lattice with AF coupling between first neighbours. a) shows both possible ground states for the hexagonal lattice. Suppose another hexagon is added to the system, as is shown in b). In that case, its configuration is entirely determined by the previous system state; therefore, the number of possible ground states will not change.

As well as the hexagonal and triangular geometry with FM interactions, this system is not frustrated. Its function of degeneration is not depending on the size of the system and is given by:

$$g_{\text{hex,AM}} = 2. \tag{1.12}$$

On the other hand, if AM interactions are present in the triangle system, there is no way to satisfy all the interactions simultaneously, as shown in Figure 1.6 a). There are six

[4]Ludwig Boltzmann defined entropy as a thermodynamic quantity that indicates the degree of disorder of the system: The entropy $S(U, N)$ can be calculated from the function of degeneration $g(U, N)$ of the system with internal energy U and the number of particles N, using the following formula: $S(U, N) = k_{\text{B}} \ln g(U, N)$, where k_{B} is Boltzmann constant.

possible ground states, all of which have one interaction unsatisfied. Therefore the system is frustrated.

Difficulties arise as more triangles are added to the system. With the addition of one triangle to the string of triangles, another three possibilities of ground state emerge. The schema of this problem is shown in Figure 1.6 b).

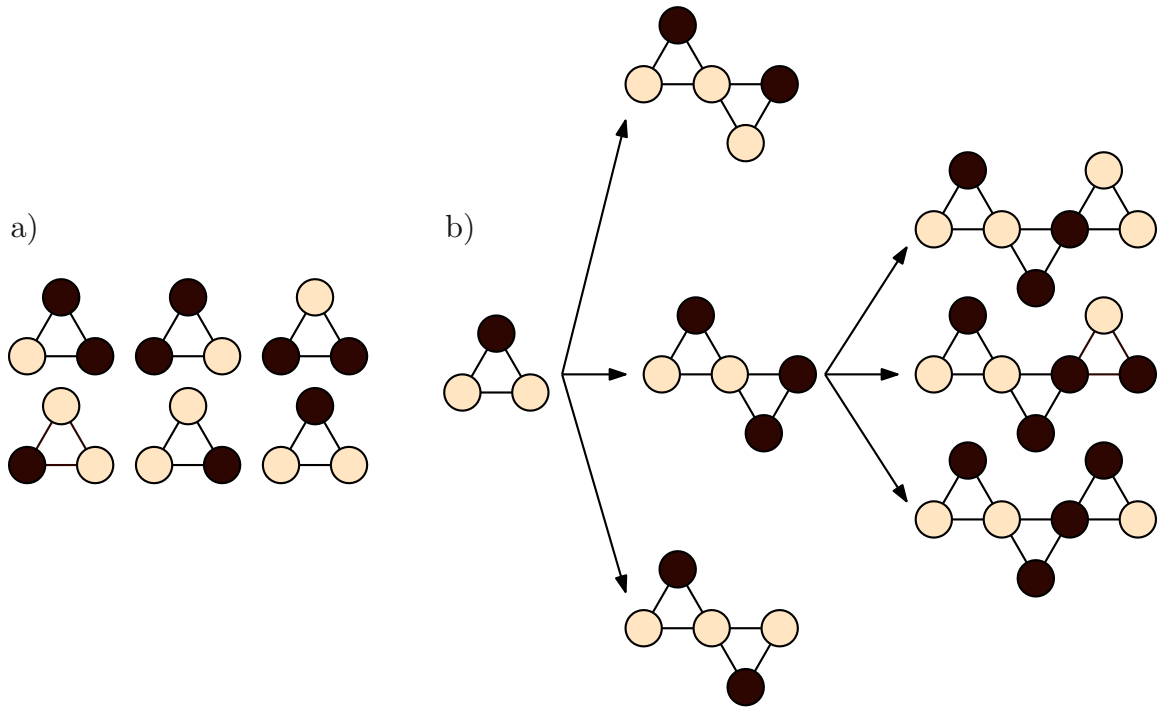

Figure 1.6: a) Six possible configurations of a triangle with AF interactions; all of these configurations have one interaction unsatisfied. b) With the addition of a triangle into this system, three more ground state configurations are possible.

The triangle string with AF interaction is highly frustrated, and the degeneration function can be calculated with the formula:

$$g_{\mathrm{tri,AM}} = 6 \cdot 3^{n-1}, \tag{1.13}$$

where n is the number of triangles in the system[5].

Our work mainly focuses on designing geometrically frustrated systems made from magnetically interacting nanomagnets. Even though we are researching artificially created systems, these systems mimic real nature systems' behaviour.

1.3. From ice to artificial spin ice systems

Artificial spin ice systems are now used to study magnetic frustration and other related phenomena. But the idea of using two-dimensional arrays of nanomagnets is relativity new. This section describes a brief evolution of artificial spin ice systems from their origin and relation to real natural materials such as water and magnetic pyrochlore crystals.

[5]This system is frustrated, and if such a triangle system has 172 cells, the number of possible ground states is larger than the number of atoms in the Universe.

The evolution started in the 1930s when strange behaviour and properties of frozen water were first observed [6, 7]. It was measured that even at low temperatures, the water still had non-zero residual entropy. It seems that this behaviour conflicts with the third law of thermodynamics [8]. Planck's interpretation of the law says: *When the temperature falls to absolute zero, the entropy of any pure crystalline substance tends to a universal constant (which can be taken to be zero).* It has been discovered that the water is actually geometrically frustrated with the function of degeneracy heavily dependent on the size of the system. The cause of the frustration will be discussed in section 1.3.1.

It has been discovered that many systems have similar properties and behaviour as frozen water. The magnetic equivalent was found in pyrochlore crystals such as $Ho_2Ti_2O_7$ and $Dy_2Ti_2O_7$. Both compounds belong to the large class of oxides $A_2B_2O_7$, where A is a rare-earth element and B is a non-magnetic transition metal. Pyrochlore crystals are perfect condensed matter examples of geometrical frustration due to their geometry and magnetic interaction, and they are discussed more in section 1.3.2. The main problem is that we cannot directly measure the spin degree of freedom. Also, a measurement of these crystals needs to be conducted at a low temperature.

Tanaka et al. [9, 10], and Wang et al. [11] published pioneering works on two-dimensional lithographically fabricated lattices composed of interacting nanomagnets. These artificially fabricated systems were designed to mimic the geometrical frustration of spin ice crystals, but with several advantages. Since the systems are no longer solid matter crystals but two-dimension lattices, it is possible to measure the orientation of every nanomagnet directly. That allows us to access both local and global information about the systems. Also, the nanomagnets were small enough to be single domain but large enough so their magnetisation reversal cannot be thermally activated, so the measurement could be done at room temperature [11]. These systems were named *artificial spin ices* and are described in section 1.3.3.

1.3.1. Ice

Water at low temperatures has a unique behaviour. Due to its geometry in the hexagonal phase and electrostatic interactions between hydrogen ions, water is a geometrically frustrated system.

Figure 1.7 shows the geometry of the hexagonal phase of frozen water. Each oxygen atom (grey ball) is surrounded by four neighbour oxygen atoms. A hydrogen atom (red ball) lies on each oxygen-oxygen bond. Centres of the oxygen-oxygen bond form tetrahedron surrounding one oxygen atom (full red and black dotted lines). Black dots show vertices of tetrahedrons.

For a better description of the frustration of this system, let us focus on the red tetrahedron. Hydrogen atoms can occupy two possible positions: within the tetrahedron or outside of it.

Since there is repulsive electrostatic force between hydrogen ions [12], all hydrogen ions would prefer to occupy a position outside the tetrahedron. Still, this configuration cannot propagate trough out the whole lattice. For this reason, the minimum energy in ice is reached if two hydrogen ions are in the tetrahedron and two are out. These "two-in"

"two-out" conditions are known as *ice-rules*. Red arrows indicate the displacement vector of hydrogen atoms from a central position on the oxygen-oxygen bond.

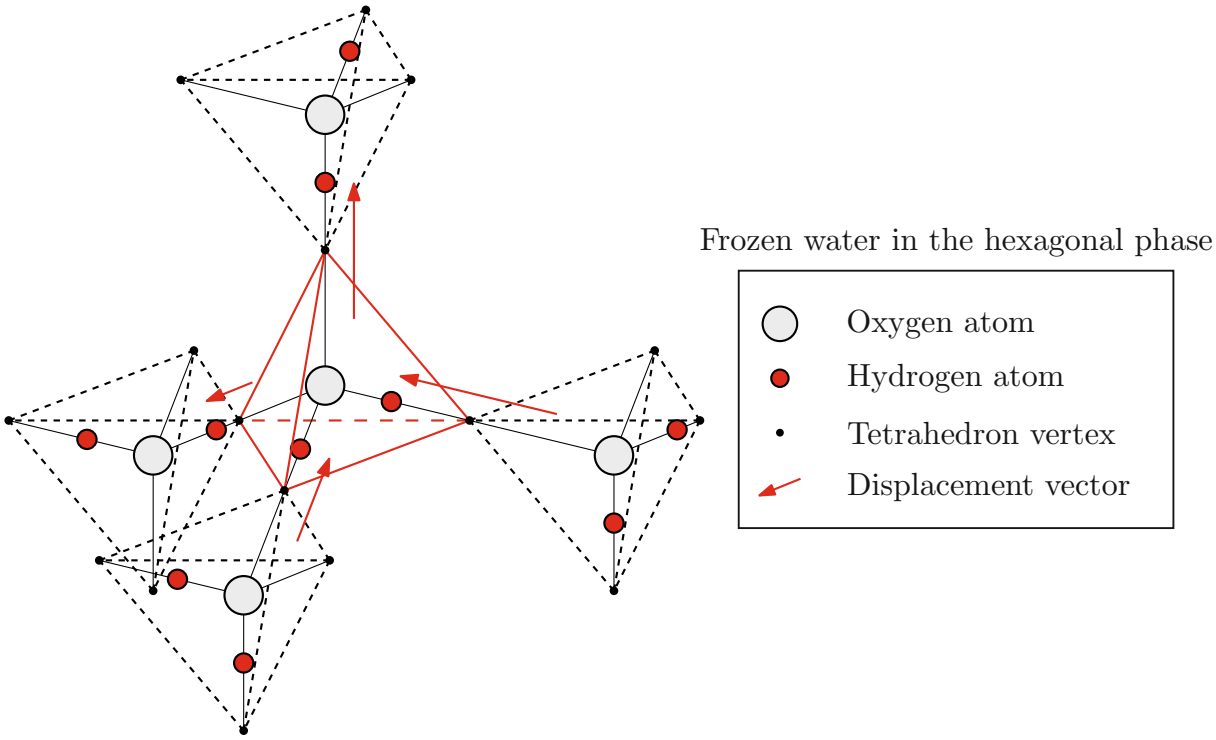

Figure 1.7: Simplified schema of frozen water in its hexagonal phase. For more complex information see [7].

In the 1930s, several papers were published [6, 12] with puzzling consequences of this geometrical frustration of frozen water. Giaque et al. found out that the residual entropy of frozen water was non zero and measured value $S = 0,82 \pm 0,05\,\mathrm{cal{\cdot}K^{-1}mol^{-1}}$. In 1935 Pauling [7] found out and described the reasons that cause this residual entropy by calculating the function of degeneration for frozen water. The total number of configurations for a system with N oxygen ions is 2^{2N}. For each oxygen, there are sixteen (2^4) possible configurations of hydrogen atoms displacements. Six of these sixteen configurations obey the ice-rules and therefore are allowed. The function of degeneration for the lowest possible energy state of frozen water is [13]:

$$g_{\mathrm{water}} = 2^{2N} \cdot \left(\frac{6}{16}\right)^N = \left(\frac{3}{2}\right)^N \tag{1.14}$$

and entropy of this system per site is:

$$S = k_{\mathrm{B}} \cdot \ln g_{\mathrm{water}} = 5,60 \cdot 10^{-24}\,\mathrm{J \cdot K^{-1}} = 0,81\,\mathrm{cal \cdot K^{-1} \cdot mol^{-1}} \tag{1.15}$$

Pauling results perfectly matched Giaque measurements. Pauling also explained how water transforms from one ground state to another [7], and therefore, the water in its hexagonal phase is still fluctuating even at very low temperatures.

1.3.2. Spin ice

Six decades after the ice-rules were observed and described in water ice, it was discovered that similar behaviour is also present in pyrochlore crystals in the low-temperature regime [14–17]. The magnetic ions of pyrochlore crystals such as $Ho_2Ti_2O_7$ and $Dy_2Ti_2O_7$ are effectively Ising-like. These ions form perfect tetrahedrons similar to water ice. Harris et al. [14] measured ferromagnetic interaction between the ions, but even at very low temperatures 0.05 K, neutron diffraction did not detect any proof of long range ordering.

In Figure 1.8 b), the magnetic moments of magnetic ions are represented by blue arrows. The interaction between the moments is ferromagnetic; therefore, the system would minimize its energy if all moments are in *head to tail*. Since the ions are positioned on the vertices of a tetrahedron with the spins oriented along the $\langle 111 \rangle$ directions, a configuration that could satisfy all interactions simultaneously does not exist. Therefore there is no way to arrange all the pairs of the Ho^{+3} Ising spins to satisfy their ferromagnetic coupling. Instead, the energy is minimized if two moments point in and two out. This behaviour is similar to water ice, and direct mapping can be done between water ice displacement vectors and pyrochlore crystal spin vectors, hence the name *spin ice*.

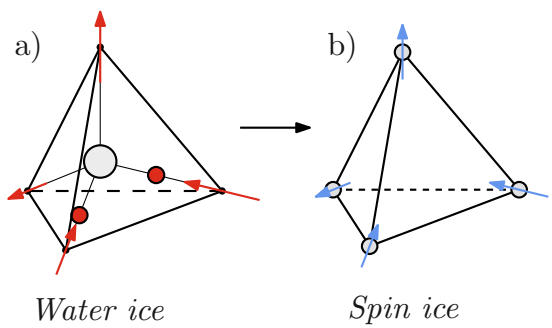

Figure 1.8: a) Atomic configuration of frozen water in its hexagonal phase with an oxygen atom (grey) and hydrogen atoms (red). The red arrows show the displacement vector of hydrogen atoms. Two hydrogen atoms are in the tetrahedron, and two are out. See Figure 1.7 for a detailed description. b) Magnetic ions form perfect tetrahedrons in spin ice crystals. Blue arrows represent their magnetic moments. Minimal energy of one spin ice tetrahedron is reached if two moments point in and two out.

A similar method to the Giauque et al. [6] was used on $Dy_2Ti_2O_7$ crystal by Ramirez et al. [15], and the results were in good agreement with water behaviour. However, the spin ice system measurements must be conducted at a very low temperature and by a technique such as a neutron diffraction. These techniques can not measure the spin degree of freedom, and we are bound to see only the average information of the system.

1.3.3. Artificial spin ice

At the beginning of the millennium, Tanaka et al. [9,10], and Wang et al. [11] successfully fabricated artificial arrays of nanomagnets that captured some behaviour of the frustrated spin ice systems, but in the two-dimension lattices. With the improvements in nanofabrication techniques, the design of artificial systems can get more complex and better at

capturing the physics that would be difficult or impossible to observe in nature. There are two possibilities for how the 3D spin ice geometry can be transferred into 2D geometry.

Figure 1.9 shows two possible ways in which pyrochlore crystal can be projected into the two-dimension system: b) *vertex projection* and c) *edge projection*. Two two-dimension lattices can be built up from the projections. The primitive cell of the kagome lattice is derivative of vertex projection, and the square lattice's primitive cell is the result of the edge projection of pyrochlore crystal. These lattices are shown in Figure 1.9 d) and e).

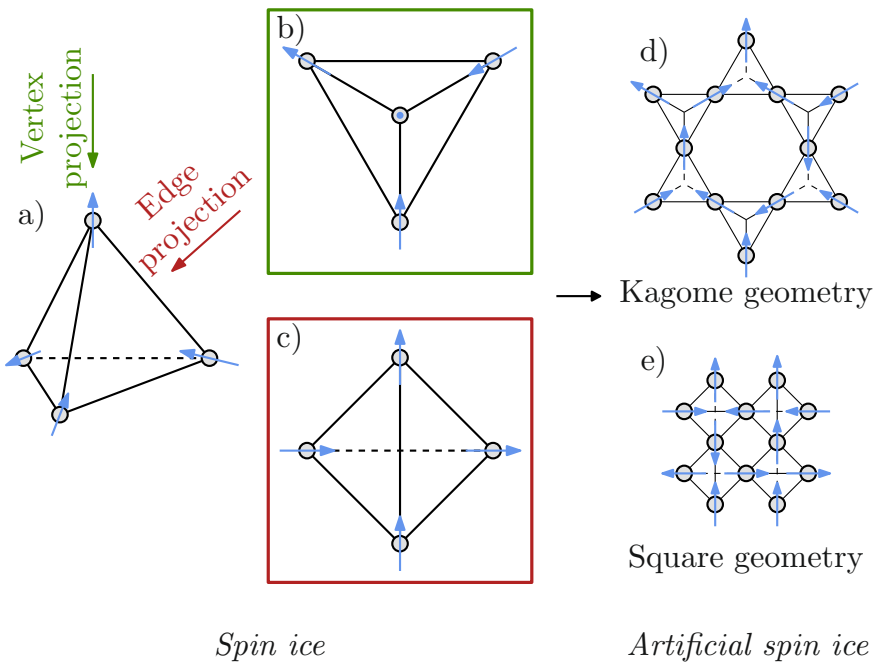

Figure 1.9: a) Spin ice tetrahedron and the two possible projections of it into the two-dimension plane: b) vertex projection and c) edge projection. d) Kagome lattice and e) square lattice are possible two-dimensional lattices built up from the projection of tetrahedron into 2D space.

The system can be called *artificial spin ice*, if it is a frustrated system with a six-times degenerated ground state and geometry derived from ice. Plenty of artificially fabricated frustrated systems do not meet previously mentioned conditions. Those systems will be called *artificial spin systems* for the purpose of clarity.

Artificial spin ice lattices are created by a pattern of elongated nano- or micromagnets. These nanomagnets need to be small enough to be a single domain. The magnetisation of these single-domain *macrospins* always points along the long axis of the nanomagnet and therefore is a good approximation of Ising-like spins in spin ices. Measurement of the nanomagnets' magnetisation can be done directly and provide the visualisation of the spin degree of freedom. Another advantage of artificial spin systems is that the strength of the interaction can be tuned by changing the spacing between the nanomagnets and other geometrical parameters.

The artificial kagome geometry

Figure 1.10 a) shows an example of how the artificial kagome lattice can look. There are more ways the lattice can be realised, and they are discussed more in Chapter 3, which is dedicated to describing this artificial system.

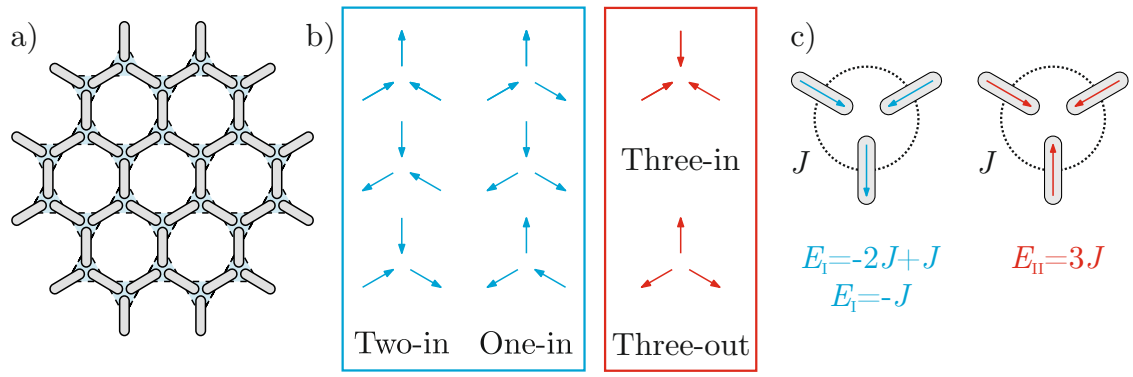

Figure 1.10: a) Artificial kagome spin ice lattice, grey nanomagnets are placed on the apex of the kagome layout (blue triangles), forming the lattice. b) Six possible ground state configurations obey the kagome ice-rules (blue frame) and two ice-rules breaking high-energy configuration (red frame). The ground state energies and high-energy configurations are shown in c), where J is the coupling strength constant between the spins.

The vertices are geometrically frustrated since the "macrospins" (single domain nanomagnets) interact via dipolar interaction. They minimise their interaction if they point head to tail, which is impossible for all three pairs of spins in the vertex. The ground state spin configuration follows the kagome modified ice-rule: two-spin outside or two-spin inside of the vertex, and it is six times degenerated as is shown in Figure 1.10 b) in the blue frame. In terms of the J coupling strength constant, the energy of the ground state configuration is $E_{\mathrm{I}} = -2J + J = -J$ since two interactions are minimised ($-2J$), and one is maximised (J). The other two high-energy spin configurations have no interaction minimised, and the total energy of these vertices is $E_{\mathrm{II}} = 3J$. The J coupling constant's strength can be tuned by changing the spacing between the nanomagnets.

This type of kagome realisation can be called an artificial spin ice system. Since the ground state is six times degenerated, and the geometry is derived from the ice and spin ice systems, even though there are sixteen possible vertex types in ice or spin ice systems.

The artificial square geometry

The pioneering work on the artificial square geometry was done by Wang et al. [11]. Wang introduced the square spin geometry shown in Figure 1.11 a). The lattice is made of single-domain Ising-like nanomagnets placed on a layout made of edge projection of pyrochlore crystal (the blue square layout).

There are sixteen possible spin configurations (divided into four types), since each vertex has four spins with two possible orientations similar to the ice and spin ice systems. All possible spin configurations are shown in Figure 1.11 b). Contrary to the spin ice vertices, in the artificial square spin system, the interacting nanomagnets do not have the same interaction strength. Therefore, there needs to be considered two types of neighbours

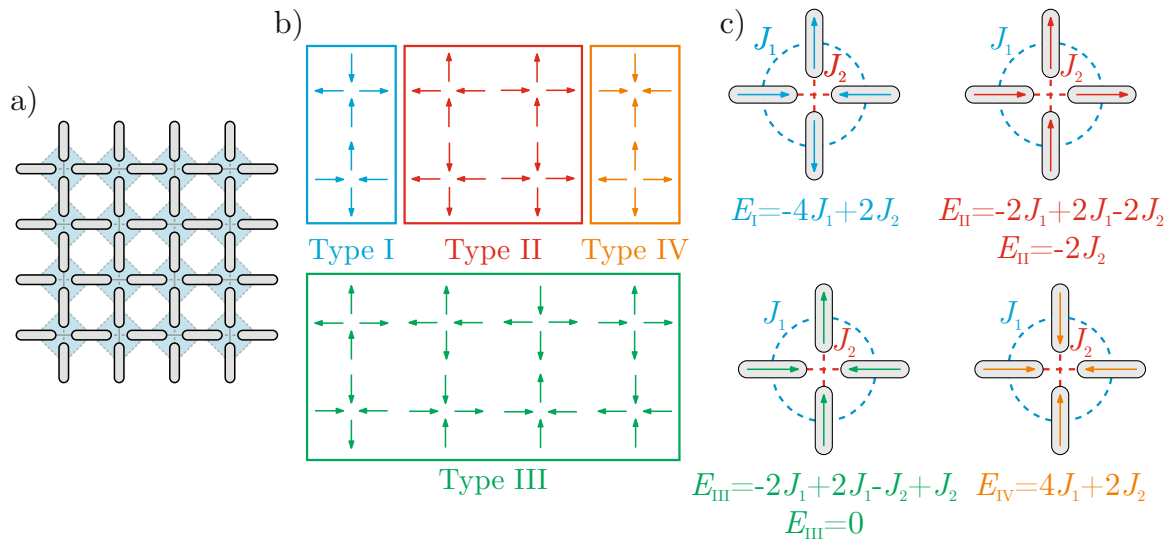

Figure 1.11: a) Wang's square lattice, nanomagnets (grey islands) are put at the apex of square ice projections (blue squares). Sixteen possible spin configurations in square vertex. Type I and II are ice-rules obeying configurations. Type III and IV are high-energy ice-rule-breaking configurations. The total energy of each type of configuration is calculated in c), where J_1 is the coupling constant between the first nearest neighbours a J_2 between the seconds.

in the vertex. The first nearest neighbours are perpendicular to each other, and their coupling constant is J_1. The second neighbours are parallel and their coupling strength constant is J_2. The energy of each vertex type in the multiple of J_1 and J_2 are shown in Figure 1.11 c).

Because the transformation into a two-dimensional system breaks the system's symmetry, and because $J_1 > J_2$ the ground state spin configuration of Wang's square lattice is only two times degenerated, this system should not be called an artificial spin ice system.

One of the goals of this thesis is to design a new square lattice where the symmetry would be restored. Chapter 4 is dedicated to the description of the square geometry so that the spin ice models can be probed with all the advantages of using artificial systems.

1.4. Artificial spin liquids

The primary motivation for designing and fabricating artificial spin systems was to access the physics of disordered magnetic states in real space and to access the spin configuration spin by spin. With artificial systems, it is now possible to image collective states of matter and many-body physics of frustrated spin systems, which uncover exotic phenomena such as spin fragmentation or the existence of magnetic monopole-like excitation. Artificial spin systems are a well-engineered playground for researching the physics of spin liquids. And because this thesis is focused on designing new systems to capture the exotic physics of spin liquids, it is important to define what spin liquids are.

Artificial spin liquids are disordered but correlated magnetic state, which pairwise correlations decay to zero at large distances [18].

The discussion will be limited to classical spin systems throughout this thesis. No quantum effects are present and will not be considered.

Spin liquids contain various interesting physical phenomena. Contrary to the standard matter, which can be in solid, liquid or gas phase, but at the low temperature the phase is always solid, some spin liquids remain disordered even at the lowest possible temperature (for example, kagome Ising antiferromagnet described in section 3.1). Some spin liquids are, on the other hand, characterised by long range order phases at low temperatures.

The spin liquids can be divided into two groups [19]: one which has a finite correlation length approximately in the order of one lattice constant spin-spin correlation decay exponentially with the distance. The other is called *algebraic spin liquid*, and their spin-spin correlations have power-dependence and infinite correlation length [18]. The example of such algebraic spin liquid with its exotic behaviour is discussed in section 3.3.

The spin liquid can be called *Coulombic spin liquid* if it can be viewed as a coarse-grained, spatially fluctuating magnetic vector field. Henley [20] introduced the concept of the Coulomb phases and defined the three conditions the lattice model has to satisfy for the Coulomb phase to emerge:

1. Each lattice variable (the spin in our case) can be mapped to a discrete signed magnetic flux $\mathbf{p}_i$, running along bond i;
2. At each lattice vertex, the sum of these signed fluxes is zero.
3. The system is in a highly disordered state (i.e., liquid-like).

It can be proved that such vector fields obey the law of magnetostatics. Once all three conditions are met, the spin system is called *Coulomb spin liquid*. The examples of such spin liquid are discussed in Chapter 4.

1.5. Motivation and overview of the thesis

The exotic physics of frustrated systems are usually well-known and described theoretically. However, designing an artificial system which captures the desired behaviour so it can be measured in real space is still very challenging, even with all the development in nanofabrication techniques.

The motivation for this work is twofold. We want to invent and test new designs of artificial spin systems which are better at capturing the physics of different spin and vertex models connected to spin liquid physics. We prove that the newly designed lattices are functional within the theoretical frameworks and use them to understand the theoretical models better.

The main idea behind this thesis is to change the lattices by using connected nanomagnets instead of disconnected ones. These connections transform the system from a spin system, where the physics is driven by many body dipolar interactions between individual spins, into a vertex system. In the vertex system, the physics is now driven by the micromagnetic energies at the vertex sites. We can tune the micromagnetic interactions almost at will by designing special defects at the vertex sites of the connection nanomagnets. By changing

the vertex geometry, we can force the system to change its ground state configuration and configuration of excited states.

Chapter 3 presents the kagome lattice with notches as a new artificial spin system. The main problem with the kagome dipolar spin ice systems (with disconnected nanomagnets) is that it is near to impossible to force the system into low-energy spin configurations. The reasons why it is impossible are discussed in the chapter. However, our approach can bypass these limitations and prepare lattice capturing the spin configuration of low-energy phases of the kagome system.

In Chapter 4, we show how the lost degeneracy of the artificial square spin system can be restored. Furthermore, our approach can be practically used for researching individual realisation of possible vertex models connected to the square and ice geometry. We also provide the experiment based on our new lattice, which allowed us to observe real space infinite order phase transition in one of the F model [21], which is one of the celebrated vertex models.

Our results could be a gateway to a more precise study of a wide range of frustrated spin and vertex models.

Chapter 2: Methodology

Our experimental strategy relies heavily on designing new lattices that would better capture the physics of spin systems. We focus on two-dimensional artificial kagome and square spin systems described in the previous chapter. The key element of our research is redesigning the geometry of these systems to control the driving physics. By physically connecting the individual single-domain nanoislands into one macro lattice, we are transferring the spin system into the vertex system. At each vertex site, micromagnetic energies compete over the resulting configuration.

Therefore, central idea of this work is to replace the spin degree of freedom with a local "*micromagnetic knob*", which can be used to finely tune the total micromagnetic vertex energy.

In order to predict the behaviour of our newly design artificial spin systems, Monte Carlo and Mumax^3 simulations are conducted. The simulations are described in section 2.1.

After the target properties of lattices are acquired from simulation, the lattices are fabricated by *Electron beam lithography* (EBL). The required material is deposed by *Electron beam physical vapour deposition* (EBPVD). Fabricated samples are checked by *Scanning electron microscopy* (SEM) to see the quality of the sample. The fabrication techniques are described in section 2.2.

Magnetic field demagnetisation brings the magnetic samples into their low-energy configurations. The demagnetisation device and protocols are described section 2.3.

To acquire information about the sample's magnetic configuration, *Magnetic force microscopy* (MFM) is used. From MFM outputs, the analysis is done by various in-house custom build software. MFM technique and data analysis processes are described in section 2.4.

2.1. Simulation techniques

The reason for using simulations in our experiments is twofold. Firstly, when encoding specific microstates into the lattice topography, we need to know the targeted spin configurations so the sample design can be done correctly. Knowing the spin configurations is crucial for our kagome lattices with notches described in Chapter 3, and Monte Carlo simulations provide us with this information.

Secondly, we are using specially designed geometrical defects as the system's external parameter. These defects control the magnetic behaviour of the system. We need to know how changes in these parameters affect the system. Mumax^3 can compute these effects for both studied systems presented in this work. Outputs from the simulations are crucial for sample fabrication.

2.1.1. Monte Carlo simulations

Monte Carlo simulations are developed by Benjamin Canals and run by Nicolas Rougemaille at Néel Institute, Grenoble, France. These simulations are a powerful tool to predict spin configurations in any desired kagome Ising spin ice phase. In our project, Monte Carlo simulations played a crucial role in sample fabrication for the kagome lattice with notches described in Chapter 3. The idea is to imprint the desired spin configuration into the topography of the system. Therefore we need to simulate the spin configuration outcome we want to observe before we start the fabrication of the lattice.

For this reason, a series of transformation scripts were programmed in LabVIEW and python, allowing us to design layouts for almost any[6] imaginable spin configuration. The example of the simulated spin configuration output from Monte Carlo simulations is shown in Figure 2.1, as well as the layout design capturing this configuration. The physical effect of the notch will be explained in Chapter 3.

I want to thank Ing. Jakub Sadílek, who helped me develop the Python scripts necessary for designing our lattices.

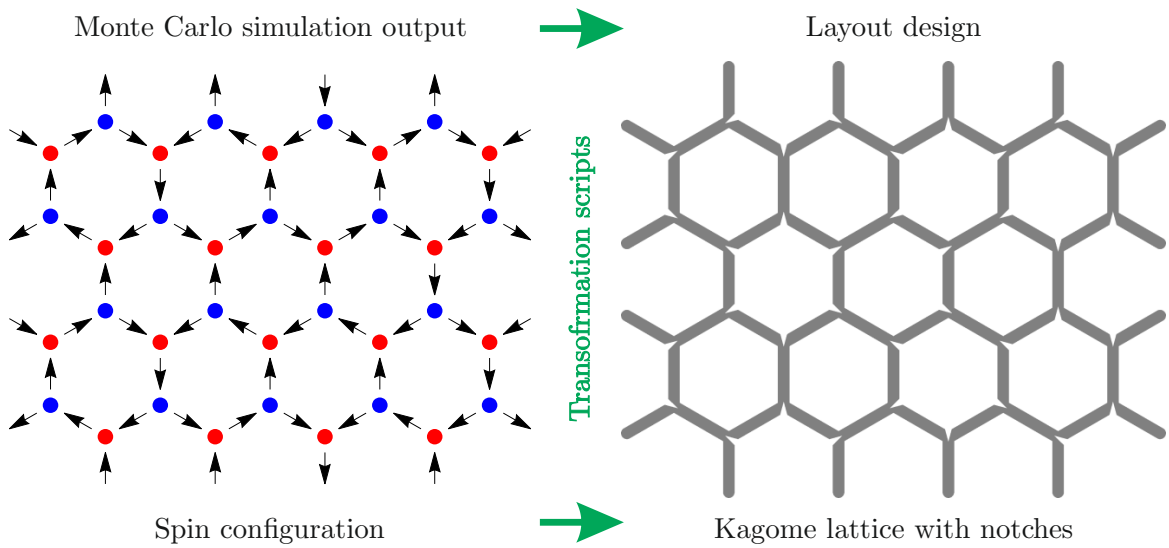

Figure 2.1: Schematics of how Monte Carlo simulation output is transformed into the layout design of kagome with notches via a series of in-house-made scripts. The lattice has the position of the notches determined by the spin configuration it tries to capture.

Monte Carlo simulations are also a powerful tool for finding our modified lattices' thermodynamic profiles, as explained in section 3.5.5.

2.1.2. MuMax^3 simulations

For calculating the total energy and other parameters of our designed system, the open-source MuMax^3 micromagnetic simulation software is used [22]. MuMax^3 calculates the space- and time-dependent magnetisation dynamics in nano- to micro-sized ferromagnets using a finite difference discretisation. For some calculations, MuMax^3 uses *graphical*

[6] We cannot design lattice where all the connected nanomagnets have their magnetic orientation pointing inside or outside of the vertex.

processing unit (GPU), and therefore it is faster than, for example, OOMMF[7]. We are using MuMax^3 for qualitative analysis of our modified lattice. Usually, we are only interested in the total energies (in the case of our experiments, the total energy is the sum of demagnetisation energy and exchange energy) of the domain walls (DWs) at the vertex sites, which are a result of nanomagnet connections and how the geometrical defects can tune the total energy of these DWs.

MuMax^3 code allows us to set the simulation parameters as close as possible to our experimental parameters, such as studied geometry and material parameters. An example of how useful the simulations can be for obtaining qualitative information and understanding the behaviour of micromagnetic texture when designing the lattices is shown in Figure 2.2. One vertex of the kagome lattice with a notch implemented at the vertex site is simulated for three different depths of the notch 0, 100 and 200 nm. The dimensions of the simulated nanomagnets are: length 750 nm, width 250 nm and thickness 25 nm.

The size of the notch changes the micromagnetic configuration and resulting magnetic stray field, and the micromagnetic energies are shown in Table 2.1. In the shown example, each nanomagnet have defined magnetisation. However, the centre around the notch had random magnetisation, and the simulations were designed to find the energy minimum. Results shown in Figure 2.2 a) have lower energy than results in Figure 2.2 b) as supported by energy breakdown in Table 2.1. The simulated stray field images also predict what patterns can be expected when measured with MFM. It can be seen that when a notch is present at the vertex site, the signal from the stray field is more intense for the high-energy configurations. These findings can help with data analysis since our main tool for acquiring the spin configurations is MFM which indirectly measures the stray field.

As mentioned before, the total magnetic energies is the sum of demagnetisation and exchange energy. Energy result from simulations are shown in Table 2.1. We can see that when the notch depth is 0 nm for both spin configurations, all energies are the same (as expected). However, as the depth of the notch increases, the high-energy configurations also increase their total energy. This energy increment is because the magnetisation flow must change its direction more abruptly since the magnetisation must curl more around the notch instead of just splitting the flow into two channels, as in the case of ground state configuration. These simulation outputs (shape of the stray field, qualitative changes in energies) give us an idea about the system's behaviour. We rely on them in all of our research, as will be explained and shown in Chapter 3 and Chapter 4.

The script used for the MuMax^3 simulations for both studied systems are shown in Appendix A.

[7] *The Object Oriented MicroMagnetic Framework*, another heavily used software for micromagnetic computations.

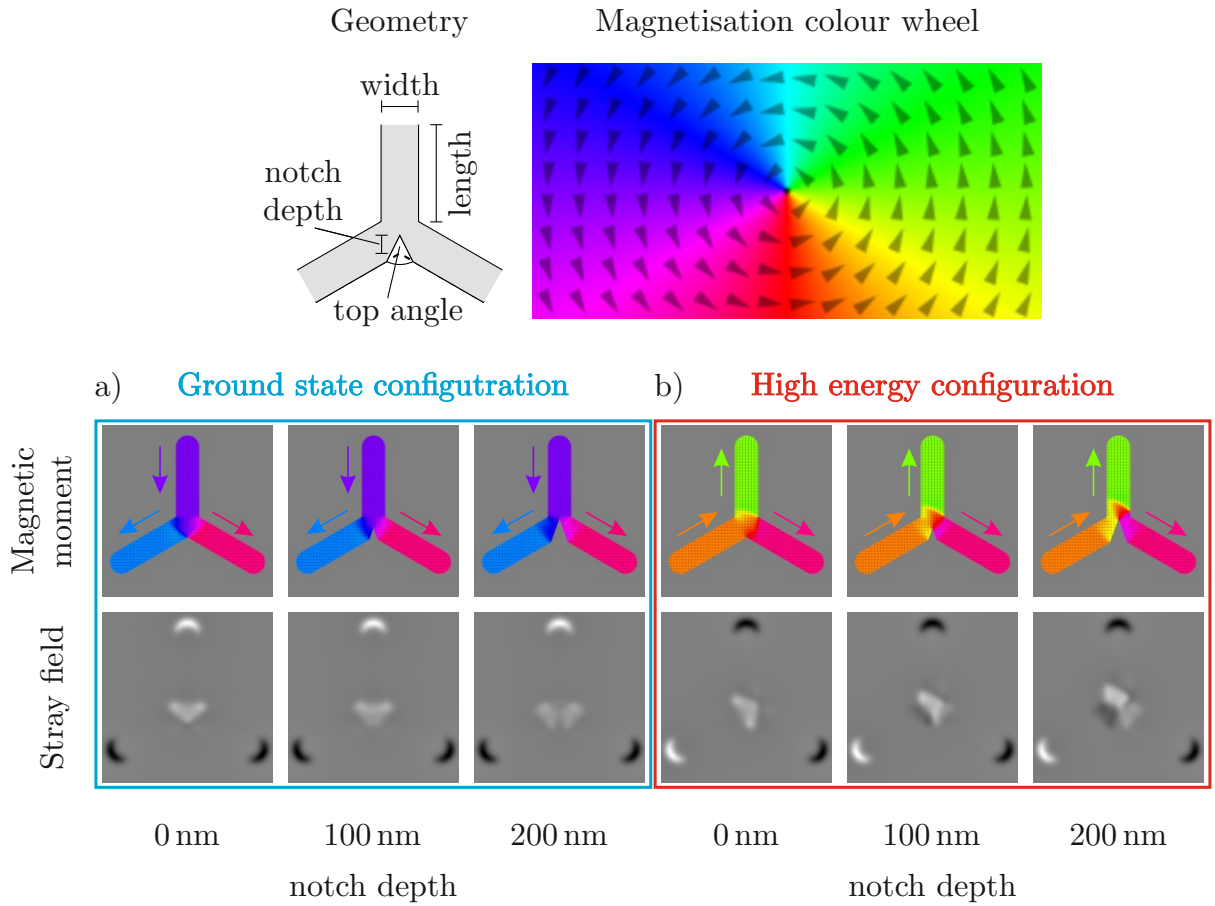

Figure 2.2: MuMax^3 simulation results for kagome vertex with notch. Two different spin configurations, a) ground state and b) high-energy, were defined and studied for three different depths of the notch 0, 100 and 200 nm. The simulated magnetic stray field related to micromagnetic texture at the vertex site shows possible MFM signals. Geometry of simulated objects are: length 750 nm, width 250 nm and thickness 25 nm.

Table 2.1: Demagnetisation, exchange and total energy of simulated ground state and high-energy configurations are shown in Figure 2.2. For the depth of the notch 0 nm, the energies are the same for both configurations as they should be. However, with an increment in the notch depth, there is an energy splitting between the two configurations.

	Ground state configuration			high-energy configuration		
Notch depth (nm)	0	100	200	0	100	200
Dem. energy (J)	9,32E-17	9,16E-17	8,97E-17	9,32E-17	9,87E-17	1,04E-16
Exch. energy (J)	1,87E-18	9,03E-19	8,07E-19	1,87E-18	2,89E-18	4,21E-18
Total energy (J)	9,52E-17	9,25E-17	9,05E-17	9,52E-17	1,02E-16	1,08E-16

2.2. Sample fabrication

Fabrication of all samples used during the research described in this manuscript was done with a one-step lift-off procedure. The EBL was done either with E-beam writer RAITH150 Two (RAITH) in BUT CEITEC research laboratory or Nanobeam Nb5 in Nanofab Institut Néel.

The samples used in our research were designed and fabricated to be thermally inactive. The magnetic objects forming our lattices are thermally stable, and their magnetic configuration is not affected by the temperature. As such, all measurements can be done at room temperature. The fabrication parameters differ only in the lithograph setting and chemical used during the kagome and square systems process. Therefore, the fabrication process will be explained on the kagome lattice, and the parameters for square systems are shown in Appendix B.

2.2.1. Electron beam lithography

The EBL is a well-known technique for fabrication in nanoscience. Due to the precision (even sub 10 nm [23,24] resolution) that EBL can reach, it is the perfect tool for designing and fabricating lattices of interacting nanomagnets that can capture the physics of spin liquids described in the previous chapter. This technique allows us to design our lattice with precise variations in geometry, enabling us to control the role of micromagnetic interaction almost at will.

The principle of EBL is shown in Figure 2.3 and all the steps are described in the following paragraphs with corresponding labelling.

a) **Substrate preparation:** A suitable substrate needs to be chosen and cleaned from all surface impurities. The substrates we used were silicone 2-inch wafers doped with boron with crystallographic orientation (100). The substrate is exposed to an ultrasonic bath in acetone for 3 minutes at room temperature. Acetone bath usually gets rid of all surface impurities. A second 3 minutes long bath in isopropyl alcohol is used to remove residual acetone from the surface of the substrate. The last cleaning step is placing the substrate on the hotplate for one minute at temperature 150 °C to remove any droplets left from the surface.

b) **Resist spin-coating:** Special materials called *resist* are used for EBL. Resist changes its molecular structures after interactions with electrons. There are two types of resist: *positive* resist - electrons interact with resist, and the irradiated area becomes more soluble, *negative* resist - the irradiated area strengthens its bonds and becomes less soluble. In all our fabrication procedures, we used positive resist AR-P 6200.09. The resist is coated onto the sample by *Lithographic wet bench for coating (SUSS-WETBENCH)* at CEITEC nano laboratories. The substrate is placed in the coater, and a droplet of resist is put on it. To achieve the targeted thickness of 50 nm of the resist layer, the coater starts to rotate with speed 6000 rpm and with an acceleration 1500 rpm/s for 60 s. To strengthen the resist after spin coating, the sample is placed again onto the hot plate for one minute at temperature 150 °C.

c) **Mask fabrication:** The most important part of the EBL procedure is the exposure of the resist. A focused beam of electrons interacts with the resist and changes its solubility. The quality of the fabricated nanostructures depends on many factors: beam energy, beam spot size, exposure time and writing strategy. The exposure was done and optimised with *E-beam writer RAITH 150 two*.

d) **Resist development:** After the electron beam change solubility of the exposed resist, the sample is immersed in the developer solution, which dissolves and rinses away resist from exposed areas. It is crucial to choose the right combination of resist and developer. In our case, the AR 600-546 was used for one minute. The next step was to rinse the sample in demineralised water and dry it by nitrogen pressure flow.

e) **Material deposition:** After resist development, the sample was placed into *Electron beam evaporator BESTEC* where the required material (NiFe - permalloy) was deposited. Evaporation-based techniques are used because, compared to sputtering techniques, more directional deposition reduces the amount of material deposited on the side walls of resist, which is crucial to prevent, especially in our newly designed lattices. During the evaporation process, the sample was rotating with $5\,rpm$ to eliminate asymmetric deposition caused by for example, a small sample tilt. The thickness of the material was usually between $15 - 25\,\mathrm{nm}$.

f) **Lift-off:** The last step of the fabrication procedure was to remove the rest of the resist with all the material deposited on it. To do so, the sample is put into a chemical for dissolving and rinsing away the unexposed resist while the material deposited directly on the sample remains.

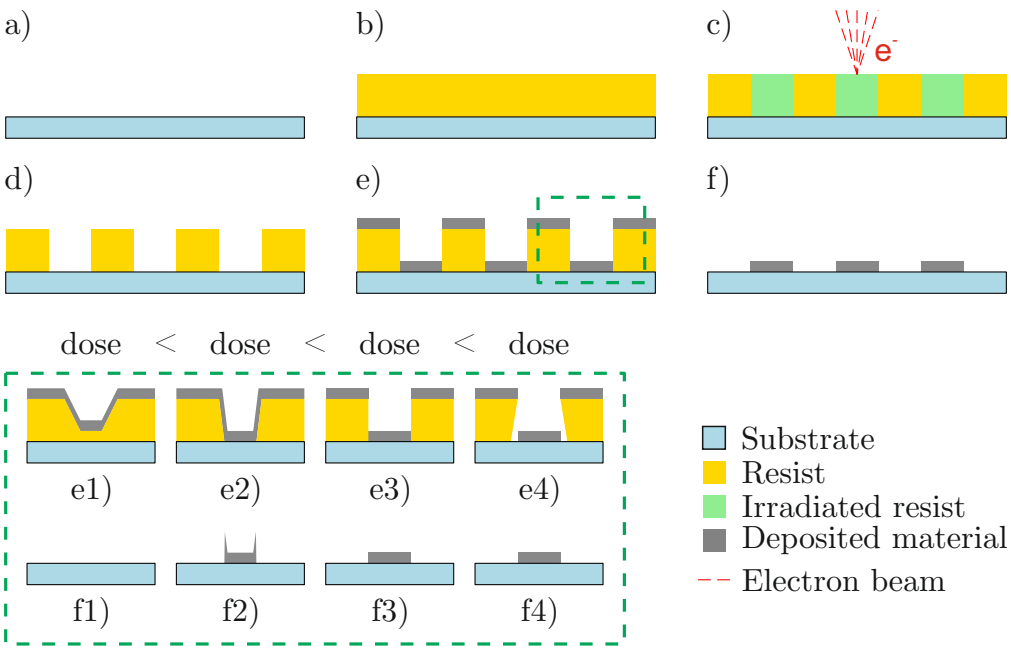

Figure 2.3: Principle of EBL: a) Choosing and cleaning a suitable substrate. b) A layer of resist is spin-coated on the substrate. c) Exposure of the resist by electron beam lithography. In the case of positive resist, the solubility of irradiated resist is increased. d) Resist after development. The irradiated resist was removed from the sample in a developer chemical. e) The required material is deposited onto the whole area of the sample. However, the material is directly deposited onto the substrate in areas where resist was developed and rinsed away. f) The rest of the resist, together with all deposited material, is removed and only desired structures remain.

As mentioned before, our strategy is to control the physics of researched systems by precisely tuning the properties of fabricated lattices with strategically placed defects at the vertex sites. It is then crucial to have well-defined structures.

Therefore it is important to discuss the effect of the dose used during the exposure on the shape of the resulting objects. In our experiments, the quality of resulting structures is most influenced by the developed resist profile. If the right combination of resist and developer is chosen, the mask's shape is mainly influenced by the exposure dose. In Figure 2.3, there is a schematic of dose effect on the shape of the developed resist and deposited material in a series of images e1)-e4). And the corresponding objects after the lift-off procedure are shown in f1)-f4).

In the case of e1,), the dose was too small, and the resist was not irradiated enough. Therefore the material is nowhere deposited only on the substrate and is all carried away during the lift-off procedure, as is shown in f1). With a higher dose, but still lower than the optimal, the shape of the developed resist is not perpendicular to the substrate and a non-negligible amount of material is deposited even on the walls, as is shown in e2). After the lift-off procedure, most of the deposited material is removed. However, some residual and non-desirable amount of deposited material is still present at the edges of the structure, forming ear-like defects as shown in f2). At some parts of the sample, the material can even crack the surface and edges during the lift-off, damaging the resulting structures. The ear-like and crack defects can affect the fabricated structures' magnetostatic (helping stabilise high-energy configurations) or dynamic (pinning the domain wall propagation) behaviour. Using the optimal dose as in the case of e3) or a slightly large dose as in the case of e4) lead to perfect or overdeveloped profiles, respectively. Both cases lead to the perfect structures after lift-off, as shown in f3) and f4). Therefore, the strategy we highly recommend using when trying to reproduce our results is fabricating many versions of the identical lattices with a small step in doses to increase the probability of successfully creating decided lattices.

Both studied lattices have different response to imperfect fabrication. The kagome lattices with notches which vertex can be seen in Figure 2.4 a) benefits from the fact that we are deliberately breaking the system's symmetry. Both magnetostatics and magnetodynamics are entirely driven by the notch defect. Therefore, even if some imperfections or even ear-like defects appear, they are overcome mainly by the presence of the notch.

The second type of geometry we study is the square lattice with holes which vertex is shown in Figure 2.4 b). The addition of the "hole defect" at the vertex site is not breaking the symmetry of the system if the hole is indeed circular. Since we rely on the hole governing the physics, the fabrication needs to be done as precisely as possible. Especially the ears-like defects can truly be mixed up with the outcome since having some extra unwanted magnetic material can help stabilise the undesirable magnetic configurations.

Fabricating the square lattice with holes is more complicated than the kagome lattice with notches. However, after several optimisation procedures and dose sweep strategy, all lattices can be reproducibly fabricated, capturing the physics of spin systems described in the following chapters.

Both kagome lattices with notches and square spin systems with holes presented different non-trivial challenges during the fabrication process.

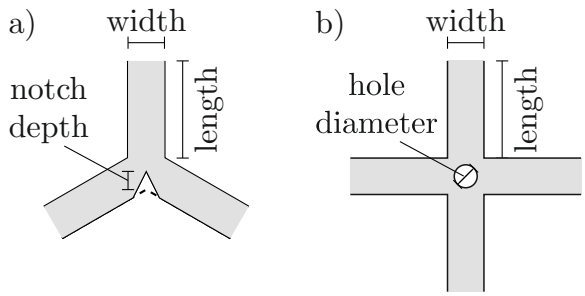

Figure 2.4: The schema of the vertices of a) kagome lattice with notches and b) square lattice with holes. The symmetry of the kagome vertex with notch is broken by design. Therefore it is less susceptible to defects caused by the fabrication process than the perfectly symmetric square vertex with hole.

In the case of kagome lattices, the fabrication was easily done after the layout designs. The main problem was finding an effective and flawless process to produce a series of layouts needed for research efficiency. This problem was already addressed in section 2.1. Figure 2.5 a) shows an example of a fabricated aperiodic lattice.

On the contrary, square spin systems were always easy to design. They are periodic, and the hole at the vertex site is the same all over the lattice, as shown in Figure 2.5 b). However, the hole diameter changes the physics drastically even if the hole diameter changes only by a few nanometers. The sensitivity of hole diameter require perfectly done lithographic procedures.

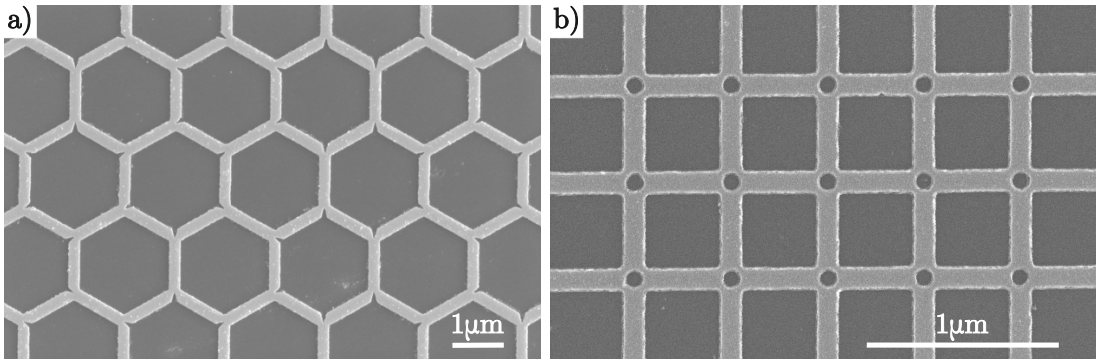

Figure 2.5: SEM images of a) kagome lattice with notch and b) square lattice with holes.

A series of lattices with holes is shown in Figure 2.6. The width of the connected islands is 100 nm, the distance from the centre of the vertex to the vertex is 500 nm, and the thickness is 25 nm. The hole diameter is the only parameter that changes between the fabricated lattices. If the hole diameter is too small, as is in the case of the nominal value of 64 nm, the resist and the magnetic material from the centre of the vertex are not properly lifted off and collapse. We can observe the fallen pillars at some vertex sites. The second type of problem occurs when the material is not fully lifted-off at some vertex sites, and during the ultrasound bath, it breaks off with a part of the lattice. Therefore all lattices we fabricated with hole diameters 64 nm and smaller are unusable. The series of lattices we used for our research described in Chapter 4 have hole diameters from 72 nm to 120 nm.

A defect in the first vertex in the second row in the lattice can be seen with 120 nm hole diameter. This defect is more common in lattices with larger holes, which is why we do

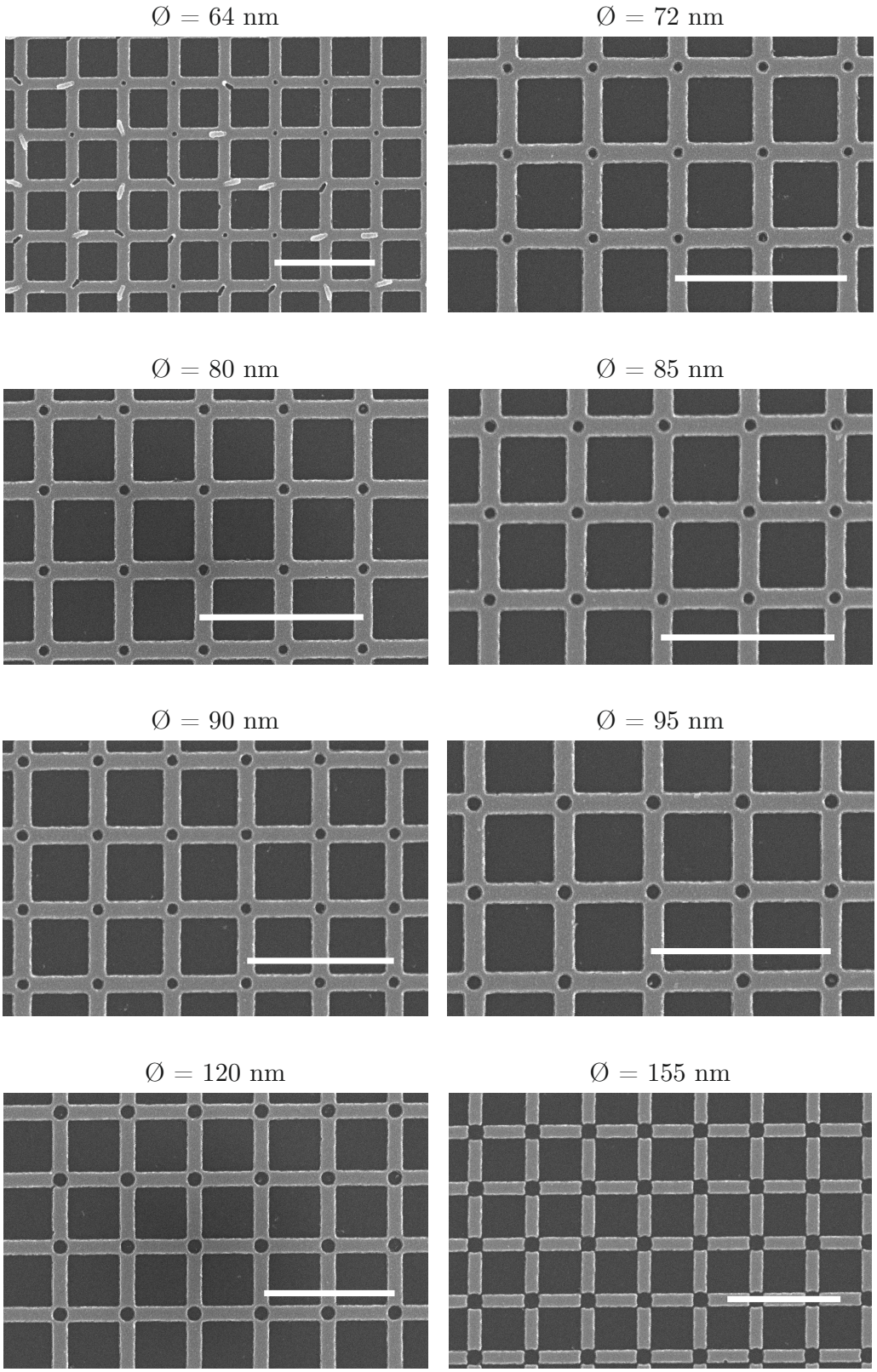

Figure 2.6: SEM images of part of the lattices with different hole diameters. All other lattice parameters were: width of the islands 100 nm, the distance from center of the vertex to vertex is 500 nm and thickness is 25 nm. All lattices are made from 30×30 vertices. The scale bar is 1 μm.

not use them. It is caused by the hole edge's proximity to the lattice's edge. Defects like this, of course, negatively affect the magnetic configuration at the vertex site, but there are less than 0.5 % of these effects in the lattices with 120 nm. We do not use any lattices with a diameter larger than 120 nm as the number of disconnected vertices increases. The largest nominal hole diameter we fabricated was 150 nm, and at all the vertex sites, the nanomagnets became disconnected.

Ing. Ondřej Brunn was involved in fabricating the square system with holes. His involvement included operation with the Nanobeam litograph Nb5 at Nanofab Institut Néel and choosing the right combination of chemicals to reach the limit of the lithographic technique.

Sample parameters

Every modified kagome lattice with notches consists of 627 vertices. Each nanoisland has an aspect ratio of 5, where the width of the nanomagnet is 200 nm, and the length is 1 μm. The thickness is 15 nm. The fabrication material is NiFe. The depth of the notch varies from $100 - 250$ nm, but is always constant in a given lattice. The lattices have a size of approximately $30 \times 30\,\mu$m.

The square system with holes consists of 900 vertices, and each nanoisland has an aspect ratio of 5. The width of the nanomagnets is 100 nm, and the length is 500 nm. The lattice is made from NiFe, and its thickness is 25 nm. The hole diameter varies from $0 - 155$ nm, but it is always constant for the given lattice. Square lattices have a size of approximately $16 \times 16\,\mu$m

2.3. Sample demagnetisation

As mentioned in Chapter 1, the artificial spin systems are frozen[8] and do not evolve in time to measure the given spin configuration. One of the first challenges after the pioneering work of Tanaka et al. [9] Wang et al. [11] was bringing the artificial spin systems into their low-energy states.

After the fabrication, the systems need to be demagnetised to recover the low-energy configurations of the artificial spin systems. Depending on the research aim and sample parameters (material, thickness, sizes, etc.), two demagnetisation protocols are available and widely used: Field driven demagnetisation and thermal demagnetisation.

Both field-driven and thermal demagnetisation protocols seem to be equivalently efficient in bringing the systems into their low-energy configurations. Both protocols described in the following paragraphs can only induce single spin flip events, shaking the systems from their higher energy configurations by flipping a series of single spins. However, both artificial systems studied in this work and described in Chapters 3 and 4 have low-energy manifolds characterised by loop models. Therefore the spin configuration and spin dynamics rely on collective spin flips (in the form of closed loop) which are experimentally

[8] The spins must not fluctuate sufficiently enough time so the snapshot of the spin configuration can be taken.

inaccessible. Therefore with current approaches, it is "lost battle" to expect reaching the ground state configurations with either demagnetisation. Even though we cannot force the collective spin loop dynamics, we can still observe and study the fingerprints of the desired physics of frustrated spin systems, mainly due to the finite size of the systems [18].

Field driven demagnetisation protocol

Magnetic field-driven demagnetisation is used for the athermal systems (systems built from ferromagnetic nanomagnets with high enough blocking temperature). The system is exposed to the external field, which cycles and decays over time. All nanomagnets still have their magnetisation point along their axis, but total magnetisation is reduced to the lowest possible value. This strategy is quite successful since many of the ground states of artificial spin systems are characterised by magnetisation close to zero. There are several proposition how to design effective field driven demagnetisation protocol [25–30].

In our experiment, we are using permalloy samples that are thermally non-active. The choice of such samples allows us to conduct the measurement of our sample at room temperature. We use a field-driven demagnetisation protocol to bring our systems into their low-energy manifolds with the following settings.

The rotating sample is put into the external magnetic field, which oscillates and decays over time and has in-plane orientation respective to the sample surface, as is shown in Figure 2.7. The sample rotation ω_{S} is much higher than the oscillation of the external field ω. The oscillation speed relation $\omega_{\mathrm{S}} \gg \omega$ should ensure that the amplitude of the field decrease only a little while facing all sides of the sample face. The demagnetisation protocol can be broken down into three different sections. Two main parameters are used for changing the effectiveness of the demagnetisation protocol: the initial amplitude of the external field B_0 and the total time of the demagnetisation t_{dem} that it takes to bring the magnetic field to zero.

At first time window $(0 < t < t_1)$, when the magnetic field is larger than value B_1 all nanoislands have their magnetisation oriented parallel with the external field. As the field decays and the demagnetisation protocol is in $(t_1 < t < t_2)$ it is in the effective magnetic window between values B_1 and B_2, only the spin flips that will minimise the total energy of the sample are realised. The third part of the process $(t_2 < t < t_{\mathrm{dem}})$ is reached when the external field amplitude is below B_2. In this part of the process, the external field is too weak to induce any change.

There is no easy way of knowing the values of B_1 and B_2[9], and still, it seems like that is not a problem. We need to be sure that the effective window of the demagnetisation protocol is long enough to bring the system to its low-energy manifold. There are two ways to prolong the effective window duration between t_1 and t_2. First, the initial starting field B_0 can be set to a lower value (but still must be high enough to saturate the entire lattice) while keeping the total time of the demagnetisation t_{dem} constant. Alternatively, the total time of the demagnetisation can be longer while maintaining the constant initial filed B_0.

[9] Since we do not know where the domain walls responsible for the magnetisation reversal are induced. Whether it is on the edge of the lattices or at the vertices sites.

In our experiment, the initial amplitude of the external magnetic field is always set to 100 mT (well above the coercive field of any of our lattices), and we use the demagnetisation time as the controlling parameter. Usually, we run the demagnetisation protocols for several days.

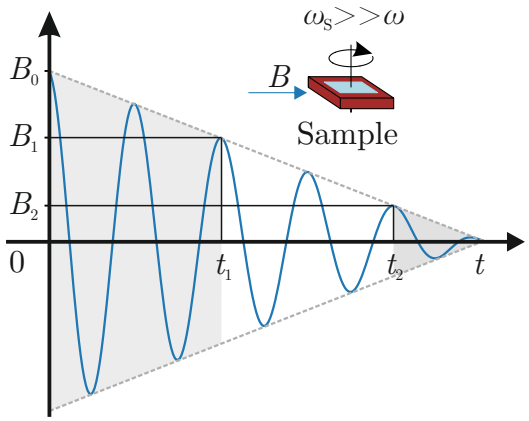

Figure 2.7: Schematic of field demagnetisation protocol. The sample is rotating within the external magnetic field B, which is oscillating and decaying over time t. The effective demagnetisation occur only between the magnetic field values B_1 and B_2. Higher fields saturate the sample, and lower have no effect.

The demagnetisation stage we use in our research is shown in Figure 2.8. Iron pole pieces are put inside the copper coil, leaving a small gap for our sample holder in between. The sample holder is mounted to the rotor, which is controlled by the Arduino controller, and it is designed in a way that allows us to demagnetise up to four samples simultaneously. The samples are usually rotating with frequency $\omega_S = 20$ Hz within the in-plane magnetic oscillating field ($\omega = 250$ mHz sine function) with decaying amplitude from initial value $B_0 = 100$ mT to 0 in several days[10]. A programmable keysight waveform generator is used to control the magnetic field.

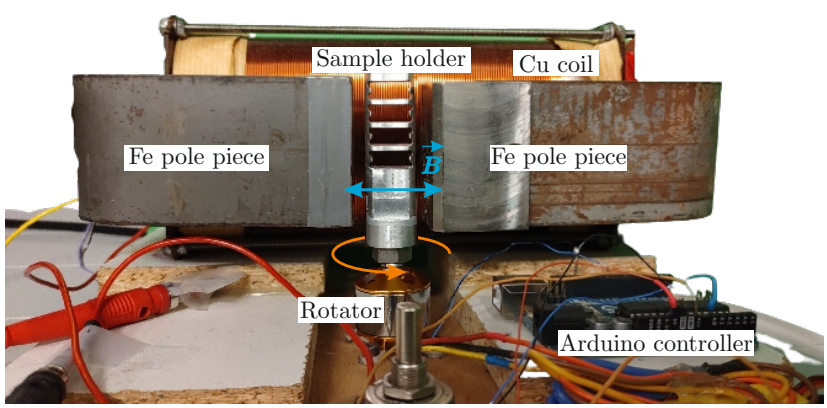

Figure 2.8: Demagnetisation stage set-up. The electromagnet made from a copper coil and iron pole pieces has a gap for the sample holder. Inside this gap, the magnetic field points in-plane respective to the sample position. There is a possibility to demagnetise up to four samples simultaneously. A programmable keysight waveform generator controls the electromagnet and magnetic field it produces. At the same time, the rotation of the sample holder is controlled by the Arduino controller.

[10]The length of the demagnetisation varies and will always be mentioned with the experiment results.

Thermal demagnetisation

There are two ways to use thermal demagnetisation if an artificial system is thermally active. The first way is to use superparamagnetic effects by reducing the blocking temperature of the nanoparticles [31–35]. The blocking temperature T_B is the temperature needed to overcome the energy barrier and change the magnetisation from one initial easy axis[11] direction through the out-of-plane hard axis into the other possible easy axis direction. T_B is proportional to the volume V and anisotropy energy density K of the nanostructure. Therefore, one way to make nanoislands superparamagnetic is to adjust their volume and make them small enough or use special material compositions to lower the anisotropy energy density and decrease the blocking temperature. This approach requires very small objects, but working with the thermal demagnetisation allows the system to fluctuate thermally while still maintaining the Ising-like character of the nanoislands.

The second thermal demagnetisation is done by heating the sample above the Curie temperature T_C [36–39]. Heating the sample above T_C causes magnetisation loss due to the phase transformation from the ferromagnetic phase to the paramagnetic phase. The system is re-magnetised as the paramagnetic system is cooled below the T_C. The disadvantage of demagnetising the sample via heating and cooling the system through the Curie point is that the interactions between nanomagnets variates both in amplitude and direction (as the magnetisation of the nanoislands is not Ising-like near the T_C) as the re-magnetisation does not occur everywhere at the same time.

2.4. Measurement and data analysis

After the sample is fabricated and demagnetised, magnetic imagining of the resulted spin configuration needs to be conducted. The main advantage of artificial spin systems is that orientation of each individual macrospin within the lattice can be measured, in case of athermal samples the measurement can be done at room temperature and without the need for a vacuum.

There are several magnetic imaging techniques that can be used for measuring the real space magnetic configuration such as *Magnetic force microscopy*, *Photoelectron emission microscopy* (PEEM) or *Lorentz transmission electron microscopy* (L-TEM). The techique that suited best our needs is MFM.

2.4.1. Magnetic force microscopy

MFM is one of the *scanning probe microscopy* (SPM) techniques based on measuring the local property of the sample by detecting the interaction between a magnetic probe and the magnetic stray field emanating from the magnetic structures.

[11] In case of a majority of the studied artificial spin systems, the easy axis is along the longest axis of the nanoparticle.

Principle of MFM

MFM is a two-pass method based on *atomic force microscopy* (AFM). Specially designed probes are used to acquire the desired information from the sample. The principle of the probe data acquiring is shown in Figure 2.9. It is a cantilever with a sharp tip at the end. For the MFM technique, the tip needs to be coated with some magnetic material, such as CoCr, or NiFe, to interact with the stray field of the sample.

In the first pass, the probe measures the sample's topography by measuring the attractive and repulsive forces near the sample surface where the van der Waals forces dominate [40]. For acquiring the topography of the sample, the tapping mode was used. In this mode, the probe oscillates near its resonance frequency and is in contact with the sample at its lower position during the oscillation. The sample resonance is controlled by a piezoelectric crystal, which is set to resonate with a set amplitude. If the sample topography changes (for example, if the structure appears or disappears), the actual amplitude of the oscillation changes and the feedback loop changes the applied voltage on the piezoelectric crystal to change the scanning height of the probe. The voltage applied to the piezocrystal is then used to calculate the real changes in topography. The principle of AFM measurement is in Figure 2.9 a). Getting as precise information about the surface as possible is essential to neglect any artefacts in the second pass when the magnetic field detections occur.

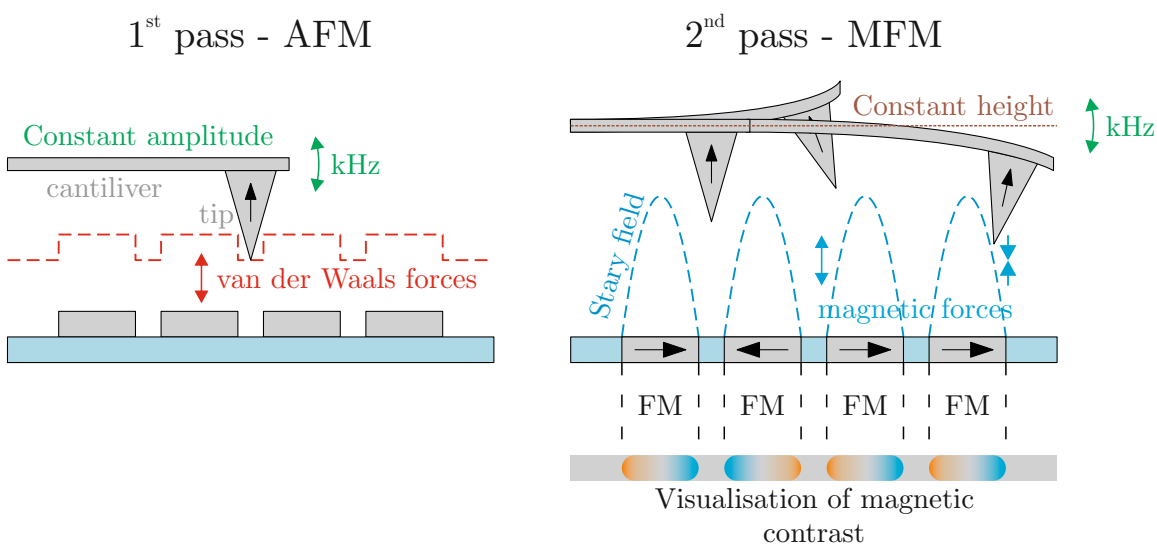

Figure 2.9: Two-pass measurement of MFM. a) Acquiring the topography by using standard AFM. b) The interaction between the magnetic tip and stray field of ferromagnetic (FM) domains at a constant height above the sample. The stray field causes a phase shift of the oscillating cantilever. The measured phase shift is a visualisation of the sample's magnetisation.

In the second pass, the tip is lifted above the sample where magnetic interactions are stronger than the van der Waals forces [40]. The probe is kept at a constant height above the sample[12], and the interactions between the stray field of magnetic domains and magnetic tip are measured. The probe is oscillating in the second pass, and magnetic forces that act on the tip and cantilever change the phase of this oscillation. This phase shift visualizes the magnetisation of the ferromagnetic domain in the sample. The second

[12]Cantilever copies the trajectory that was acquired in the first pass.

pass of MFM measurement can be seen in Figure 2.9 b). Many reviews have been written about these techniques, such as [41] for AFM and [42] for MFM.

AFM and MFM are well-known techniques. The instrument setting and different measurement modes are widely described in the literature. Investing time into finding suitable modes and probes for each individual set of systems is crucial. The measurements described in this thesis were done either on *NT-MDT Ntegra* or *Scanning Probe Microscope Bruker Dimension Icon* microscopes. We used commercial probes MESP-V2 from Bruker company with Co-Cr magnetic coating. These tips have a tip radius of around 35 nm.

Even though MFM can yield quantitative results, our measurements were done to acquire qualitative information about the samples from which the spin configuration of all lattices can be derived.

2.4.2. Acquiring qualitative data

Since our modified lattice for the kagome and the square systems are connected, we are not measuring the stray field of individual nanomagnets but the domain wall (DW) at each vertex site. From these domain walls, we can estimate the spin configuration of all three (in the case of kagome lattice) or four (in square lattice) connected nanomagnets.

To determine the spin configuration from the DW's shape and intensity, we first run MuMax^3 simulations to see how specific spin configurations form the stray field. The examples of possible DW shapes are shown in Figure 2.10. The domain walls can be rotated, and the micromagnetic texture can be reversed, but in principle, these examples represent all possible observable DW types.

In the kagome lattice, there are only two types of DWs. The low-energy ground state spin configuration is shown in Figure 2.10 a), where the magnetisation split around the notch. The high-energy spin configuration is the configuration where the magnetisation goes around the notch, shown in Figure 2.10 b)[13]. The simulated MFM signal for the ground state configuration results in a symmetric "heart shape" like the stray field. This DW shape is also measured by MFM, recognisable by its symmetry but mainly by no spike in intensity. On the other hand, the high-energy spin configuration is asymmetric both in simulated MFM and real measured signals. However, mainly the change in intensity in one part of the DW and the presence of the opposite (black/white) colour in the DW can be observed.

The square lattice has more types of possible DWs. The Type I domain wall is shown in Figure 2.10 c). This domain type is formed by spin configuration where two spins point into and two outside the vertex. The first neighbours (nanomagnets connected at an angle of 90°) have a "head to tail" spin orientation, and the domain wall have a characteristic "bow-tie" shape. This DW also has the lowest contrast of all types possible in our modified lattices. Therefore especially with large scans, this type of DW is often undetected or very poorly visible compared to other possibilities. There are only two ways this bow-tie DW can look: the light bow tie is oriented horizontally or vertically.

[13]The possible three-in/three-out configurations were so unstable that they always collapsed into two-in/two-out configurations, and we never observed them experimentally in our systems.

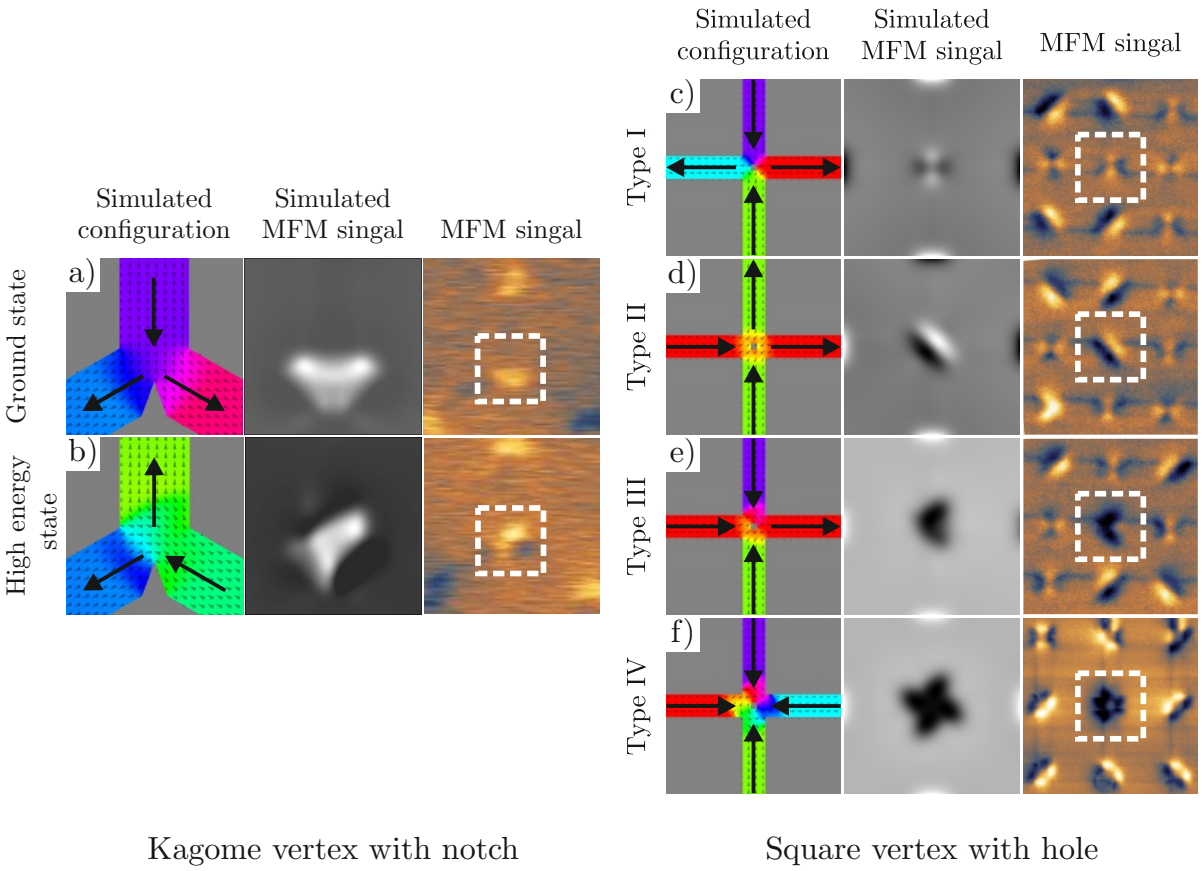

Figure 2.10: Comparison of simulated spin configuration and resulting domain wall signal with real measured MFM signal of the kagome vertex with notch with a) ground state spin configuration, b) high-energy spin configuration and the square vertex with hole for c) Type I, d) Type II, e) Type III and d) Type IV spin configuration.

The Type II spin configuration is also made from two spins pointing inside the vertex and two outside, but the second neighbours now have a "head to tail" orientation. This DW is, therefore, polarised and has a characteristic two-colour ellipse-like shape. Contrary to Type I, Type II has a strong magnetic signal in simulations and real measurements. There are four possible spin configurations resulting in Type II DW. The ellipse can lean to the right or left side, and the white part can be both on top or the bottom of the ellipse.

The Type III configuration is made from three spin pointing inside or outside the vertex. Type III is a transverse domain wall, and there are eight possible spin configurations forming Type III with "heart shape" DW. Four configurations where one spin is pointing in and four where one spin is pointing outside of the vertex.

Type IV forms the DW, where all four spins point in or outside the vertex. There are only two possible ways spins can make Type IV DW, the four-in or four-out configurations.

It must be said that both Type I and Type IV configurations in our connected lattices have out-of-plane magnetisation at the centre of the vertex. Therefore these two types would have high-energy, and without the hole defect at the centre of the vertex, they would be unstable. Therefore, removing the area where this out-of-plane magnetisation would appear helps us stabilise these configurations. However, even with the centre removed in

the vertex, the Type IV have much higher energy than the rest of the types. The only real space image of stabilised Type IV vertex visible in Figure 2.10 f) has been captured but only on the lattice with so many defects, making it unusable for research. However, these defects also made stabilising this rare configuration possible.

The proper discussion about the defects at the vertex site and the energies of individual DW will be discussed in Chapter 3 for the kagome lattices with notches and Chapter 4 for the square system with holes.

There are examples of how the AFM/MFM measurement outputs look for both types of lattices, as shown in Figure 2.11. AFM and MFM outputs were analysed and pre-treated with Gwyddion data processing software. The AFM outputs can give us information about the quality of the surface (whether there are some impurities) and the completeness of the lattice. It can be seen that in the kagome lattice, there is a nanomagnet missing in the bottom right corner. Except for the quality of the lattice, the AFM measurement does not provide any information about the spin configuration; however, knowing the exact topographic can explain some unusual magnetic contrast in MFM measurements. The white bar indicates the length of $3\,\mu$m. Depending on the sharpness of the tip and on the lattice parameters, hole defects can be observed. On the other hand, in kagome lattices with notches, the notches are often hard to observe because the lattices are quite large, and to acquire many results, the measurement was done with relatively fast scanning and a large step size. Measurement was always set up to acquire the highest quality MFM images within a reasonable time frame (each measurement took around 50 minutes).

The interaction between the magnetic probe and the stray field of the sample is measured by the phase change of the probe's oscillation. Therefore the false colour scale shows the change in degrees. Where there are negative phase changes, the tip is attracted by the lattice via the magnetic field and vice versa for the positive changes. We are not measuring the direct magnetic orientation in the lattice but its interaction with the tip. Therefore if the tip was magnetised in the opposite direction, the measured contrast would also be reversed.

From the shapes of the measured DW in the MFM image, the spin configuration across the lattice can be determined as shown in the bottom panel of Figure 2.11.

The spin configuration of the square lattice is accompanied by the colour visualisation of the individual types of vertex configurations. The analysis can be done by hand, but it is a time-consuming process where many mistakes can be made. For this purpose, an in-house build software and scripts were programmed by Ioan-Augustin Chioar (PhD 2015), Yann Perrin (PhD 2016) and Vojtěch Schánilec.

2.4.3. Acquiring quantitative data

After measuring the spin configuration, the analysis is done to determine whether the system is at- or out-of-equilibrium, how fitting the physical framework (Hamiltonian) used in describing the system is, and what phase within the predicted thermodynamics profiles the system captures.

The process of the spin configuration analysis we use in our research is described in the following paragraphs.

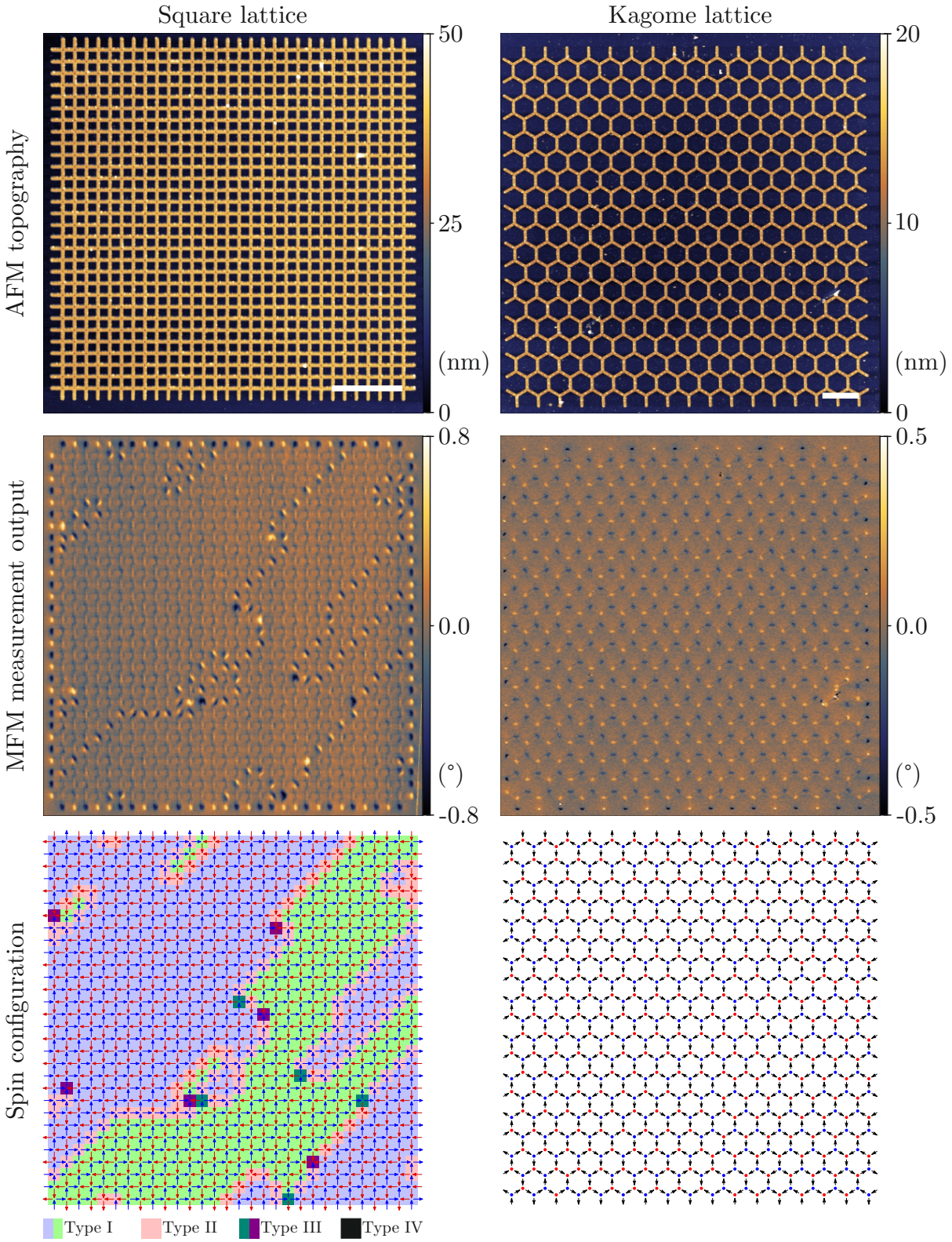

Figure 2.11: An example of measurement output from AFM and MFM on a square system with holes and kagome with notches. In the top panel are topographies of the lattices acquired with AFM. The white bars indicate the length of $3\,\mu$m. In the middle panel, MFM images show the domain wall formation at each vertex site. The bottom panel shows the visualisation of the spin configuration for the measured lattices.

The vertex population count

One way to analyse the system, which can be directly taken from real space images of spin configuration, is the vertex population count as shown in [26, 33, 43]. This method can be easily used for the system with perfectly ordered ground state order. The vertex population can then provide information about how far the system is from being in its ground state. In systems where the long range interactions are neglected, the system's total energy is directly counted as the sum of the energy of each vertex. However, this type of analysis has some limitations.

There are only a few artificial spin systems where long range interactions can be neglected. Therefore, calculating the system's total energy simply by summing up different types of vertices is only a rough approximation in most systems.

Pairwise spin correlation

Another type of analysis calculated from the real space images is the computation of the pairwise spin correlations. The correlations present a convenient way to see how the state of a given spin determines any other in the lattice. Pairwise correlations between the spin $\boldsymbol{S}_i$ and $\boldsymbol{S}_j$ are calculated as:

$$C_{ij} = \langle \boldsymbol{S}_i \cdot \boldsymbol{S}_j \rangle \,, \tag{2.16}$$

where $\langle\rangle$ indicates that the scalar product is averaged over all pairs of spins. It is particularly useful to compare the pairwise correlations calculated from the experiment $C_{\alpha j}^{\mathrm{exp}}$ with the correlations predicted by simulations. Monte Carlo simulations can be used to calculate these correlations $C_{\alpha j}^{\mathrm{MC}}$ for any desired Hamiltonian. Correlation coefficients are usually temperature dependent. To see if the measured spin configuration is, in fact, in-equilibrium and captures the physics of the predicted model, it is helpful to use the spread-out function defined as:

$$K\left(T\right) = \sqrt{\sum_j \left[C_{\alpha j}^{\mathrm{exp}} - C_{\alpha j}^{\mathrm{MC}}\left(T\right)\right]^2}. \tag{2.17}$$

By finding the minimum of this spread-out function, the effective temperature of the measured system can be estimated. If all experimental correlation coefficients fit within the deviation of the simulated coefficients, the system seems to be in-equilibrium. As Chioar et al. showed, comparing the simulated and measured pairwise spin correlations is extremely useful in recognising the type of physics that governs the system. They also determined that the kagome system with out-of-plane magnetisation is governed by long range interactions, which have non-neglectable effects [44]. It also helps them to recognise that the kinetics of demagnetisation protocol can cause correlations deviations [45]. In Figure 2.12 there is an example of the comparison taken from [44] of the experimental (dots) and Monte Carlo simulated correlation coefficients of the thermally demagnetised kagome dipolar spin ice system. The spin-spin correlation for the seven nearest-neighbour from measurement fall on the simulated curves at effective temperature[14] 0.05. The

[14]Temperature normalised to the coupling strengths of the nearest neighbour $J_{\alpha\beta}$.

correlation coefficients deviation of $C_{\alpha\delta}$ and $C_{\alpha\nu}$ is caused by the demagnetisation process [44].

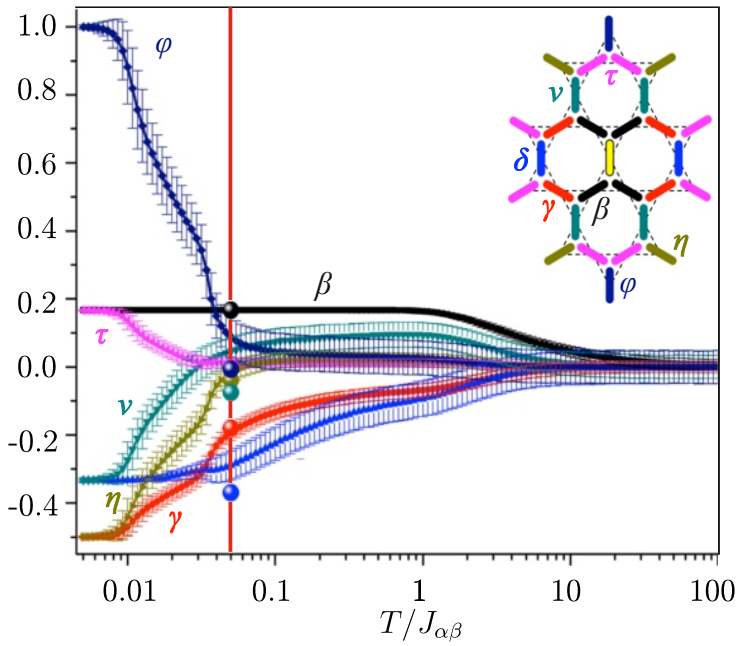

Figure 2.12: Comparison of measured (dots) and simulated pairwise spin correlations $C_{\alpha j}$ for the seven nearest-neighbours. The simulations were done with the kagome dipolar spin ice Hamiltonian. The system's effective temperature ($T/J_{\alpha\beta}$) was estimated from the comparison to be around 0.05. The deviation of the $C_{\alpha\delta}$ and $C_{\alpha\nu}$ correlation coefficients are attributed to kinetic effect during the (de)magnetisation process [18, 44]. Different pairwise correlations are distinguished by the different colours as visualised in the legend. Taken and edited from [44].

If the experimental and simulated coefficients do not match, it can be caused by the following things:

- The measured system is not in thermal equilibrium.
- The system is in equilibrium, but the simulations were done with the wrong Hamiltonian, and therefore the physics of the system is not the same as the simulated one.

Magnetic structure factor

Another way to represent the spin configuration and order is to calculate the *magnetic structure factor* (MSF). MFS is obtained by calculating the Fourier transformation of pairwise spin correlations. The MSF shows the magnetic diffraction patterns associated with the real space magnetic state. Similarly to comparing the correlation coefficients with the predicted outcome, the MFS can be used to identify in which phase the measured sample is. These patterns are similar to the diffraction patterns acquired by neutron diffractions on spin ice crystals.

MSF is a useful tool for visualising the order or disorder of the system. If the system is ordered, the MSF shows magnetic Bragg peaks in reciprocal space. However, a diffused

background signal is seen if the system is disordered. Examples of four different MSFs are shown in Figure 2.13, where three different ordered and one disordered states of the square spin system are shown. If the system is ordered, the intensity of the MSF signal is larger by an order of magnitude then the disordered one as is shown in Figure 2.13. The ordered states are easily distinguishable simply by comparing the position of the magnetic Bragg peaks in reciprocal space. The antiferromagnetic ordering is built by Type I vertices everywhere. The polarised state has only Type II vertices, but they are all ordered in one direction, and the Manhattan order has only type II vertices as well, but it is built by two perfectly alternating saturated sub-lattices. On the other hand, in the disordered spin liquid phase, the Type I and Type II vertices are almost randomly distributed.

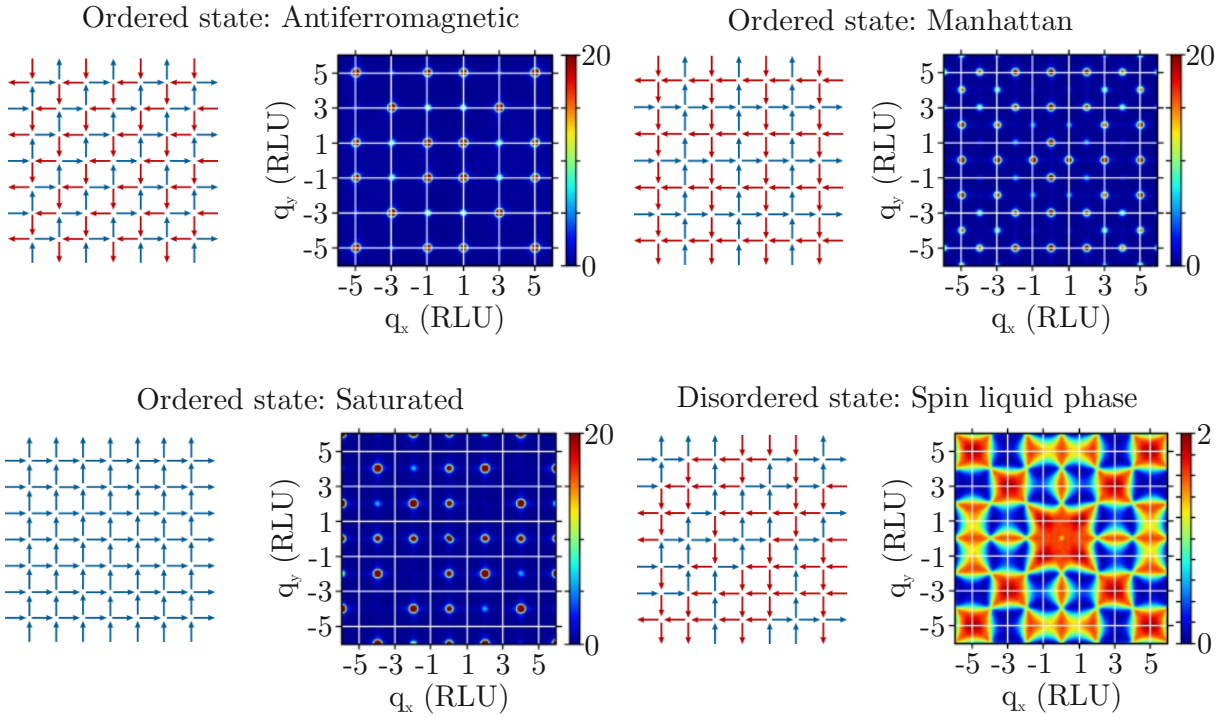

Figure 2.13: Example of three different ordered and one disordered spin configuration of the square spin system with their associated magnetic structure factors. The ordered states have high-intensity Bragg peaks in their space, and the disordered state shows no Bragg peaks but a low-intensity diffused background signal. Taken and edited from [46]

.

All MSF calculated for the square spin systems are done by Yann Perrin's code developed during his PhD studies. A deep description of how MSF is calculated is described in Perrin's PhD thesis [46]. Examples of how the MSF analysis can distinguish differences even in the configurations with the same or similar vertex populations can be seen in [18].

The MSF will accompany all research results presented in this work since it is a powerful tool for determining how the system is ordered or disordered.

2.5. Overview of the experimental process

The whole process of our experiment is summarised in the diagram in Figure 2.14 showing all the involved steps. At the beginning of the process, series of micromagnetic simulations are made to see how the defects in geometry we use (notches and holes) control the micromagnetic energy of our system. In the case of the kagome lattice with notches, Monte Carlo simulations are used to determine how the spin configuration of the desired phases should look like. These simulations are then used to design proper lattice layouts.

After the layouts of the lattices are designed, the samples are fabricated using the EBL technology. The samples are demagnetised by field-driven demagnetisation and then measured by MFM.

Raw MFM data are post-processed via Gwiddyon software and then analysed by a series of in-house software and scripts. Both kagome and square toolkits made by me are used to determine the vertex types all over the lattice. The outputs of my toolkits are spin configurations exported in a format compatible with Chioar (used for the kagome system) and Perrin (used for the square system) toolkits.

The reason why my toolkits were made is twofold. Firstly, it is easier and faster to analyse the configuration of the DW at the vertex site and then determine the magnetisation of each macrospin. Secondly, the toolkits offer an easier way to repair analysis mistakes. Via both toolkits, the analysis of one MFM image is done in approximately 10 minutes, whereas manually doing this work takes more than 90 minutes.

Chioar and Perrin toolkits were programmed by Yann Perrin and Ioan-Augustin Chioar during their PhD studies. These toolkits are handy for data analysis. The inputs for these toolkits are spin configurations, and from them, the spin configuration map, pair-wise correlations, vertex population and distribution and MSF are calculated. All these mentioned tools are then used for data interpretation.

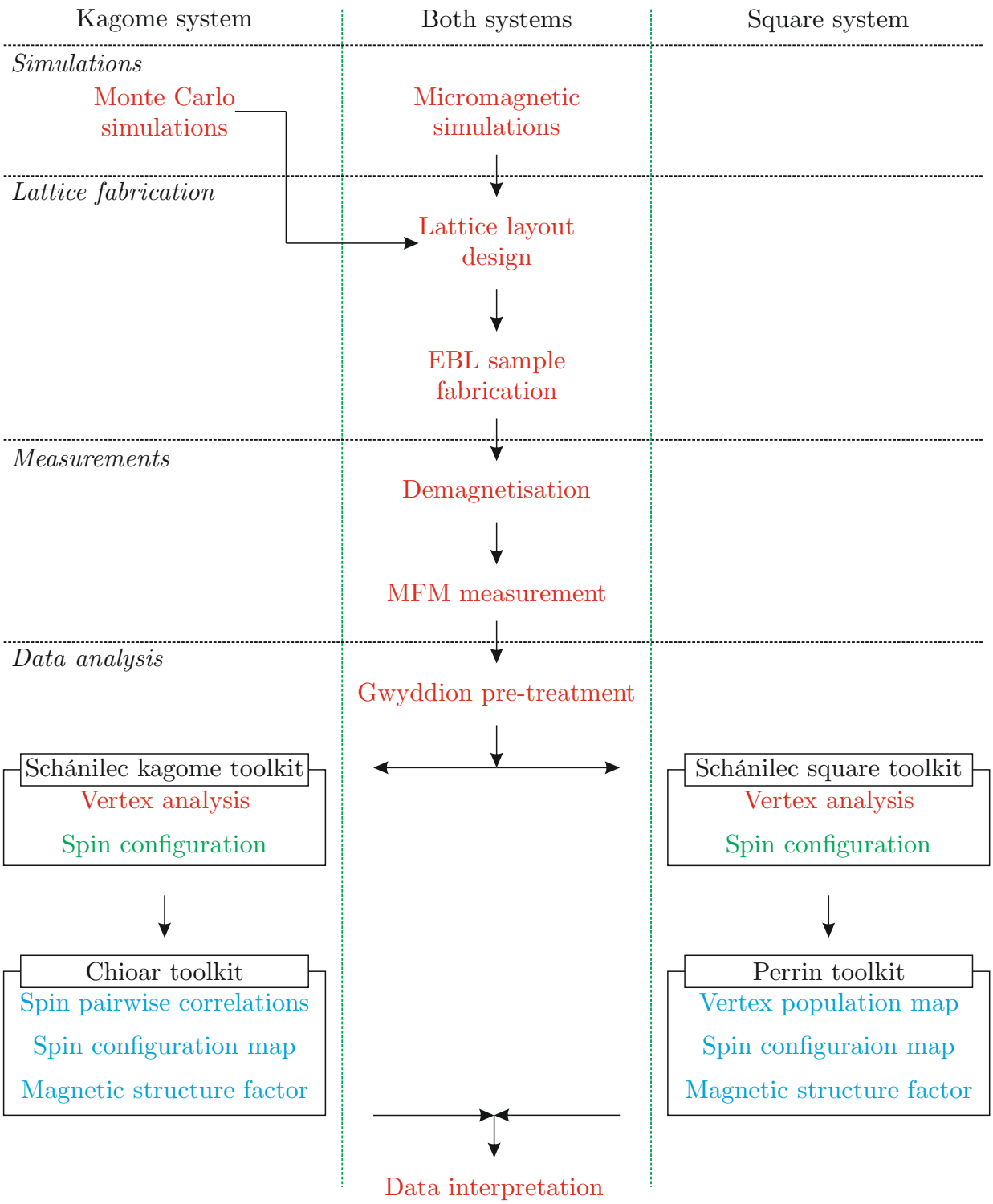

Figure 2.14: Diagram of the experimental process used for the experiments described in this thesis. The colour code in the diagram is the following: the red-coloured steps need to be done manually. The green ones are done automatically and are used as inputs for Chioar and Perrin toolkits. The blue items are the ones we are using for the data interpretation.

Chapter 3: Artificial kagome spin system with notches

One of the ways how to transform a 3D spin ice crystal into a 2D lattice is to use vertex projection, as was discussed in section 1.3.2. This transformation results in two-dimensional kagome geometry that will be the main focus of the following sections. First, the introduction of possible models 3.1 describing the physics of such geometry will be made, followed by examples of possible realisation in 3.2. The challenges tied with probing the artificial kagome spin systems are discussed in sections 3.3 and 3.4 and our suggestion on how to overcome them will be introduced in section 3.5 supported by experimental and numerical analysis.

3.1. Introduction to the kagome models

Two main possibilities for building a system on this projection are with out-of-plane or in-plane orientation of Ising variables. Furthermore, depending on the range of interaction models can be divided into short and long range models. All of these combinations will be described in following sections.

3.1.1. Short range kagome models

If only the nearest neighbours in the model affect each other and do not affect the farther neighbours, the system is considered short range. In kagome geometry, there are two main short range models with similar properties but different spin orientations.

The kagome Ising antiferromagnet

The first model can be acquired by placing an out-of-plane spin at each triangle's apex, as shown in Figure 3.1 a). All spin axes are parallel with a unit vector $\boldsymbol{e_z}$ pointing out-of-plane. This system is called *kagome Ising antiferromagnet* (kIa), and it is one of the first studied two-dimensional classical **spin liquids** [47,48]. The Hamiltonian describing kIa behaviour can be written as:

$$H = -J \sum_{\langle ij \rangle} \boldsymbol{S}_i \cdot \boldsymbol{S}_j, \tag{3.18}$$

where J is the negative [15] coupling strength constant between spins $\boldsymbol{S}_i$ and $\boldsymbol{S}_j$. Every spin points along the same direction of unit $\boldsymbol{e_z}$, as shown in Figure 3.1 a). Therefore spins can be re-written as $\boldsymbol{S}_i = \sigma_i \cdot \boldsymbol{e_z}$, where σ_i is scalar indicating whether the spin points parallel (+1) or anti-parallel (-1) with unit vector $\boldsymbol{e_z}$.

Due to the negative J, the interaction between pair of spins is minimised if the spins are oriented antiferromagnetically. Because of the system's geometry, there are always

[15] As well as the exchange energy between spins in antiferromagnetic materials.

three spins at the vertex site. The combination of interaction and geometry results in frustration; hence there is no possible spin configuration that minimises all interaction between nearest neighbours. Each vertex is therefore frustrated, as is shown in Figure 3.1 b), where the red line shows pair of spins with unsatisfied interaction. There are six possible low-energy configurations where one interaction is unsatisfied, but two are minimised (in blue frame). These configurations follow the so-called *kagome ice-rule*[16] [12] and are ground state configurations. The two possible high-energy configurations with all three spins parallel are high-energy excitation of this model (red frame).

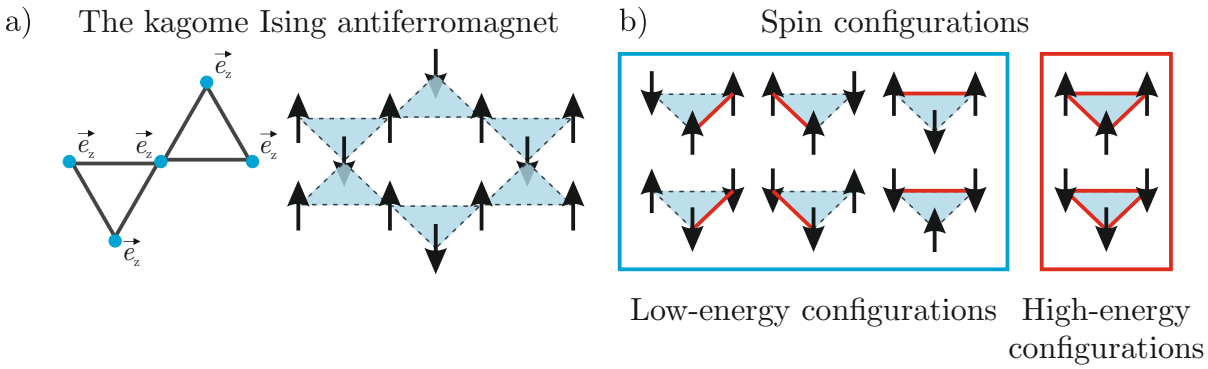

Figure 3.1: a) Ising variables - spins (black arrows) are placed at each triangle's apex of kagome geometry parallel to the unit vector $\boldsymbol{e_z}$ (blue), which points out-of-plane forming kagome Ising antiferromagnet. b) Interaction between first neighbours is satisfied if the first neighbours are ordered antiferromagnetically. There are six low-energy ground state spin configurations with only one unsatisfied interaction (in the blue frame) between the nearest neighbour at the vertex site and two high-energy configurations with all three interactions unsatisfied (in the red frame). Unsatisfied interactions are highlighted with red lines.

From a thermodynamic point of view, kIa model is described by two different temperature regimes separated by crossover [48, 49]. Suppose the system's temperature is larger than the coupling strength constant, i.e. when $T/J \gg 1$ system is in *paramagnetic state*. Due to the system's high-energy, spins can fluctuate without limitations, and ice-rule constraint is not present. All types of spin configurations shown in 3.1 b), even the high-energy, are possible. Spins fluctuate between both possible (up/down) directions equally, and they are therefore uncorrelated and zero on average.

As the system's temperature is cooling down, the system starts to correlate at the short range, introducing the kagome ice-rule while minimising the energy of the nearest neighbour interaction. Furthermore, when the $T/J \ll 1$ condition is met, the system enters the *cooperative paramagnet state*. Spins still fluctuate highly [19], but short-term correlations appear as every triplet of the nearest neighbour strives to minimize all the interaction. Therefore only low-energy ice-rule obeying configurations are present. Magnetic susceptibility of the systems is proportional to $1/T$ [50] in accordance with *Curie's law*.

[16] Ice-rule states that ground state of water ice is reached if two of four hydrogen atoms surrounding oxygen atom are *in* (closer) and two are *out* (farther) as explained in section 1.3.1. The kagome ice-rule is a modification of this rule for three Ising spins: two-in (one-out) or two-out (one-in).

The kagome multiaxial Ising ferromagnet

The second model consists of in-plane spins placed onto the apex of each triangle of the kagome lattice, as shown in Figure 3.2 a). In this system, the spin axes of first neighbours are at a 120 ° angle therefore there are three unit vectors $\boldsymbol{e_0}$, $\boldsymbol{e_1}$ and $\boldsymbol{e_2}$. Hence this system is called *the multi-axial kagome system* (kmIf) or *kagome spin ice* (ksi). The latter is more often used in literature therefore, it will be used further on.

Because of the in-plane spin orientation, the energy of the spin couple is minimised if their configuration is head to tail. The Hamiltonian describing behaviour of ksi is:

$$H = -J \sum_{\langle ij \rangle} \boldsymbol{S}_i \cdot \boldsymbol{S}_j, \tag{3.19}$$

where J is the positive[17] coupling strength constant between spins $\boldsymbol{S}_i$ and $\boldsymbol{S}_j$.

Like the kIa system, ksi minimises its energy if the vertices follow the *modified kagome ice-rule*, meaning that the energy is minimised if two spins point into/outside the vertex. All other cases are high-energy ice-rule-breaking configurations. Every possible spin configurations are shown in Figure 3.2 b).

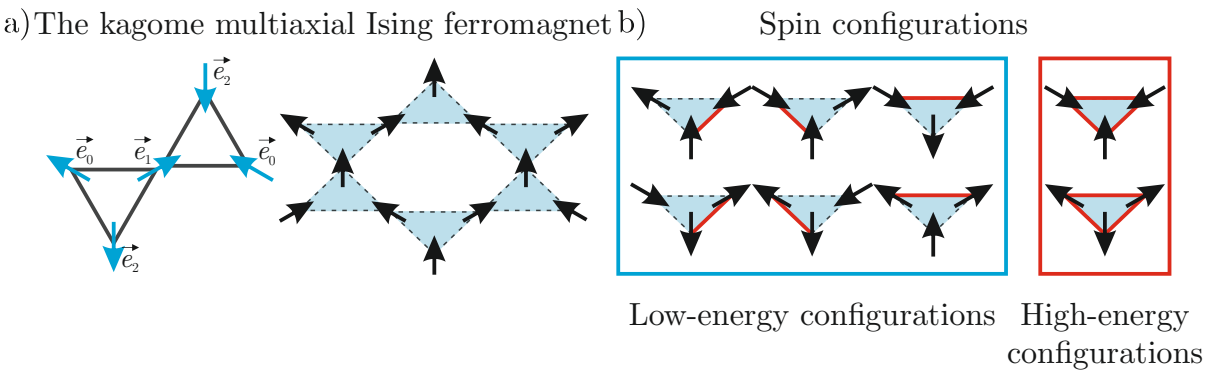

Figure 3.2: a) Ising variables - spins (black arrows) are placed at each triangle's apex of kagome geometry parallel to the in-plane unit vectors $\boldsymbol{e_0}$, $\boldsymbol{e_1}$ and $\boldsymbol{e_2}$ (blue arrows) pointing inside (or outside) of kagome vertex, forming kagome multiaxial Ising ferromagnet. b) Interaction between first neighbours is satisfied if the first neighbours are ordered ferromagnetically (head to tail). There are six low-energy ground state spin configurations (in the blue frame) with only one unsatisfied interactions between the nearest neighbour at the vertex site and two high-energy configurations (in the red frame) with all three interactions unsatisfied. Unsatisfied interactions are highlighted with red lines.

The thermodynamic profile of the ksi is the same as kIa. Therefore kIa and ksi can be directly mapped onto each other if only the first neighbour interactions are considered. This statement can be supported by comparing pairwise correlation coefficients of the first seven neighbours. The correlation coefficients were calculated by using Monte Carlo simulations see Table 3.2 [18, 44].

Pairwise correlation coefficients: β, γ, τ, η differ by a factor $-1/2$, which can be explained by visualising the configuration of the nearest neighbours for both systems as shown in

[17] It is similar to the ferromagnet exchange energy, hence the name.

Table 3.2: Theoretical values of the pairwise spin correlation coefficients C_{ij} for first seven nearest neighbour in kagome Ising antiferromagnet and kagome spin ice for low-energy configuration. Values are calculated by using Monte Carlo simulations. These correlation coefficients are temperature-independent.

C_{ij}	$\alpha\beta$	$\alpha\gamma$	$\alpha\nu$	$\alpha\delta$	$\alpha\tau$	$\alpha\eta$	$\alpha\phi$
n^{ith}	1	2	3	3	4	5	6
Kagome Ising AF	-0.333	0.124	0.101	-0.075	-0.024	-0.038	0.023
Kagome spin ice	0.167	-0.062	0.101	-0.075	0.012	0.019	0.023

Figure 3.3. While in kIa all axis of possible spin directions are parallel and therefore the spins can be either fully correlated (+1) or fully anti-correlated (-1). In ksi the mentioned neighbours to α have their axis under 120 ° and since the correlation is the cosine of the angle between two spins (axis), the factor $-1/2$ is present.

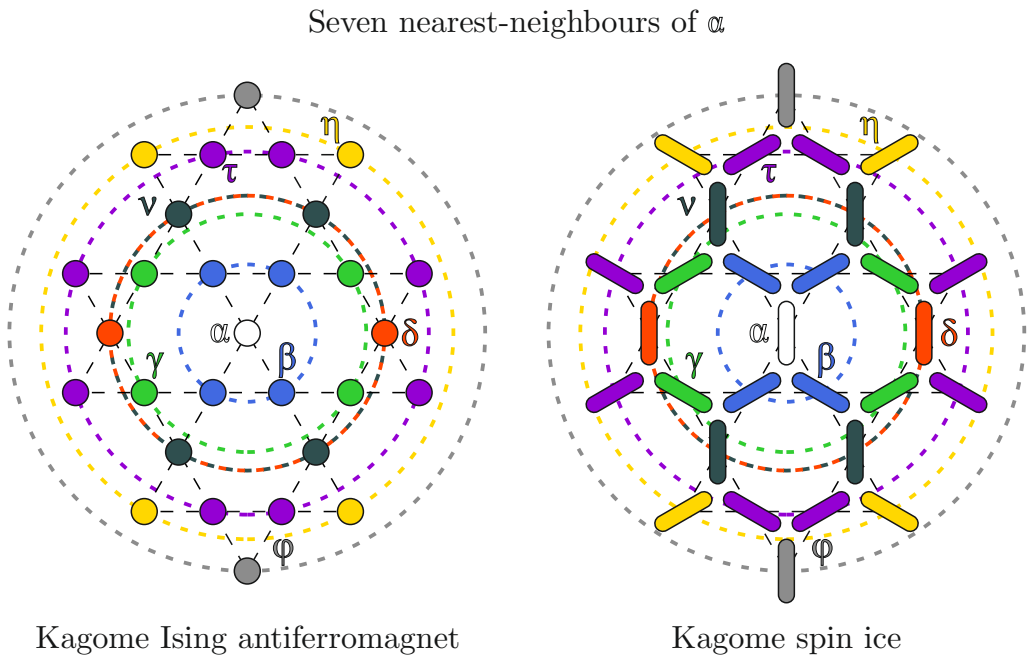

Figure 3.3: Schema of position and ordering of the first seven nearest neighbours for both kagome Ising antiferromagnet and kagome spin ice. The colour circle's radius indicates the centre-to-centre distance between individual spin positions. The order of the first seven nearest neighbour is as following from closes to farthest from α (white) position: β (blue), γ (green), ν (dark green) and δ (red) at the same distance, τ (purple), η (yellow) and ϕ (gray).

3.1.2. Long range kagome models

Previous models were almost identical and could be directly mapped onto each other, but only if further neighbour interactions were not considered. This mapping is no longer possible if long range dipolar interactions are introduced into the model and further neighbours interact with each other. The long range couplings enrich the phase diagram

of both kagome networks [44] with new magnetic textures. Hamiltonian for long range dipolar kagome models can be written as:

$$H = -\frac{D}{2}\sum_{(i,j)}\left[\frac{3\left(\boldsymbol{S}_i\cdot\boldsymbol{r}_{ij}\right)\left(\boldsymbol{S}_j\cdot\boldsymbol{r}_{ij}\right)}{r_{ij}^5} - \frac{\boldsymbol{S}_i\cdot\boldsymbol{S}_j}{r_{ij}^3}\right], \tag{3.20}$$

where D is the dipolar constant, $\boldsymbol{S}_i$ and $\boldsymbol{S}_j$ are spins placed on positions separated by distance vector $\boldsymbol{r}_{ij}$.

The kagome dipolar Ising antiferromagnet

The addition of the long range dipolar interaction in the kIa model changes its behaviour immensely. Even though there has been some research done [44, 51, 52] on the kagome dipolar Ising antiferromagnet (kdIa), some questions are still unanswered, such as the number of phases and phase transitions and spin dynamics that need to occur to overcome critical freezing before reaching the ground state [18].

The thermodynamic profile of the kdIa consists of a high-energy disordered and uncorrelated paramagnetic phase at high temperature and as the systems cool down into the spin ice phase, all triangles respect the kagome ice-rule. Inspired by the behaviour of kagome dipolar spin ice, Chioar et al. used Monte Carlo simulations to explore the low-energy configuration of kagome dipolar Ising antiferromagnet. They found out possible ground state candidate for kdIa. This candidate has lower energy than any previously reported ground states while having ordered spins and perfect *magnetic charge* configuration, as is shown in Figure 3.4. The sum of spins parallel to unit vector in the vertex (+1) or antiparallel (-1) is usually called magnetic charge.

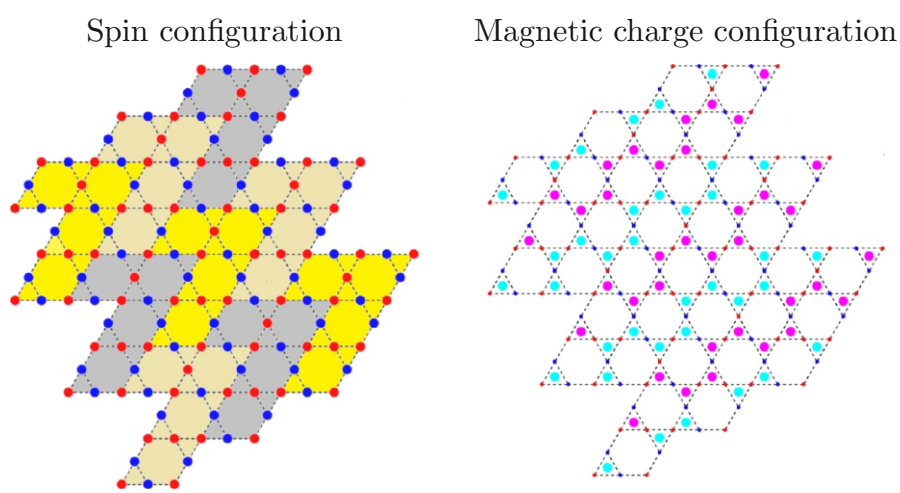

Figure 3.4: Spin configuration of the 7-shape phase (left) and resulting magnetic charge (right). The presence of long range order interaction orders the spin configuration, and the proposed ground state for kdIa system is built by 7-shaped unit cells, hence the name. Magnetic charge exhibit perfect ordering as well in the form of a string of vertices with +1 or -1 charge configuration (purple or light blue circles). Taken and edited from [52].

The kagome dipolar spin ice

The kagome dipolar spin ice (kdsi), on the other hand, is a model with a well-known thermodynamic profile that hosts many interesting many-body phenomena such as emergent charge crystallisation in low-energy phases [53–55], Coulomb phase physics [56–58] and fragmentation of the spin [55]. As a consequence of the long range dipolar interaction, the phase diagram of kdsi is richer and more exotic than ksi described in section 3.1.1. Monte Carlo simulations show a two-stage ordering process happening at low temperature, revealing two different ordered phases.

The thermodynamics of kdsi consists of four regimes [55,59,60]. Those phases are following from the highest energy phase to the ground state phase: *Paramagnetic phase* (PM), *Spin liquid 1 phase* (SL1), *Spin liquid 2 phase* (SL2) and *Long range order phase* (LRO). The high-energy PM phase resembles that of ksi. Spins in PM phase are uncorrelated and disordered. Spins in SL1 phase obey the kagome ice-rule, but SL1 phase is different than the short range kagome spin ice phase. Correlation coefficients of SL1 are temperature dependent. Monte Carlo simulations uncovered another two phases SL2 and LRO, with different ordering rules at low temperature.

The most interesting phase of kdsi phase profile is the SL2 phase because the magnetic charge of this phase is perfectly ordered, and spins lying on top of this magnetic charge crystal are ordered and disordered at the same time. This behaviour is caused by the phenomenon called *fragmentation of the spin*. Part of the spin needs to be static, so it forms the magnetic charge crystal, and part of the spin fluctuates on top of this crystal and causes a disordered in spin configuration.

In the LRO phase, which is ground state of the kdsi, spins and magnetic charge are perfectly ordered and no spin fluctuation is allowed.

The summary of different properties of each phase i.e. pin ordering, spin correlation and magnetic charge ordering, is shown in Table 3.3. Since our research is focused on kdsi and its challenges, all of the phases will be explained in more detail in section 3.3.

Table 3.3: Spin, spin correlation and magnetic charge properties for each of the four kdsi phases. The phases are ordered according to the effective temperature of each phase: $T_{\mathrm{LRO}} < T_{\mathrm{SL2}} < T_{\mathrm{SL1}} < T_{\mathrm{PM}}$.

	Long Range Order	Spin Liquid 2	Spin Liquid 1	Paramagnetic
Spin	Order	Order-Disorder	Disorder	Disorder
Spin correlation	Correlated	Correlated	Correlated	Uncorrelated
Magnetic charge	Order	Order	Disorder	Disorder

Even though the phases of kdsi are well-known and theoretically proven, there is a problem in the designing system which would capture the physics of low-energy phases on a large scale in real space. It is excellent motivation to find a way to design such a system so we can study the real space global and local properties and analyse the system's behaviour.

3.2. Artificial realisation of kagome models

Artificial systems are the perfect tool for probing exotic properties of matter, which would be hard or impossible to study otherwise. The idea to fabricate two-dimensional lattices of interacting nanomagnets disconnected [11] or connected [9] designed to capture the physics of frustrated systems opens a door for a wealth of studies on spin systems. The main advantage is having systems which can be probed in real space with imaging techniques, such as magnetic force microscopy, Lorentz transmission electron microscopy and plenty more. This advantage allows us to study the local configuration of each object (such as spin orientation or ordering of magnetic charges), and all global properties (spin-spin correlations, magnetic structure factors) can be calculated.

With improvements in EBL techniques, it is now possible to design arrays of small magnetic particles at will. If the nanomagnets are small enough, they are single domains and, therefore, can be counted as pseudo-Ising variables[18]. Anisotropy axis, which determines the orientation of such Ising variables, can be controlled by the right material composition (this is crucial in the case of stabilising out-of-plane magnetisations) or simply with the shape of the nanomagnet.

There are two main approaches how to fabricate artificial kagome spin lattice with interacting single domain nanostructures. It can be built up from nano-magnets with out-of-plane magnetisation as seen in Figure 3.5 a). Nanomagnets with out-of-plane magnetisation are placed at the apex of each triangle in the kagome lattice (blue background layout). In this schema, orange represents magnetisation up and brown down. The second possibility is to use nanomagnets with an elongated shape and in-plane magnetisation as it is shown Figure 3.5 b).

At first glance, it might seem like systems shown in Figure 3.5 can perfectly capture the physics of the short range models introduced in section 3.1.1. The following works proved that long range interactions play a significant role and are hard to suppress.

The first experimental work of Tanaka et al. [9] showed that artificial kagome arrays with in-plane magnetisation tend to follow the kagome ice-rule and therefore resemble the behaviour of short range model of kagome systems. In Figure 3.6 a) there is Tanaka's MFM image of permalloy lattice. A magnetic domain observation at each vertex site shows no ice-rule-breaking configuration presence. This system might seem like a good candidate for capturing the physics of the short range model, but since nanomagnets interact via long range dipolar interactions, it is not the case. Qi et al. demonstrated that the ice-like physics of such structures could not be described using short range Hamiltonian [61].

Another possibility is to fabricate lattice with nano-discs with out-of-plane magnetisation as Chioar et al. did [44]. In Figure 3.6 b) you can see the magnetic contrast of TbCo nano-discs that gives the local directions of magnetisation. Nevertheless, by analysis of correlation coefficients and magnetic charges correlation, Chioar et al. proved that this system, too, is affected by long range interactions.

[18] A small single domain nanomagnet will always have a curl of its magnetisation at the edges - this is a feature that is usually neglected. Thus, the nanomagnet's magnetisation can be considered an Ising spin-like variable.

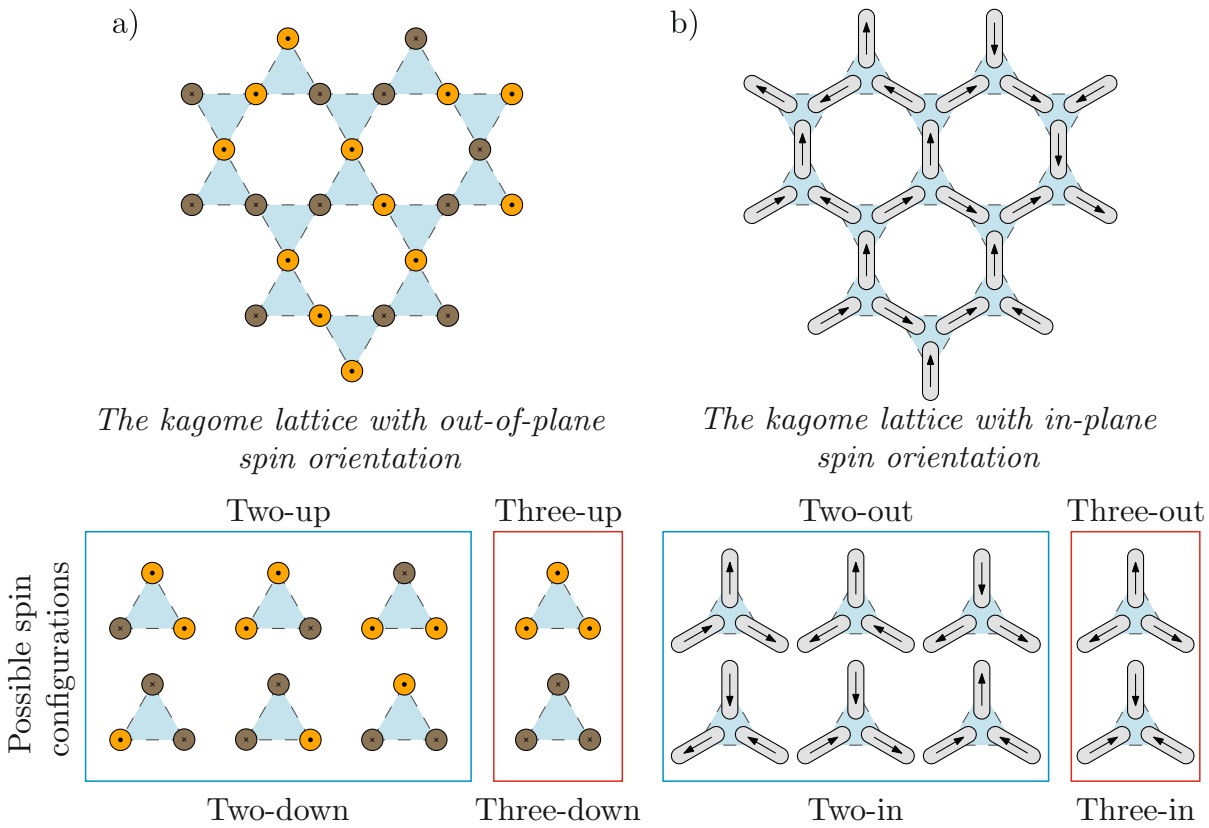

Figure 3.5: a) Nanomagnets with uniform out-of-plane magnetisation up (orange) or down (brown) placed on the apex of kagome lattice geometry. b) The kagome lattice made by nanomagnets with in-plane magnetisation. For both lattices, there are eight possible spin configurations of each of the vertices. These configurations can be divided into two groups: The first group follows the kagome ice-rules, and only two spins always point in the same direction (two-up/two-down or two-in/two-out of the vertex). In the second group, there are high-energy spin configurations where all spins point in the same direction (three-up/three-down or three-in/three-out of the vertex).

At this point, many works are building on Tanaka's founding and studying long range dipolar kagome spin ice. But there are promising attempts to design systems where the long range interactions and effect of father-neighbour couplings are minimized[19] in artificial kagome dipolar Ising antiferromagnet by using a mixture of out-of-plane and in-plane magnetisation regions [62] as can be seen in Figure 3.6 c) where areas with out-of-plane magnetisation (red ones) are connected to the areas with in-plane magnetisation (blue ones). White bar indites length of 500 nm in each of the images.

One of the challenges of studying artificial kagome dipolar systems is bringing them into their low-energy phases, mainly due to the effect of critical freezing at the SL1/SL2 border, where magnetic charge crystallisation occur.

In this work, we show how to bypass the intrinsic problem of freezing the dynamics simply and with our approach, we can access a priory dynamically inaccessible ordered ground state of kdsi and even fragmented spin liquid configurations.

[19] Minimised but not eliminated.

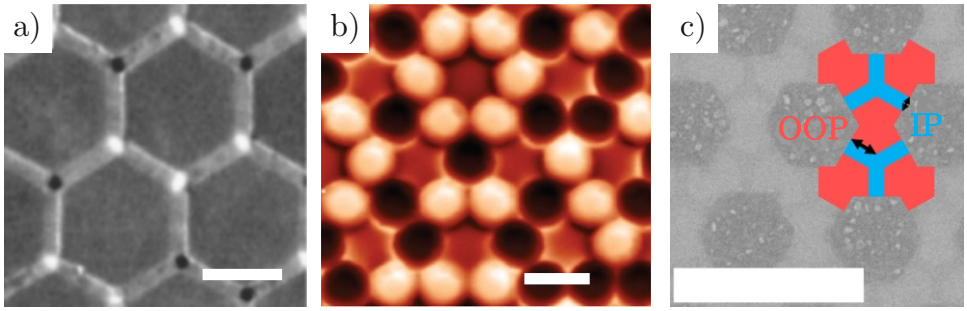

Figure 3.6: a) Pioneering work of Tanaka's showing MFM contrast of kagome dipolar spin ice permalloy lattice with in-plane magnetisation and kagome ice-rule obeying spin configurations taken from [9]. b) MFM image of the kagome dipolar Ising antiferromagnet Chioar's TbCo nanodiscs array with out-of-plane magnetisation taken from [44]. c) Artificial lattice combining the areas with out-of-plane magnetisation and in-plane magnetisation to reduce the effect of long range dipolar interaction within the system as proposed by Colbois et al. [62].

3.3. Phases of the kagome dipolar spin ice

The interest in the kagome dipolar spin ice system arises from the fact that this system has a very peculiar phase diagram. As mentioned in section 3.1.2 phases of kdsi are following: *Paramagnetic phase* (PM), *Spin liquid 1 phase* (SL1), *Spin liquid 2 phase* (SL2) and *Long range order phase* (LRO).

Thermodynamic evolution of entropy and specific heat of kagome dipolar spin ice system is shown in Figure 3.7 calculated using Monte Carlo simulation by Canals et al. [55]. Both of the quantities are plotted dependent on T/J_{NN}, where T is the temperature of the system and J_{NN} is the coupling strength constant between nearest neighbours. As the temperature decreases the systems evolve via crossover (orange line in Figure 3.7) from high-temperature paramagnet into SL1 and the system starts to correlate. Further decrease in the temperature force the system to undergo a phase transition from SL1 to a fragmented SL2 phase. During this transition, there is an immense loss of entropy (which will be discussed further in the text closely) and a spike in specific heat. If the system is cooled enough, the second phase transition occurs, and the system ends up in the ground state long range order configuration. Black dashed lines highlight both phase transition temperatures.

The best way to fully describe the difference between each phase is to look at the spin configurations, magnetic charge configurations and spin dynamic constraints. For that purpose, dedicated figures comparing the following properties for all phases are provided:

1. *Spin configuration* - whether the spins are ordered/disordered and correlated/uncorrelated. In Figure 3.8 you can see an example of: a) the spin configuration and b) the average spin configuration corresponding to each phase. An easy way to visualise spin ordering in real space is to show which simple loops (the smallest possible loops are made from six spins) have a closed flux of spins. A green dot will highlight these loops. However, this property is best visualised by calculating the correlation coefficients and magnetic structure factors, which give us information

about how the spins correlate. Both correlation coefficient and MSF temperature dependence are shown in Figure 3.9.

2. *Magnetic charge*. This property is visualised by red or blue coloured circles for positive or negative charges. Small circles represent ± 1 charges, corresponding to two-in/two-out spin configuration and large circles ± 3 corresponding to high-energy three-in/three-out configuration. Examples of possible charge configuration and average charge configuration for each phase are shown in Figure 3.8 a) and c), respectively.

3. *Spin dynamic constraints* - in each individual phase, different constraints of the spin dynamics arise from both charge and spin configuration energy minimisation requirements. These dynamic constraints are shown in Figure 3.10.

Each of these three aspects will be discussed individually for every phase in the following paragraphs.

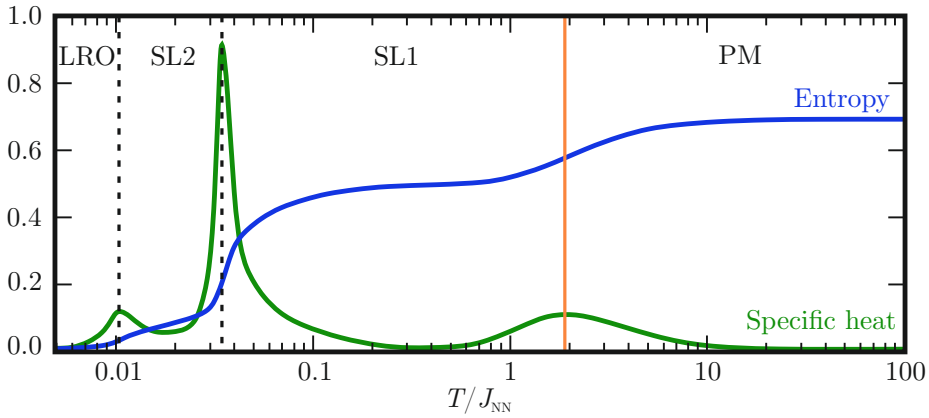

Figure 3.7: The simulated temperature dependencies of the entropy and specific heat of the kagome dipolar spin ice system. T/J_{NN} is the temperature of the system normalized to the nearest neighbour coupling strength. Crossover temperature between PM and SL1 phases is coloured orange, while phase transition temperature between SL1/SL2 and SL2/LRO phases are black dashed lines. Taken and edited from [55].

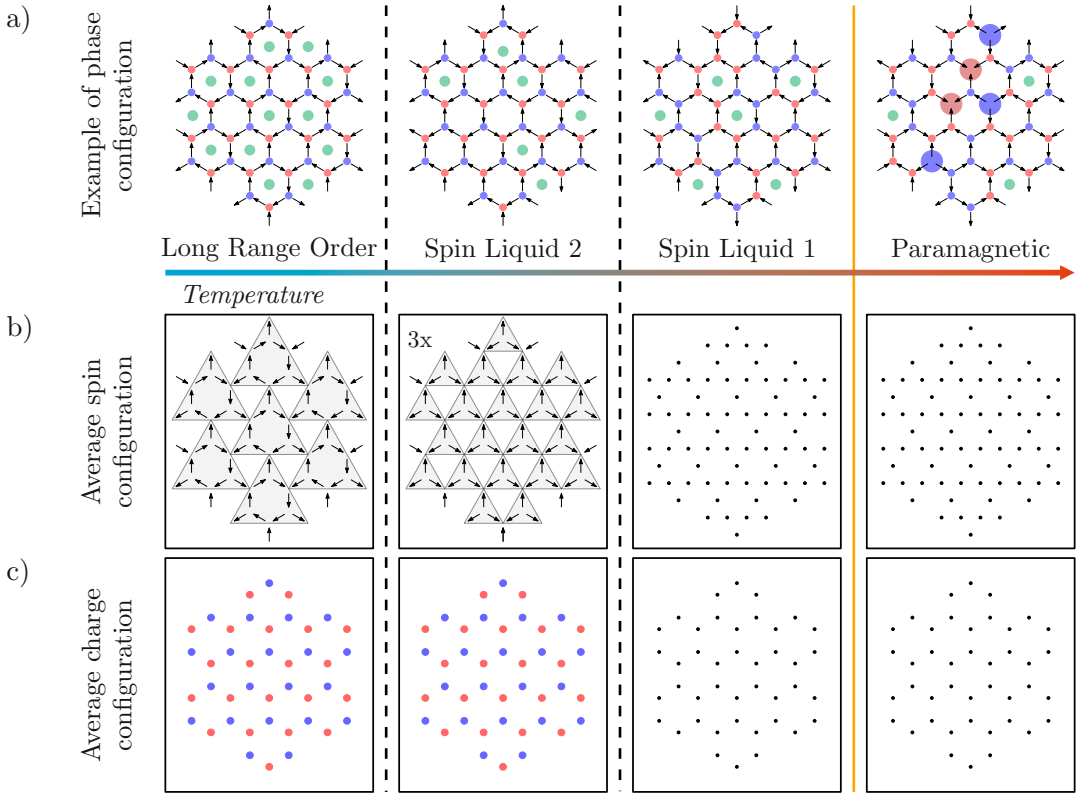

Figure 3.8: a) Examples of possible spin and magnetic charge configurations. Red and blue dots represent magnetic charge and the green dots represent hexagons with closed magnetic flux. b) Average spin configuration, where arrows represent the mean value of spin after averaging. The length is zero for the PM and SL1 phase, 1/3 for the SL2 phase and 1 in the LRO phase. The shaded triangles show the spin unit cell. c) Average magnetic charges, where the blue and red dots represent the mean value of the magnetic charge. While in PM and SL1, the value is zero on average, in SL2 and LRO, phase magnetic charge is ordered with alternating value ± 1. Taken and edited from [63].

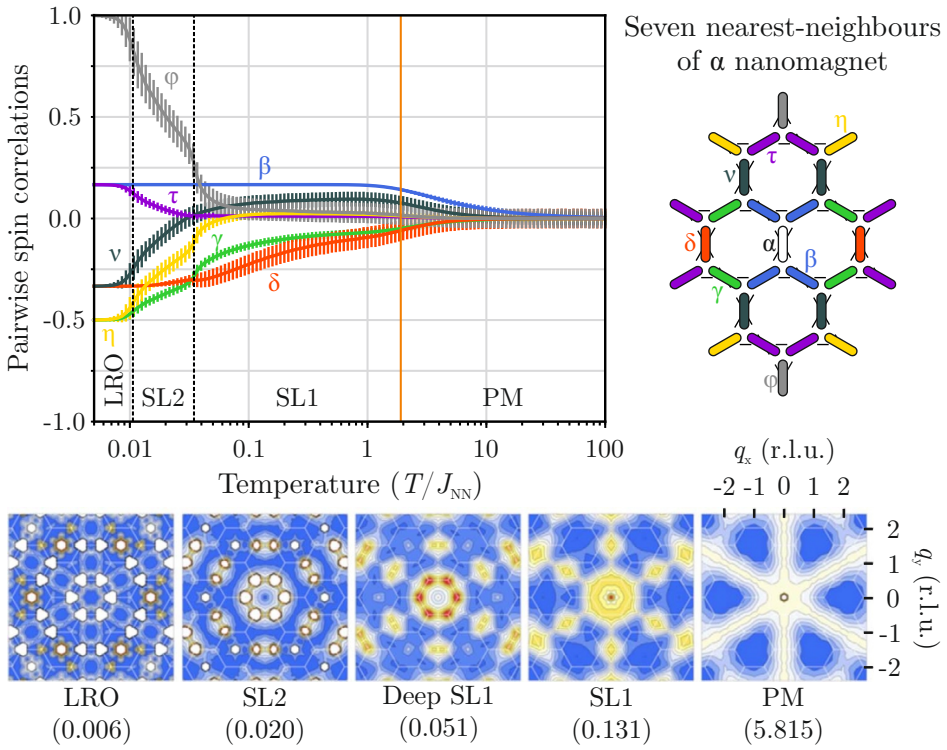

Figure 3.9: Monte Carlo simulations of temperature-dependent pairwise spin correlations of the first seven neighbours to α. The orange line indicates the crossover temperature between PM and SL1, and the black dashed lines mark the temperature of phase transitions between individual phases. In the bottom panel, MSF is calculated for different effective temperatures (shown in brackets below) belonging to each phase. MSF are taken and edited from [55]. MSF images show how system goes from disordered (indicated by diffused background) PM phase into perfectly ordered (indicated by intensive Bragg peaks) LRO phase.

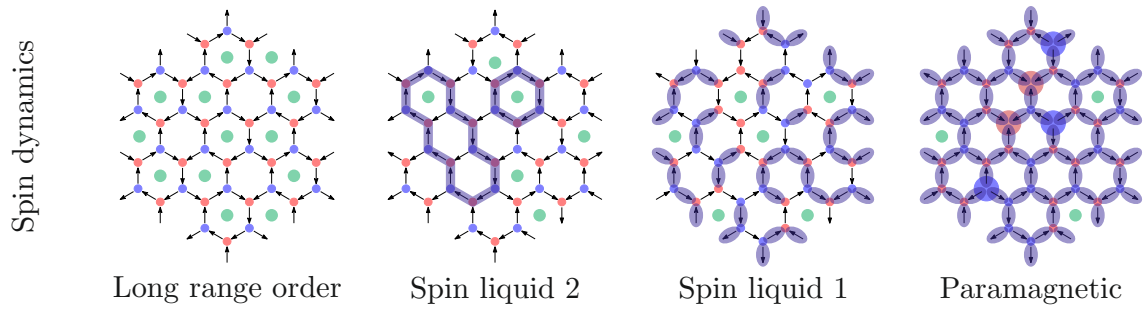

Figure 3.10: Schematics of the possible spin dynamics in all kdsi phases. Spins that are allowed to flip are highlighted in purple frames. In PM, all spins can flip freely since there are no charge or spin constraints. In SL1, only some spins can flip rest of the spins are frozen as flipping them would lead to the kagome ice-rule-breaking three-in or three-out spin configurations. In the SL2 phase, another constraint is present as magnetic charge crystallisation occurs; therefore, the spins can only flip if the whole loop containing the spin switches. If not, the charge ordering would be broken. In the LRO phase, everything is perfectly ordered, and no spins are allowed to flip.

Paramagnetic phase

PM phase is the highest energy phase of kdsi. An example of the spin configuration of the PM phase can be seen in Figure 3.8 a). In this phase, the temperature T of the system is much higher than the coupling constant between the nearest neighbour J_{NN}, hence $T/J_{\mathrm{NN}} \gg 1$. There are no constraints on spin dynamics, and all spins are allowed to change their orientation without any limitation[20]. In this phase, spins are uncorrelated, as is proven by Monte Carlo simulations in Figure 3.9 where all pair-wise correlations fluctuate around zero and MSF shows only diffused background. Even high-energy spin configurations are possible; hence vertices with magnetic charge +3 (large red circle) or -3 (large blue circle) can be observed. Due to the constant spin flips leading to random magnetic charge configurations, the average spin and magnetic charge configuration are zero, as is shown in Figure 3.8 b) and c).

Spin liquid 1 phase

As the temperature decrease to values $T/J_{\mathrm{NN}} \sim 1$, the system evolves into the SL1 phase. The spins start to correlate as Monte Carlo simulations show in 3.9, and in the MSF image, we can see how fingerprints of correlations start to emerge. Therefore this phase is disordered but correlated as one would expect from the spin liquid. There are no ± 3 magnetic charges since the effect of coupling strength of the nearest neighbours starts to have more power over the dynamic of the spin; therefore, in Figure 3.8 there are only ± 1 magnetic charges and no visible spin ordering. The spins still fluctuate but only if the resulting configuration follows the kagome ice-rule, and thus average spin and magnetic charge configuration is zero. As it can be seen from the evolution of correlation coefficients and MSF images (see changes in-between higher temperature MSF of SL1 and low temperature deep SL1 MSF), SL1 phase correlations coefficients are temperature dependent, which is the difference between this phase and low-energy phase of short range models described in sections 3.1.1.

Spin liquid 2 phase

Further temperature reduction causes longer range couplings to correlate, and the systems undergo the first phase transition into the SL2 phase. Even though most of the residual entropy is released, as is shown in Figure 3.7 SL2 phase is still macroscopically degenerated [59, 60]. In spin liquid 2 phase spins develop stronger pair-wise correlations. Moreover, a puzzling behaviour of the system appears. On the one hand, magnetic charge crystallisation occurs, and ± 1 charges periodically alternate across the system. This crystallisation indicates strong spin ordering, but on the other hand, spins are still highly fluctuating. It must be said that there is no magnetic charge degree of freedom encoded in the system's Hamiltonian as shown in Equation 3.20. Therefore magnetic crystallisation seems to emerge out of nowhere.

However, the spin fluctuation now must obey not only the kagome ice-rule but also magnetic charge constraint, meaning that spins are only allowed to flip in a way that will not disturb the charge ordering. Such flipping can be achieved only if spins fluctuate in

[20] Spins are still Ising variables, so they only fluctuate between two possible orientations.

collective loop spin flips, as shown in Figure 3.10. Spins are ordered and disordered at the same time. Therefore, diffused background in MSF coexists with rising Bragg peaks signal as is shown in Figure 3.9. This behaviour of spins is called *spin fragmentation* because each spin can be considered fragmented into a static and dynamic part of itself. Signatures of spin fragmentations have been detected experimentally [53, 64] and even observed in real space measurement on a fraction of the sample [55].

SL2 can be described as spin liquid (disordered but correlated spin system) sitting upon a magnetic charge crystal. Spin configuration can be considered to be a vector field and by applying Helmholtz-Hodge (HH) decomposition over the entire network [55, 65] each spin can be separated into curl-free (static) and divergence-free (dynamic) channels as is shown in Figure 3.11. Result configuration shows the possible spin (black arrows, having value 1) configuration of the SL2 phase. The magnetic charge is $+1$ in red triangles and -1 in blue ones. After applying HH decomposition, we can separate the configuration into two parts.

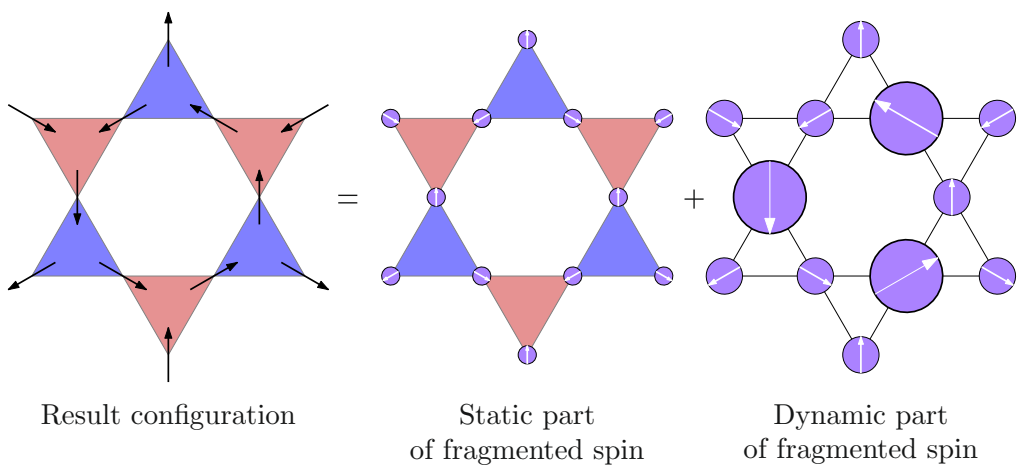

Figure 3.11: Visualisation of the spin fragmentation process. Any spin configuration belonging to the SL2 phase can be divided into two parts. Black arrows represent spins in the result configuration, and the associated magnetic charge is visualised by red (+1) and blue (-1) triangles. By applying Helmhotlz-Hodge decomposition on the spin network, each spin fragment into two channels. The static part of the spins forms a divergence-full field, where all spins have a value of 1/3, and by pointing all in or all out, the vertex forms the corresponding magnetic charge crystal. The dynamic part of the spin forms a divergent-free field and can constantly fluctuate. The spin value is either 2/3 and the same orientation as its static part or 4/3 with the opposite orientation to its static part, always adding up to 1. The resulting configuration has the same spin orientation as the dynamic part of the fragmented spin. However, it forms the same magnetic crystal as the divergence-full static part of the fragmented spin. Taken from [55].

First, let us focus on curl free static part. The fragmented spins in the smallest purple circles all have a value of 1/3[21] and are oriented all in (in the case of red triangles) or out (in the blue triangles) since there are always three spins contributing with $\pm 1/3$ the result is always ± 1 charge in vertex.

[21] In this case value is meant as a part of unit *spin*.

On the other hand, in the divergence-free dynamic part, we can see two types of spins. One type has a value 2/3 and the same orientation as its fragmented portion within the static section combining into a spin with a total value 1. The second type has a value of 4/3 and the opposite direction than its static counterpart.

HH decomposition can be done on any spin configuration belonging to the SL2 phase, always resulting in the same configuration of static curl-free configuration independent of the initial state. As a result of the spin fragmentation, if an average image of spin configuration is calculated as shown in Figure 3.8, one can see the static part of the fragmented spin forming unit cells. For a better visibility, the spins in images were enhanced 3x times. Also, the direct effect of spin fragmentation is that the average magnetic charge is perfectly ordered and alternating. However, there is no visible spin ordering in the spin configuration example.

The first partial capture of the SL2 phase in real space in a portion of the system was captured by Canals et al. [55].

Long range order phase

As the system temperature drops to the level of the second phase transition from SL2 into the LRO phase, almost all the residual entropy is released, and the system enters its two-times degenerated ground state.

In the LRO phase, the spins are perfectly ordered and therefore highly correlated, as shown in Figure 3.9. Example of the LRO phase in Figure 3.8 a) shows the perfect ordering of smallest possible loops (six spins) with closed magnetic flux as visualised by the green dots. Average spin configurations are perfectly ordered while maintaining the magnetic charge crystal, which results in intense Bragg peaks in the MSF image as shown in Figure 3.9.

The first ever real space image of the LRO phase was measured by Gartside et al. [66] with a clever trick. They fabricated six hexagons of magnetic nanostructures and saturated the magnetisation in one direction, as seen in Figure 3.12. Using a high-moment MFM tip, they then reversed the spin orientation of chosen islands (blue ones) to form perfect LRO ordering.

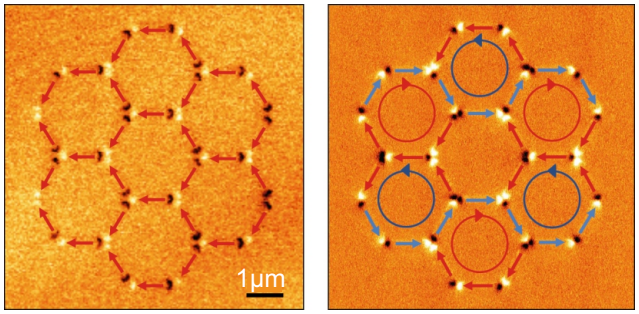

Saturated state | Long range order configuration

Figure 3.12: MFM image of LRO phase writing process as done by Gartside et al. Initially, the system consisting of six hexagons is saturated in one direction. Only by flipping 14 spins with the MFM tip rewriting mechanic described in [66] were they able to form the resulting LRO spin configuration. Taken and edited from [66].

3.4. Dynamical freezing

As mentioned, one of the main problems of probing low-energy phases of kdsi (or kdIa) systems is the critical slowing of spin-spin correlations as the system approaches the SL1/SL2 phase transition. There are two different contributions to the slow-down effect: critical slow down and single spin freezing.

Firstly, as with any phase transition, the system exhibit *critical slow down* near the phase transition. It takes the system more time to return to equilibrium, even after small perturbations or disturbances are made.

The second factor that causes the slow-down is freezing the single spin-flip dynamics. In Figure 3.13 result of the MFM measurement of the kagome lattice can be seen together with a spin and a magnetic charge configuration of zoomed section. The system was brought into this configuration via magnetic field demagnetisation. There are no three-in or there-out configurations, the magnetic charge is disordered, and the system is in the SL1 phase. If we look at the spin and magnetic charge configuration, we can see areas with a white and green background. These areas indicate patches of magnetic charge domains. The spins crossing the border of these patches are frozen; they cannot flip because it would introduce a three-in or a three-out defect within one of those patches. The inability of spin flips means that the domain walls are frozen and cannot evolve, and the system is frozen in this configuration. The patches of magnetic charges nucleate randomly all over the system and can only grow if the neighbour patch vanishes and is absorbed into the growing patch. For this annihilation of a large magnetic charge patch, first, one of the border frozen spins would need to flip - leading to a high-energy configuration. Only after that could the spins co-creating this three-in/three-out defect flip and bring the whole lattice into a lower-energy state, closer to the SL1/SL2 phase transition. The deeper in SL1 the system is, the less probable such transient high-energy excitations are.

The only possible single spin flips are those which annihilate the patch by itself. Examples of all such spins are highlighted in Figure 3.13 with black ellipses surrounding them.

Therefore the dynamical freezing is a consequence of significant energy barriers separating quasi-degenerate configuration, and the system cannot find a more energetically favourable state.

The freezing of dynamics is an intrinsic, model-dependent mechanism; thus, it is an ever-present slowing factor and must be bypassed with external effects to reach the low-energy phases. Dynamical freezing is not occurring only in the dipolar kagome ice but is affecting all systems where loop dynamics drive the low-energy manifolds.

Probing the low-energy manifolds is still challenging in the ice models [64] if possible. Therefore the LRO and SL2 phase in the artificial dipolar kagome ice have never[22] been observed and studied in real space.

[22]Only exception is research done by Gartside et al. [66]. Although they manually write the configuration spin by spin with MFM tip

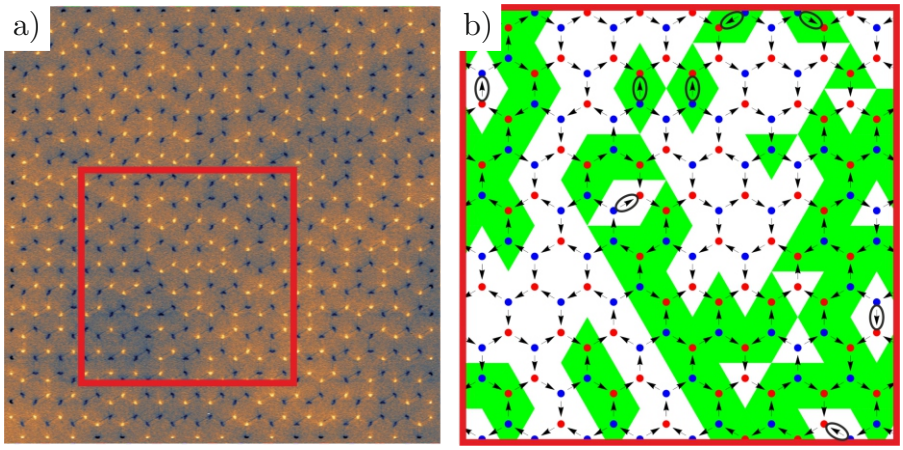

MFM image of SL1 phase

Spin configuration and magnetic charge of framed area

Figure 3.13: a) MFM image of permalloy lattice with connected nanoisland in SL1 phase with a red framed zoom section on a random part of the lattice. b) Spin configuration of zoomed area together with a corresponding magnetic charge. The white and green area indicates two opposite patches of magnetic crystal. Only highlighted spins are allowed to flip. All other spins are frozen. Taken and edited from [63].

3.5. Modified artificial kagome lattice with notches

In this work, we demonstrate, numerically and experimentally, one possible way to bypass dynamical freezing in artificial kagome ice. We are reproducibly and efficiently able to bring the system into any desired microstate satisfying the ice-rule. Specifically, we can force the system to form any spin and magnetic charge configuration of SL1, SL2 and LRO phases.

Artificial spin ice systems are typically build of small single domain nanomagnets, as shown in Figure 3.14 a), which are usually considered to be Ising pseudospins [67–70], and their micromagnetic texture is neglected. To the contrary, the strategy presented in this work relies heavily on micromagnetism as a key ingredient. Vertices in our systems are connected with a notch at each vertex, as shown in Figure 3.14 b). This notch locally lifts the system's degeneracy and prefers a specific spin configuration. With this, lattice can be built up vertex by vertex with desired spin configuration imprinted within its topology.

By tuning with geometrical parameters such as length or width of the nanomagnet and position, top angle or depth of the notch, we can tune the total energy of the micromagnetic texture at the vertex site.

The fabricated system differs from a conventional kagome lattice in a way that now it is not an assembly of interacting nanomagnets. Instead, the system can be viewed as a single object - magnetic grid where the main driving force is no longer two-body interaction between all pairs of spins in the system but the micromagnetic texture at the vertex site. Therefore, we consider this system not to be a spin model but a vertex model.

The illustration of the difference between these models is in Figure 3.14, where spins (represented by arrows) in a) can interact via dipolar interactions even with farther neighbours same as an array of interacting nanomagnets. However, in the vertex model in b), vertices represented by *the puzzle pieces* only affect their nearest neighbours via connections they share.

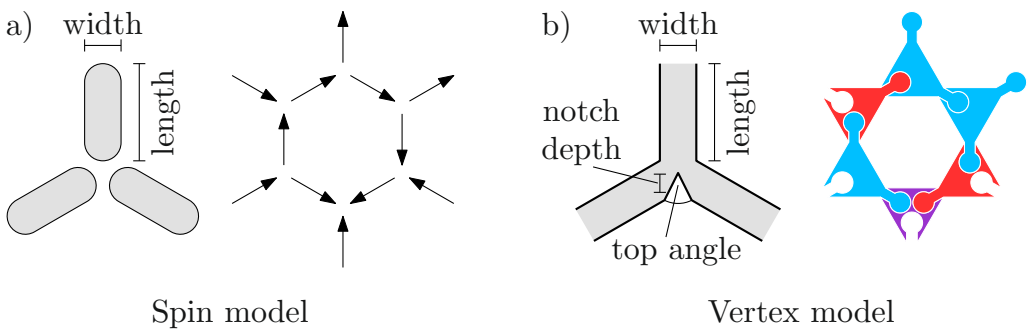

Figure 3.14: a) Schema of kagome vertex formed by separated single domain nanomagnets described by length and width. The behaviour of such a kagome lattice is described as pseudo-spins interacting via dipolar interaction. b) Schema of the kagome vertex with connected island and notch with all important geometrical parameters highlighted. The driving force of systems with connected nanomagnets are micromagnetic forces at the vertex site, and the nearest neighbours are only affected by the connection they share - similar to *puzzle pieces*. Systems with this behaviour can be described well by the vertex model.

3.5.1. Magnetostatic effect of the notch

Changing the geometry of the artificial kagome spin system by adding the notch will break the symmetry of the vertex and lift the system's degeneracy. The six spin configurations that follow the ice-rule now break into two groups. Two of them now have lower energy than the four rest, as is shown in Figure 3.15 a). The total energy of the magnetic domain wall at the vertex site is in case of permalloy vertices the sum of the *exchange* and *demganetisation* energies described in section 1.1.2. The energy E_1 of the vertex configurations in blue frames is lower than energy E_2 of the configurations in the red frames.

The notch size can be used as an external parameter to tune the total energy of E_1 and E_2 configurations. The energy dependence on the notch size and thickness of the structure is plotted in Figure 3.15 b). Grey, blue and purple data sets represent the energy of the E_1 configuration, and red, green and gold data sets are energies of E_2. When the depth of the notch is zero nm, the energy value for E_1 and E_2 is the same, but the energy splitting is visible as the notch goes deeper into the vertex.

The micromagnetic simulations were performed using Mumax3 code [22], with the following simulation parameters: The nanomagnets were 750 nm long, 250 nm wide and with three different thicknesses 5, 10, 25 nm. The depth of the notch varied between 0 and 300 nm with 50 nm step. The top angle of the notch is fixed to 30°. Since our experiment uses permalloy as magnetic material, the stiffness constant is set to 10 pJ/m, magnetocrystalline anisotropy is neglected, and spontaneous magnetisation is $8 \cdot 10^5$ A/m

to best mimic the behaviour of real structures. The damping coefficient is set to 0.5. To limit the influence of numerical roughness mesh size of the simulations has been reduced to $2 \times 2 \times t$, where t is the thickness of the structure.

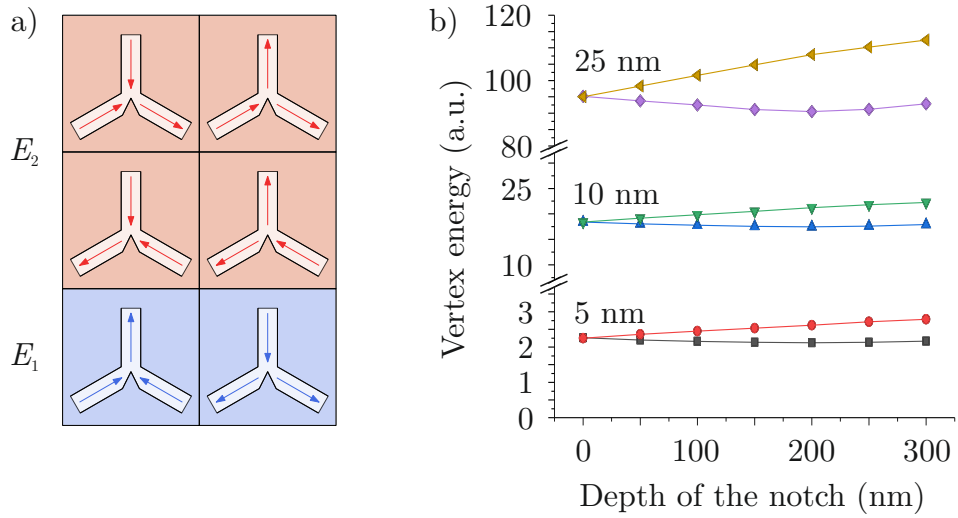

Figure 3.15: a) Six possible spin ice configurations in our modified lattice. Due to the presence of the notch, configurations in the blue frame have lower energy E_1 than energy E_2 of configurations in red frames. b) The vertex energy dependence on notch depth was simulated for three different thicknesses: $5, 10$ and $25\,\mathrm{nm}$. Grey, blue and purple are results for E_1 configurations, and red, green and gold data sets are energies of E_2. The energy gap between E_1 and E_2 always increases as the notch goes deeper into the vertex. Taken from [63].

For clarity, we define *the notch-rule* (a special case of ice-rule) that states that the vertices with notch prefer spin configurations with energy E_1. Large notches force the system to obey the notch-rule and to pick one of the two times degenerated configurations. However, if the notch is small, it slightly increases the probability of such a pick. With this knowledge, we can now build up vertex by vertex the whole lattice with the desired phase imprinted in its topography.

3.5.2. Imprinting the phases

To prove our concept, we fabricated several lattices with different phases of dipolar kagome ice imprinted into the topography. A series of kagome lattices with connected islands were made from permalloy material. The lattices were fabricated using EBL, and the resulting arrays consist of 250 nm wide and 1 μm long connected nanomagnets. The targeted thickness of the lattice was 15 nm. A notch was incorporated into every vertex site with a fixed 30 ° top angle. The depth of the notch was constant in each lattice but varied from 50 to 250 nm in between different sets of lattices. To have better statistics and eliminate the effect of the edges, each lattice contains approximately 10^3 nanomagnets.

All the lattices were demagnetised using a magnetic field protocol described in section 2.3 similar to the protocol used in [53, 56]. The length of the demagnetisation protocol will be mentioned with all the results. The measurement was done with the MFM technique.

Examples of how we use the notch position for imprint individual phases are shown in Figure 3.16, where there are SEM images of a) LRO and b) SL2 phases with the addition of the graphics on how the spins and resulting magnetic charge would be ordered in both cases. The same procedure can acquire lattices with any thinkable ice-rule obeying spin configuration.

Imprinting the LRO phase is easy since all the spins have to be perfectly ordered. To achieve such ordering, the notches must be periodically placed all over the lattice. The tricky part is to figure out how the notches need to be placed on acquiring one of the possible SL2 phases. We run Monte Carlo simulations to acquire a possible spin configuration of the SL2 phase. From the output of these simulations, we draw the layouts with a semi-automatic procedure where notches are placed at the vertices in a way that will lead to the configuration matching the Monte Carlo simulations.

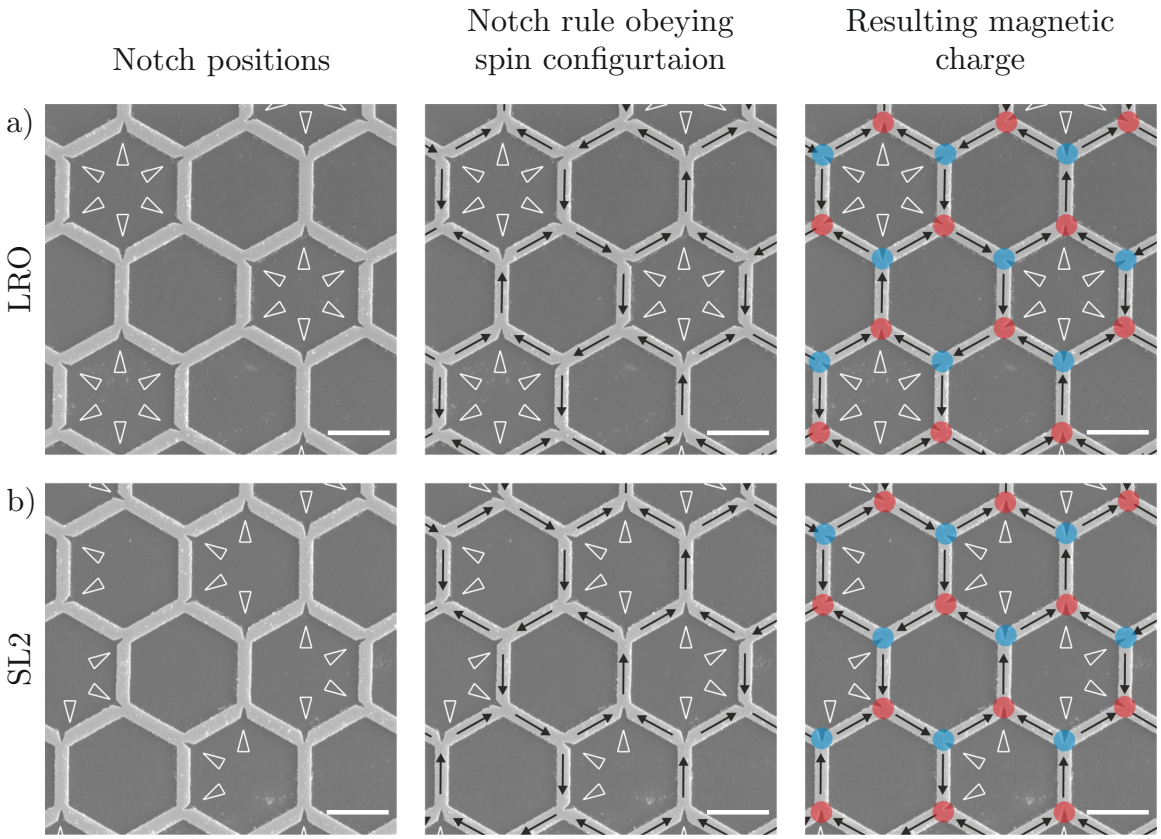

Figure 3.16: SEM images of two different lattices with notches. a) The LRO phase is imprinted into the lattice. Notch positions and orientations are periodic and white triangles highlight their position. Spins are perfectly ordered if they all obey the notch-rule, and the magnetic charge alternates from $+1$ to -1 all over the lattice. b) The SL2 phase is imprinted into the lattice, and positions of the notches are chosen, so the notch-rule spin configuration is one of the SL2 manifolds. The magnetic charge would also alternate in this lattice, but spins are not perfectly ordered. Black arrows indicate one of two possible ground state spin configurations of the lattices. White bars indicate the length of $1\,\mu$m.

Experimental results of lattices with imprinted phases are shown in Figure 3.17. For each of the LRO, SL2 and SL1 phases, AFM topography and MFM magnetic contrast is presented in top and middle panels, respectively. Individual spin orientation can be

acquired with a magnetic charge from MFM contrast, and both are plotted in the bottom panel. The topography of individual lattices and especially the positions of individual notches are hard to read. Therefore AFM images do not bring much information. For this reason, a further presentation of MFM measurement will not be accompanied by AFM topography but only with spin and magnetic charge configurations.

In Figure 3.17 a) lattice with LRO phase imprinted with the notch depth 200 nm shows almost perfect magnetic charge ordering in MFM image all across the lattice with a few exceptions at the edges. Domain wall dynamics cause these defects during demagnetisation, as mentioned in section 3.5.6. The length of the demagnetisation protocol used on this lattice was 7 days. In lattice b) with SL2 phase is imprinted with notch size 200 nm and the 3 days long demagnetisation protocol. LRO and SL2 have almost perfectly ordered magnetic charges, which means that the spins followed the notch-rule, but a more complex analysis will be done further in the text. SL1 phase shown in Figure 3.17 c) has no notches, and therefore all vertices follow the ice-rule instead of the notch-rule, which leads to a disordered phase of SL1.

The lattices with imprinted phases are brought to their ground state with field demagnetisation protocol, which is a strikingly different approach than the one introduced in [66]. The desired spin order is not restricted to only a few hexagons but is observed across the lattice. The dynamical freezing described in section 3.4 is therefore efficiently bypassed, and the previously inaccessible phases of the kdsi model are easily imaged. This approach can be used to acquire any ice-rule obeying microstate.

More importantly, magnetic disorder reapers if the notch size is reduced or when a shorter demagnetisation protocol is used. We were able to capture more disordered spin configurations resembling those of the SL1 phase, even on lattices with LRO ground state imprinted. With this knowledge, we present how the system's effective temperature can be tuned both with the notch size and with a shorter demagnetisation protocol. Supporting results are shown in Figure 3.18, where two lattices with LRO phase imprinted were exposed to the same demagnetisation protocol. The lattice in a) has 200 nm deep notch, and the lattice b) only 100 nm. The correlation coefficients and MSF were calculated for both lattices and are shown in Figure 3.18 c). The effective temperatures of both cases a) and b) are highlighted by black dashed lines and paired with their corresponding MSF. The MSF for lattice with a large notch shows perfect ordering with strong Bragg peaks, as is expected from the LRO phase. On the other hand, if a smaller notch is used, as in the case of b), the MSF shows a disorder associated with the SL1 phase. The effective temperatures of the systems are derived from comparing experimental and theoretical values of correlation coefficients expected in the kdsi model. The temperature is normalised to J_1 coupling strength between two nanomagnets not sharing the notch.

To demonstrate the effect of the demagnetisation protocol, Figure 3.19 shows the MFM contrast of two different lattices with the LRO phase imprinted. The depth of the notch is 200 nm, same as in Figure 3.18 a). However, the demagnetisation protocol was shorter than in case Figure 3.18 a). A larger disorder and LRO ground state crystallites are scattered across the lattices, leading to a higher effective temperature. The consistency of our method is also proved by the fact that the lattices with the same depth of the notch exposed to the same demagnetisation protocol ended up at the same effective temperature. Measurement in Figure 3.19 proves that the system is not trapped in its imprinted phase.

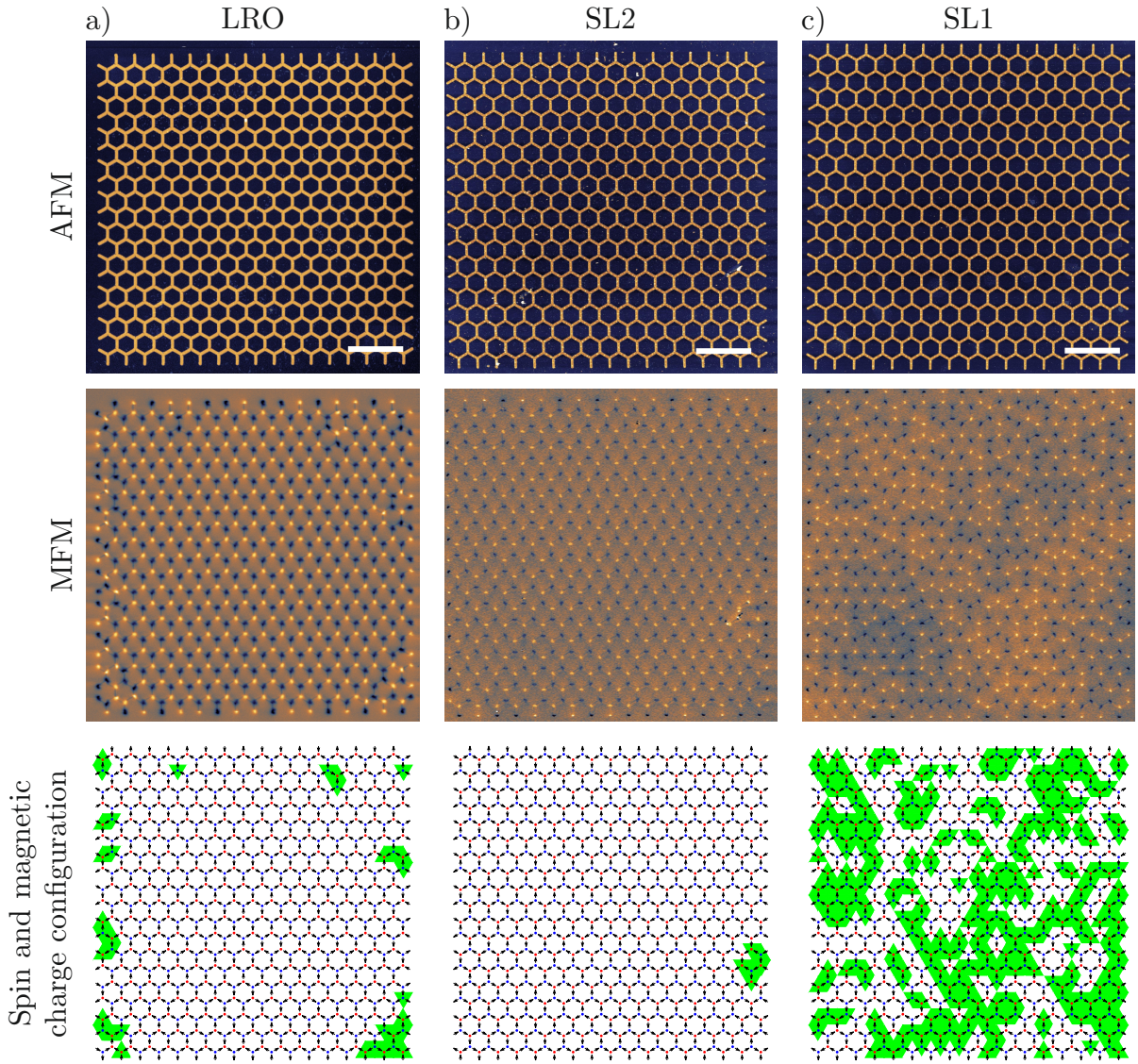

Figure 3.17: Examples of lattices with a) LRO, b) SL2, and c) SL1 phase imprinted. a) The MFM image shows almost perfect magnetic charge ordering in the LRO lattice. The reconstructed spin configuration shows perfect spin ordering following the notch-rule, with a few exceptions at the edge of the lattice. b) MFM image acquired by measuring SL2 phase shows perfect magnetic charge ordering and all spins except the three vertices in green patch perfectly follow the notch-rule. c) SL1 phase is exhibiting no charge ordering. Since no notch was used anywhere in the lattice, the ice-rule condition is obeyed. Spins are disordered, as well as magnetic charges.

MSF images show almost identical patterns of blurred Bragg peaks and slightly disordered backgrounds.

Similar results can be obtained with lattices where the SL2 phase was imprinted. As is shown in Figure 3.20 where the SL2 phase was imprinted with a) 200nm and b) 150nm notches. As expected, with large notches, the SL2 microstate is observed all over the lattice with an exemption of a small defect at the right edge. For a smaller notch size, the crystallites of SL2 states are separated by domain walls of notch-rule-breaking spin configurations. For both lattices, spin-spin correlations are compared to those predicted

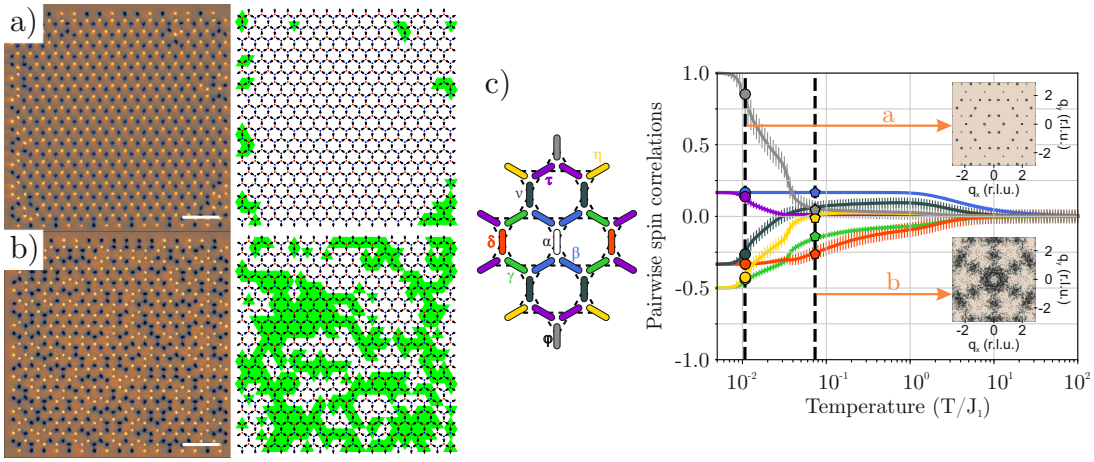

Figure 3.18: MFM images for lattices with imprinted LRO configuration with a) 200 nm and b) 100 nm depth of the notch. Comparison of experimental values of correlation coefficients (a) circles, b) pentagons) and correlation coefficients calculated for the kdsi model are shown in c) and accompanied with MSF for each system. The fraction of the notches breaking the notch-rule is a) 7 % b) 39 %. The white scale bar is 6 μm. Taken and edited from [63].

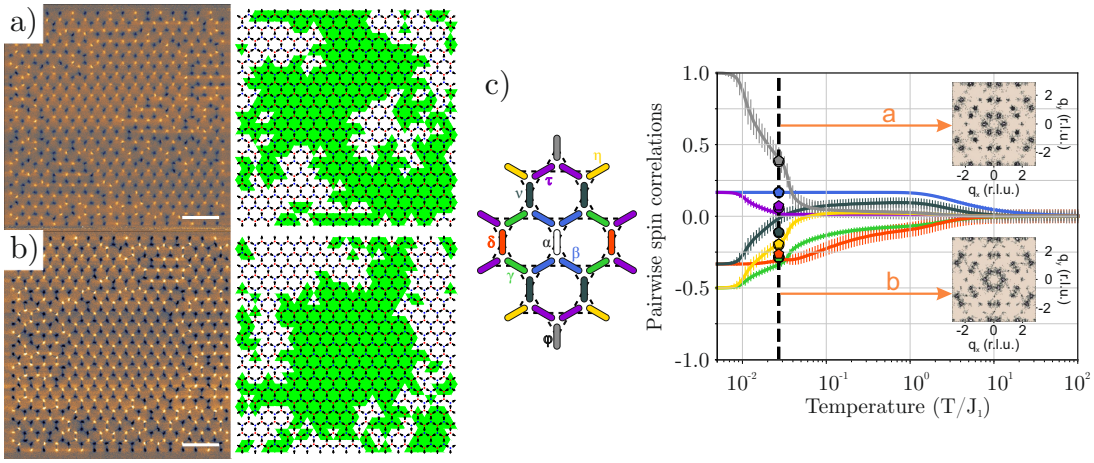

Figure 3.19: Magnetic images for lattices with imprinted LRO configuration with 200 nm depth of the notch for both lattices are shown in a) and b). Comparison of experimental values of correlation coefficients (a) circles, b) pentagons) and coefficients calculated for the kdsi model are shown in c) and accompanied with MSF for each system. The field demagnetisation protocol was shorter than the one used in Figure 3.18. The direct effect of the shorter demagnetisation protocol is bigger disorder, and the fraction of the notches breaking the notch-rule is a) 21 % b) 23 %. The white scale bar is 6 μm. Taken and edited from [63].

by the kdsi model. It can be seen that the notch size somewhat affects the effective temperature. The MSF was calculated for both lattices and is shown in Figure 3.20 c). For both lattices, we observe fingerprints of fragmentation process - disordered but structured background signal coexisting with emerging Bragg peaks.

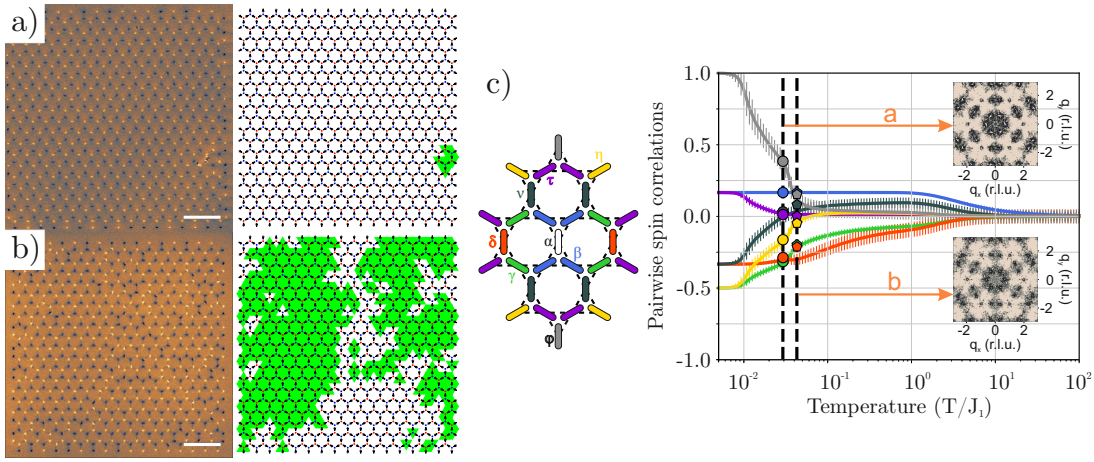

Figure 3.20: Magnetic images for lattices with imprinted SL2 configuration with a) 200 nm and b) 150 nm depth of the notch. Comparison of experimental values of correlation coefficients (a) circles, b) pentagons) with correlation coefficients calculated for the kdsi model is shown in c) and accompanied with MSF for each system. The field demagnetisation protocol was the same as in Figure 3.18. Both MSF reveals the fingerprints of the fragmented spin liquid phase. The fraction of the notches breaking the notch-rule is a) $< 1\,\%$ b) $17\,\%$. The white scale bar is $6\,\mu$m. Taken and edited from [63].

With the notch strategy, we managed to fabricate lattices that successfully bypassed the dynamical freezing. Our lattices were able to reach spin configurations representing both LRO in Figure 3.18 a) and SL2 in Figure 3.20 a) phases. Even though the ground state was imprint into the topology of the lattices during the fabrication process, the microstates are not frozen. The thermodynamics of our modified kagome lattices can be probed over a range of effective temperatures using smaller notch or shorter demagnetisation protocols. Therefore the notch can serve as a kind of heating knob since the notch's size determines the system's effective temperature.

3.5.3. Disadvantages of the notch presence

The ability to imprint any desired ice-rule-obeying configuration into our lattices comes with a price to pay. We are destroying the system's symmetry and changing the Hamiltonian using the notch defects. The effect of the changed Hamiltonian will be discussed in detail in section 3.5.5. As a consequence of bypassing the dynamical freezing with our notch approach, we do not need the loop dynamics, and single spin flip events can reach the imprinted ground states. However, without any loop dynamics, we cannot properly probe the physics of the SL2 phase - we can only probe one imprinted microstate.

Surprisingly even though we changed the Hamiltonian of the system by imprinting the desired microstate, we were able to heat the system and measure configurations that have the same spin correlations corresponding to the higher effective temperature of the kagome dipolar spin ice. There is one puzzling question yet to be answered. How is it possible to observe correlation coefficients which almost perfectly fit the thermodynamic profile of KDSI, even with the changed Hamiltonian?

3.5.4. Breaking of the notch-rule

In all our measurements, some vertices do not follow the notch-rule. In Figure 3.21 there are lattices with imprinted a) LRO with 200 nm depth of the notch and b) SL2 phase with 150 nm. All vertices breaking the notch-rule are at the boundaries of separating magnetic charge crystallites. The domain wall between these crystallites results from two patches of LRO or SL2 domains forming from a different area of the sample meeting. The energy penalty of having a notch-breaking configuration is proportional to gap $E_2 - E_1$. Therefore there are fewer notch-rule-breaking spin configurations within the lattices with a larger notch.

Analysing the lattices with notch-rule-breaking configuration shows that there are only two types of notch-rule braking vertices, one directly tied to the domain wall (the black ones) and the other trapped between two vertices violating the notch-rule (the orange one).

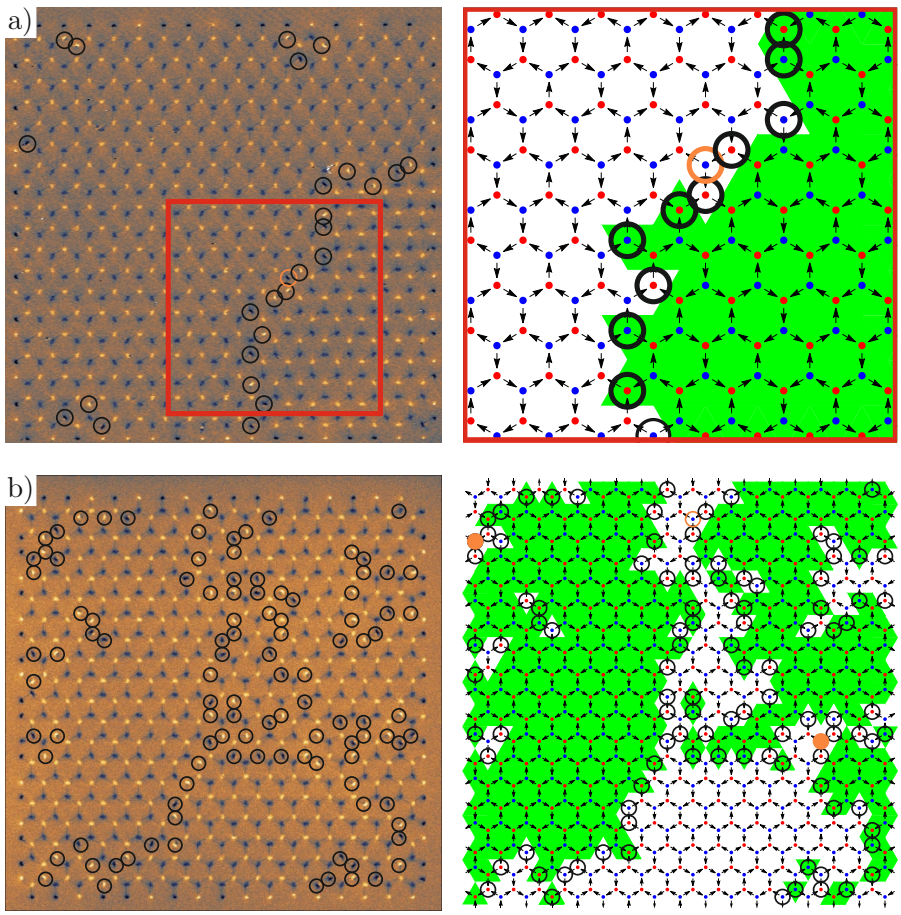

Figure 3.21: Magnetic image acquired by MFM technique of lattice with a) LRO and b) SL2 imprinted configuration and their associated spin and charge configurations. The circles indicate vertices with spin configurations breaking the notch-rule. All of them are confined to the domain wall separating different magnetic crystallites. Taken and edited from [63].

However, none of the 134 vertices violating the notch-rule in both images in Figure 3.21 is ever within the charge domain. They all result from the domain wall's existence and contribute to its energy.

3.5.5. Monte Carlo simulations and the Hamiltonian of kagome spin system with notches

Monte Carlo simulations shown in this section were calculated by Dr Nicolas Rougemaille and processed by the author.

Monte Carlo simulations were performed to answer the question about the effect of the presence of the notch on the physics of the dipolar kagome ice. Hamiltonian used in the MC simulations was the following:

$$H = -\sum_{\langle i,j \rangle} J_{ij} \sigma_i \cdot \sigma_j, \tag{3.21}$$

where σ_i and σ_j are Ising variables on sites i and j, respectively, the summation is done on the nearest neighbours. The further neighbours are neglected since we assume that the notches fully drive magnetostatics and magnetodynamics. Therefore the spin configuration is not affected by further neighbours.

The notch's presence breaks the vertex's symmetry; therefore, two coupling strength constant needs to be considered. J_1 constant will be considered for the neighbours not sharing the notch (two pairs in vertex), and J_2 is the coupling strength of nanomagnets sharing the notch. In all following simulations, J_1 is set to 1, and the thermodynamic behaviour of the system is probed for different values of J_2. The simulations were done with lattices where notches are periodically organized, so the imprinted ground state of the simulated lattices is LRO.

The following description of Monte Carlo simulations done by Dr Rougemaille is directly taken from [63] supplementary material:

"The Monte Carlo simulations were performed on $18 \times 18 \times 3$ kagome lattice sites with periodic boundary conditions. A single spin flip algorithm is used. The system is cooled from $T/J_1 = 100$ to the lowest possible temperature. 10^4 modified Monte Carlo steps (mmcs) are used for thermalization, where one mmcs corresponds to a set of local updates sufficiently long to achieve stochastic decorrelation. 10^4 mmcs measurements then follow the thermalisation. The magnetic structure factor is composed of an 81×81 matrix covering a $\pm 3\pi$ area in reciprocal space. The specific heat, the entropy and the magnetic structure factors were calculated as a function of the normalized temperature T/J_1."

The discussion will be done on three possible cases for relations between J_1 and J_2 since all three possible cases are related to our experiment.

Suppose the J_2 constant is much larger than J_1 (situation corresponding to the system with large notches). In that case, Monte Carlo simulations show the system undergoing a phase transition from a high-temperature paramagnet to the imprinted LRO microstate as is shown in Figure 3.22, where $J_2 = 5$. These simulation results are in accordance with the observed behaviour of lattices with large notches (200 nm).

Suppose the coupling constants are equal $J_2 = J_1 = 1$. In that case, the system recovers its sixfold degeneracy (this is a case for the lattices without the notches). Hamiltonian in Equation 3.21 is equivalent to Hamiltonian described in Equation 3.18 and the thermodynamic properties of the kagome Ising antiferromagnet (or kagome spin ice) described

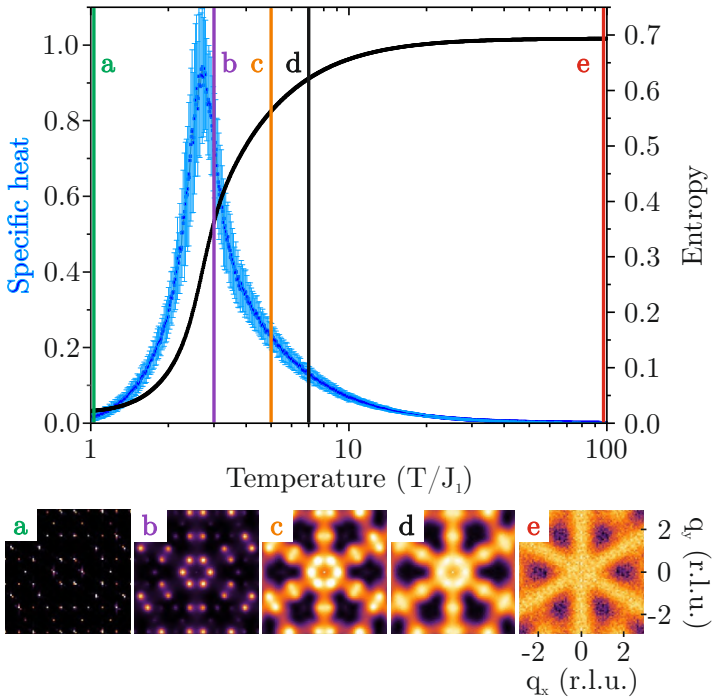

Figure 3.22: Monte Carlo simulations of entropy and specific heat evolution dependence on the system's temperature with the LRO phase imprinted. Coupling constants were set to $J_2 = 5$ and $J_1 = 1$. MSF images are calculated for effective temperatures highlighted by coloured lines. Taken and edited from [63].

in section 3.1.1 are observed. The high-energy paramagnet is separated by crossover from the spin liquid phase, as shown in Figure 3.23.

The interesting results were yielded by simulations where $J_2 \gtrsim J_1$, for instance in Figure 3.24 where coupling constant were set to $J_2 = 1.05$ and $J_1 = 1$. The thermodynamic profile of the system with these parameters is described by a high-temperature paramagnet separated by crossover from a spin liquid and followed by phase transition into imprinted ground state phase, which in this case was LRO. The entropy per site shows a plateau around 0.501 value (in spin liquid phase between crossover and phase transition) as expected from short range kagome ice [55]. Such a system can be fabricated by using smaller notches.

Coexistence of Bragg peaks together with diffused background signal in Figure 3.24 b) around effective temperature $T/J_1 = 0.05$ can be observed. However, rather than a fragmented SL2 phase, such MSF is caused by the formation of LRO crystallites surrounded by SL1-like as the phase transition effective temperature is approached. Comparison between the thermodynamic profile of kdsi and our modified lattices with $J_2 \gtrsim J_1$ shows the absence of SL2 manifold and the low-temperature ordering is a one-step process. This is due to the absence of long range dipolar interactions in the short range spin Hamiltonian considered in these Monte Carlo simulations.

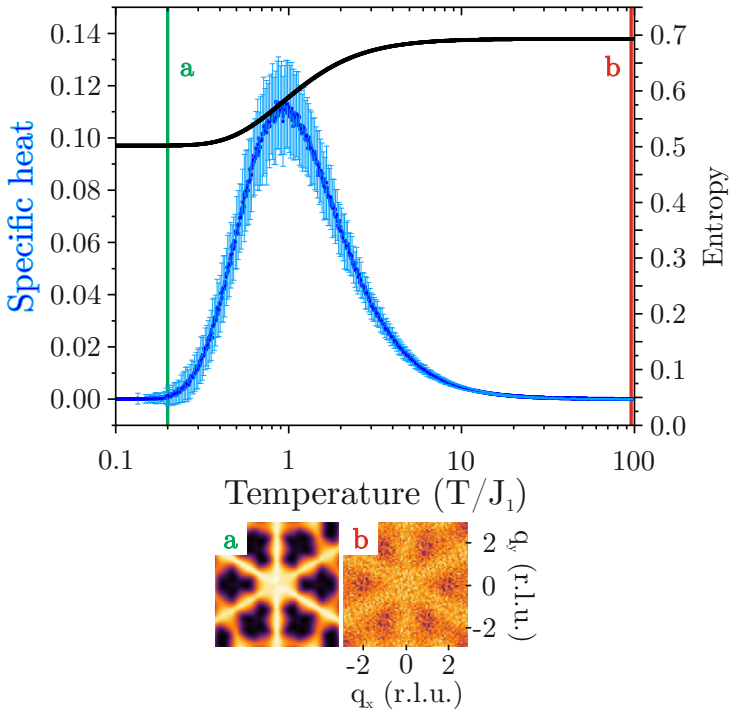

Figure 3.23: Monte Carlo simulations of entropy and specific heat evolution dependence on the system's temperature with the LRO phase imprinted. Coupling constants were set to $J_2 = J_1 = 1$. MSF images are calculated for effective temperatures highlighted by coloured lines. Taken and edited from [63].

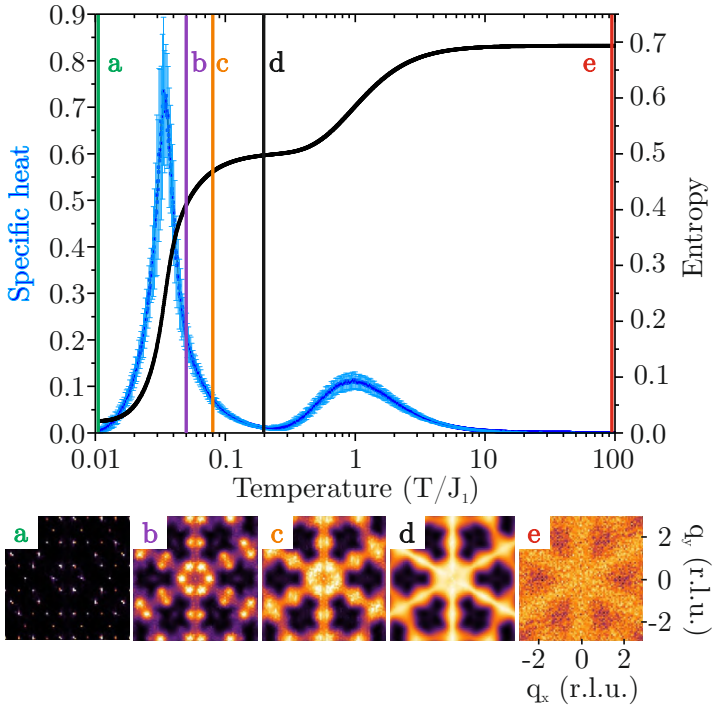

Figure 3.24: Monte Carlo simulations of entropy and specific heat evolution dependence on the system's temperature with the LRO phase imprinted. Coupling constants were set to $J_2 = 1.05$ and $J_1 = 1$. MSF images are calculated for effective temperatures highlighted by coloured lines. Taken and edited from [63].

3.5.6. Notch-driven domain wall propagation

Since we are using magnetic field-driven demagnetisation on lattices with connected nanomagnets. It is crucial to understand how the notches affect the domain wall (DW) propagation. Using Mumax3 code, we simulated the behaviour of our modified lattices during the simplest possible demagnetisation process. The simulations are used to acquire qualitative information about the effect of the notch. Simulated nanomagnets are 150 nm wide, 750 nm long and 20 nm thick. The mesh size of the simulations is always smaller or equal to $6 \times 6 \times t$, where t is the structure's thickness. All notches in simulations have the following parameters: the notch depth is 120 nm, and the top angle is 60 °. These geometrical parameters are slightly different from the one used in the experiment. However, the larger notch gives us a better understanding of its effect on DW propagation.

Starting with one vertex, we simulated how would notch position affect the domain wall propagation. The initial state of the simulations is shown in Figure 3.25 a), b), and c), where the vertices were all saturated along the axes of nanomagnets pointing upwards and relaxed, so the local energy minimum was reached. This saturated state obeys the ice-rule since two nanomagnets point inside the vertex and one outside. The next step was to apply a magnetic field in orientation of blue arrow shown in d), e) and f) and observe how the DW propagated from the top of the vertex. The results for notch position a), b) and c) are shown in Figure 3.25 d), e) and f) respectively. The yellow arrows mark the path of the DW across the vertex.

The results in e) and f) clearly show how the notch pushes the DW in the direction the notch is pointing. A more complicated situation is with result d). If the notch is pointing as shown in figures a) and d), there are, in fact, three possible outcomes, and it all depends on the shape of the travelling domain wall. It can flip one of the two nanomagnets or both of them, as is shown in Figure 3.25 d).

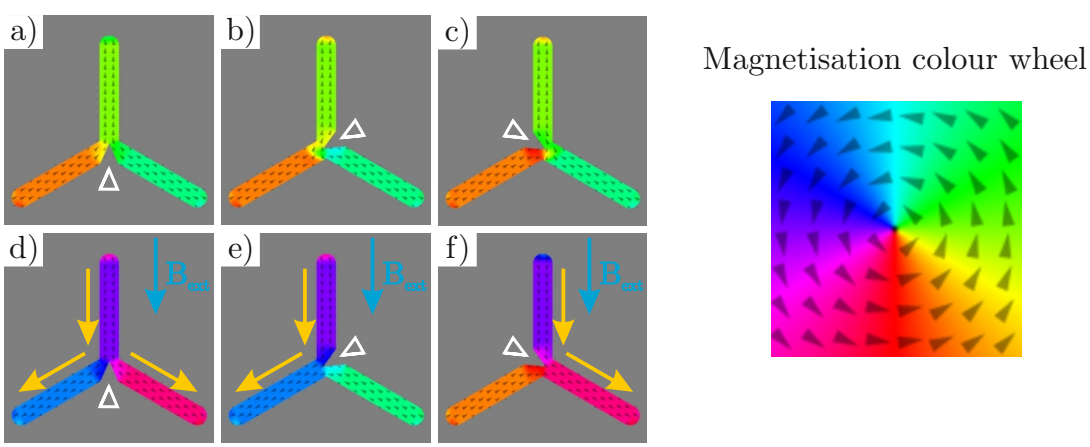

Figure 3.25: Mumax3 simulation of the domain wall propagation in one vertex with three different notch positions. Subgraphs a), b), and c) show the initial magnetisation configuration before the simulation starts. The magnetisation points up along the axes of the individual island. Outcomes of simulations after an external magnetic field (with direction of blue arrow) is applied are shown in subgraphs (d), (e) and (f). Yellow arrows indicate the way of propagation of the domain wall.

DW behaviour at the vertex with a notch pointing toward the propagating DW is similar to DW propagation in the vertices without the notch studied by Zeissler [71] and Sanz-

Hernández [72]. Both works studied the stochasticity of DW propagation in kagome-like systems and the effect of external parameters such as field direction on DW propagation.

Furthermore, we have simulated DW propagation in more complex systems to find out how the DW travel in lattices with notches and how individual DW interact with each other. In Figure 3.26, there is a medium-sized lattice with notches that are placed periodically. If all vertices obey the notch-rule, the resulting spin configuration would be the LRO phase. Similar to the previous simulation analysis, the lattice is first saturated and relaxed in the upward direction. In all cases shown in Figure 3.26, nanomagnets at the edges have frozen micromagnetic texture at their end, except for the ones marked with the white circle. This constraint is non-physical but allows us to analyse the propagation of DW from individual starting points.

After application of the external field (indicated by the blue arrow) in Figure 3.26 a) we can observe how the DW propagate from its starting point marked by a white circle to the vertex with the notch that splits the domain and the DW propagates trough both nanomagnets, but not further than into next vertices. As the DW arrives at the next vertices-sites, the configuration is stable because it is the notch-rule-obeying configuration. Moreover, the pinning field of this configuration is larger than the one used to drive the propagation further into the system. In cases b) and c), we can observe the "zig-zag" propagation of DW govern by the notches from starting points to the end of the lattice.

Important information is obtained from simulation in Figure 3.26 d) where all three DW were allowed to propagate trough-out the system. The most important part is highlighted with a black circle. It is a vertex where DW from a) and b) connect. The result of such a connection is a notch-rule-breaking spin configuration. It is the simplest possible mechanism for how defects in a spin configuration are made by DW propagation, even though notches govern all DW paths.

In the last set of simulations, the larger array of connected nanomagnets with periodically placed notches all over the system was saturated in upward orientation, as is shown in Figure 3.27 a). No part of the lattice was frozen, so the DW propagation could start from any given place at the lattice. An external magnetic field with the direction indicated by the blue arrow was applied until all DW propagation was ended. Yellow lines mark all the paths of DW propagations. Resulting configuration is shown in Figure 3.27 b) accompanied with related MFM contrast in Figure 3.27 c). In MFM contrast, we can see a large patch of "well demagnetised" vertices and three different highlighted types (red, blue and green) notch-rule-breaking configurations.

The formation of the redly highlighted defects is easy to explain. The two DW following the notch-rules collide exactly as observed in Figure 3.26 d). The blue defects are caused by DW, which should have propagated but stopped at the vertex site instead. The blue defects with the grey centre result from DW never arriving at their positions. The opposite problem happened in vertices highlighted with green circles. The notch should push the DW in a specific direction. However, the DW also goes around the notch and flips both connected nanomagnets. The green circles with grey highlights mark defects directly caused by correct propagation of extra DW originated in green vertices.

Even by the simplest possible demagnetisation protocol consisting of saturating the lattice and then applying a magnetic field in the reversed direction, we were able to bring simulated lattices into configurations following the notch-rule. The presence of the de-

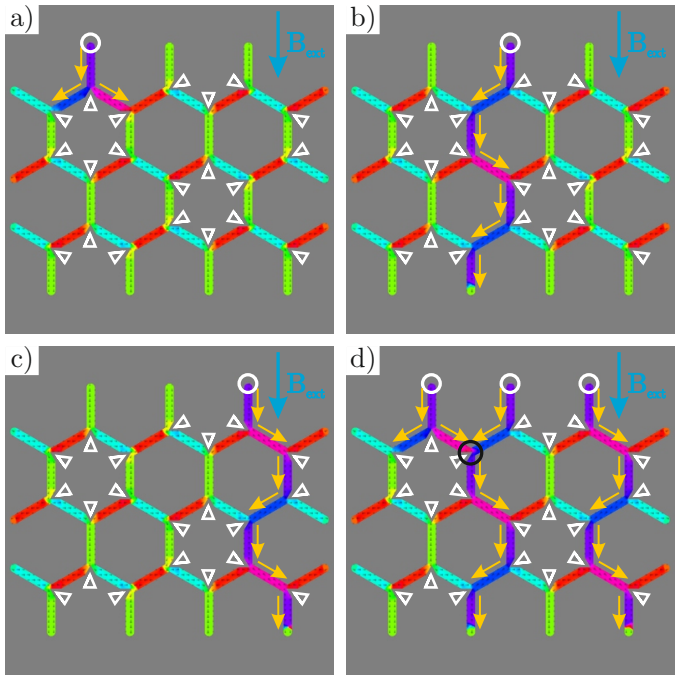

Figure 3.26: The outcome of the simulation of domain wall propagation. White circles indicate areas where the domain wall was induced before the simulation started. Yellow arrows indicate the path of domain wall propagation after applying the external field with amplitude 41 mT in the direction shown by the blue arrow. In subgraph a), we can see that the domain wall propagated only in the first vertex, and the presence of the notches blocked both paths. In subparagraphs b) and c), The domain walls propagated similarly from two different starting points. We can see the "zig-zag" propagation as the direction of the notches fully controls the domain wall dynamic. The black circle highlights the only notch-rule-breaking vertex caused by the interaction of the two DW.

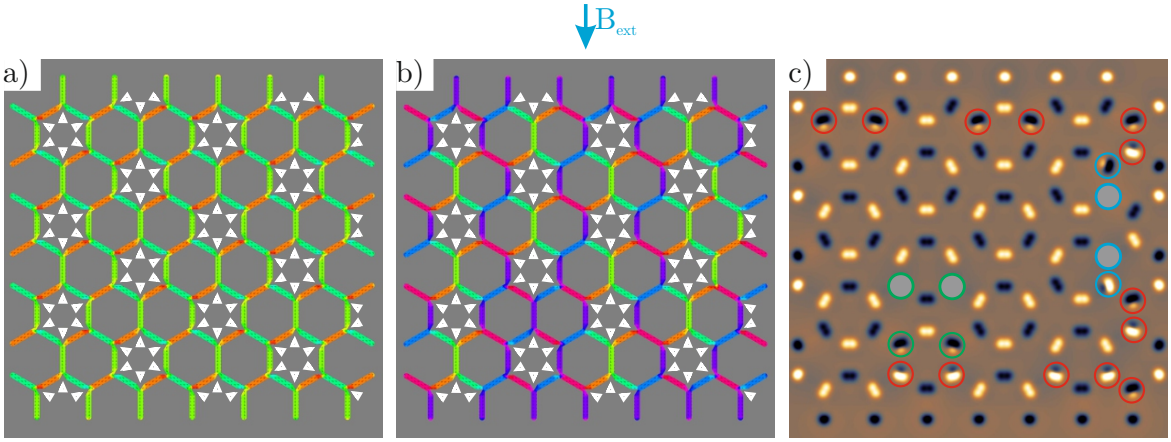

Figure 3.27: a) Large lattice with periodically placed notches highlighted by white triangles is saturated in the upward direction. b) The output of micromagnetic simulations where the magnetic field was applied to the lattice with amplitude 41 mT in the direction shown by the blue arrow. c) Corresponding simulated MFM image to the micromagnetic configuration in b). All notch-breaking configurations are highlighted in coloured circles.

fects can be explained by the fact that the system is not forced to follow the notch-rule, and the notches only increase the probability of the direction of the DW propagation.

Therefore on some occasions, the DW can propagate around the notch or get stopped by the notch pinning field. However, suppose the procedure is repeated with decaying amplitude of the applied magnetic field, ideally from all the directions, as it is done with our demagnetisation protocols. In that case, the system can eliminate the defects and force the vertices to follow the notch-rule if the notches are large enough.

Some promising works incorporate magnetically frustrated systems into the logic gate computations. There are attempts to build logic gates with the kagome-like geometry with connected nanomagnets and domain wall propagation [73] or disconnected thermally active square ice systems [74].

We believe that our notch approach can be used for building some basic magnetic logic gates. The concept is simple, and it is shown in Figure 3.28, where two logic gates, "OR" and "AND", are shown. The A and B nanomagnets are inputs, and the C is the output. The OR gate consists of three kagome vertices with two notches (highlighted by white triangles), starting with a saturated configuration where all nanomagnets have their magnetic texture pointing along their axis in the upward direction. DW propagating from starting point A always arrives at the output point C as shown in Figure 3.28 a), the same is true for DW propagating from starting point B as shown in b). Of course, if DW starts propagating from both A and B, it always arrives at output C.

"AND" logic gate is less trivial. The DW should arrive at output C only if DW arrive both from the A and B starting point. Two smaller notches in the middle vertex ensure this effect, which can pin DW propagating from a) A or b) B starting point. However, suppose both DW arrives at the middle vertex. In that case, the high-energy three-in spin configuration is present at the vertex site resulting in unstable out-of-plane magnetisation. This high-energy configuration collapses and minimises the vertex's energy by flipping magnetisation in output nanomagnet C, hence serving as an "AND" logic gate.

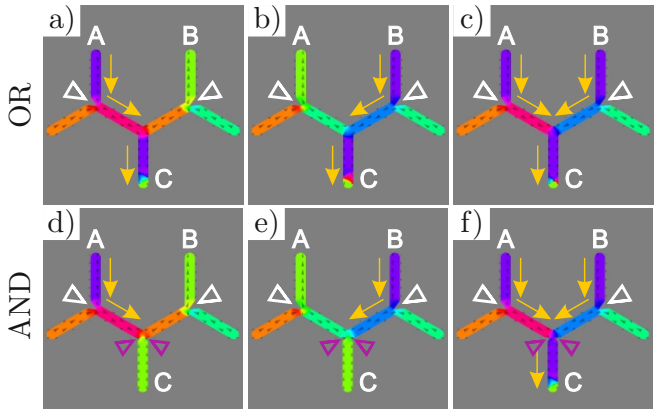

Figure 3.28: Subfigures a), b), and c) show the proposed logic gate "OR". Only two notches are placed at the position marked by the white triangles. When a single domain wall propagates through the system, notches lead it towards the centre vertex, and the magnetic field pushes the DW into the output nanomagnet C, regardless of the origin position of the DW. Subfigures e), d), and f) show the "AND" gate. If the DW propagate only from one starting point, as is shown in d) and e), the large notches highlighted by white triangles push the DW into the central vertex. The two small notches pin the DW, which cannot propagate further. Suppose both DW arrive at the central vertex. In that case, small notches cannot stop the flipping of the output nanomagnet C.

3.6. Discussion and concluding remarks

Even though the artificial kagome spin systems have been studied for almost two decades, many physical phenomena they could help uncover are still eluding. One of the reasons why it is hard to probe the physics of short range artificial kagome systems is the impossibility of elimination of long range dipolar interactions which arise from the way the systems are fabricated. On the other hand, in the long range dipolar artificial kagome systems, where the dipolar interactions are crucial, accessing the low-energy phases is prevented by the dynamical freezing described in section 3.4.

We believe that the solution presented in this chapter and published in [63] can solve both problems. Firstly, by transferring the problem from spin model[23] into the vertex model[24], we sufficiently eliminated the long range dipolar interactions because the physics is governed by the notch's tendency to minimize the energy of the domain wall at the vertex site. Note that the main difference between Tanaka's research [9] and the one presented here is that we are deliberately tuning the local energy of each configuration at the vertex site all over the lattice.

Secondly, with the approach of building the systems vertex by vertex to achieve lattice where any ice-rule-obeying state can be imprinted, we offer a solution on how to bypass the dynamical freezing and access previously inaccessible spin and magnetic charge configurations of artificial kagome dipolar spin ice. We provided experimental results of how efficiently lattice can be self-assembled using athermal field demagnetisation when the right parameters of imprint (e.i. depth of the notch) are used. Moreover, for the first time, we were able to measure spin configurations belonging to LRO and SL2 phases on a large scale in real space using artificial spin systems.

With Monte Carlo simulations, we presented thermodynamic profiles of our modified kagome lattice with imprinted phases. The LRO phase was chosen as the ground state of the simulated lattices.

Using the athermal systems that need to be brought to the ground state by field-driven demagnetisation is not the only way to reach low-energy phases via breaking the system's symmetry and locally imprinting the configuration, as Hofhuis [35] has shown. Utilizing a similar strategy, they designed thermally active lattices of interacting nanomagnets that were bridged by magnetic connections of two types (introducing two different J coupling constants between nearest neighbours), serving a similar effect as the notch.

The strategy of breaking the system's symmetry was also utilized on entirely disconnected interacting nanomagnets, where Yue et al. [75] break the system's symmetry by having nanomagnets of different sizes.

We are pleased to see that other research groups also use a strategy similar to what we presented of bypassing dynamical freezing. Now that the spin configurations of low-energy phases that holds the key to understanding phenomena like spin fragmentation

[23]The sets of nanomagnets interacting via long range interactions beyond the nearest neighbours drive the physics of the system.

[24]The local configurations of the spins depend only on the position of the notches, and neighbouring vertices affect each other only via a connection they share.

are accessible, research can be done on studying the behaviour of excitation of such configurations, or the interactions between the phase interface end so on.

Chapter 4: Artificial square system with holes

The square geometry is a result of the edge projection of 3D pyrochlore crystal into 2D plane as described in Chapter 1 and shown in Figure 4.1 a) where spins with in-plane orientation are placed onto the square projection (blue lattice). Although it is possible to have a square model with out-of-plane magnetisation [76], for the simplicity of the explanation, this realisation can be omitted since the physics of our experiment is linked only to the models with in-plane magnetisation.

However, the edge projection destroys the symmetry of the system, unlike the vertex projection (resulting in kagome geometry), by making a distance shift in between the spins creating vertex as is shown in Figure 4.1 b). There are now two types of pairs of spins in the vertex. The nearest neighbours are the spins which are perpendicular to each other, and they have coupling strength constant J_1. The second nearest neighbours are parallel, and their coupling constant is J_2. The symmetry breaking is causing a deviation from the water ice and spin ice systems. Therefore, it poses a challenge that must be solved to regain the proper degeneracy expected from the spin ice systems.

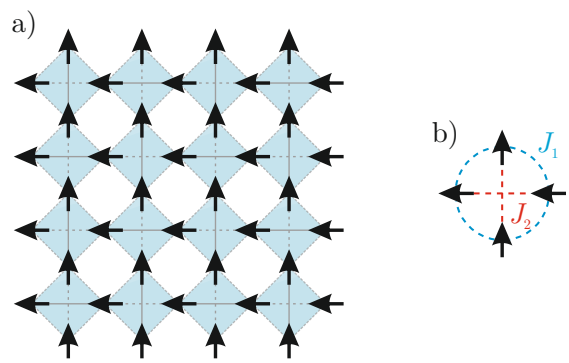

Figure 4.1: a) Square geometry results from the edge projection of pyrochlore crystal. The spins are placed at the apexes of the (blue) square lattice, pointing inside or outside the vertex. b) The projection breaks the symmetry of the problem. Since the first nearest neighbour (spins perpendicular to each other in the vertex) and the second neighbour (parallel spins) have different distances, they have different coupling strength constants J_1 and J_2, respectively.

If we consider the spin in a square spin system to only interact with their first and second neighbour (in both vertices they are forming), then the system can be described with the vertex models as it often is. The following sections will describe the vertex models [21,77] based on the square geometry.

4.1. Introduction to the square vertex models

Vertex models are models of statistical mechanics where an energy ε_i and Boltzmann weight are attributed to each possible configuration of the vertex, representing an atom or particle. In the artificial spin system, vertices are made of the spins meeting at the

junction. The vertices geometry can be adapted to fit the geometry of the problem, and the square geometry is the perfect playground for probing square-based vertex physics of the Sixteen-vertex and Six-vertex models.

In any vertex model, the interaction between vertices is provided only by the one Ising spin, shared by two neighbouring vertices. There are no long range interactions considered, and therefore the total energy of the system state is the sum of energy of individual vertex configuration: $E_{\text{system}} = \sum_i \varepsilon_i$.

4.1.1. Sixteen vertex model

Since there are four Ising spins at each vertex and each spin can have only two possible orientations, there are sixteen possible vertices. All of them are shown in Figure 4.2. The model that operates with all of these sixteen possible configurations is called *sixteen vertex model*.

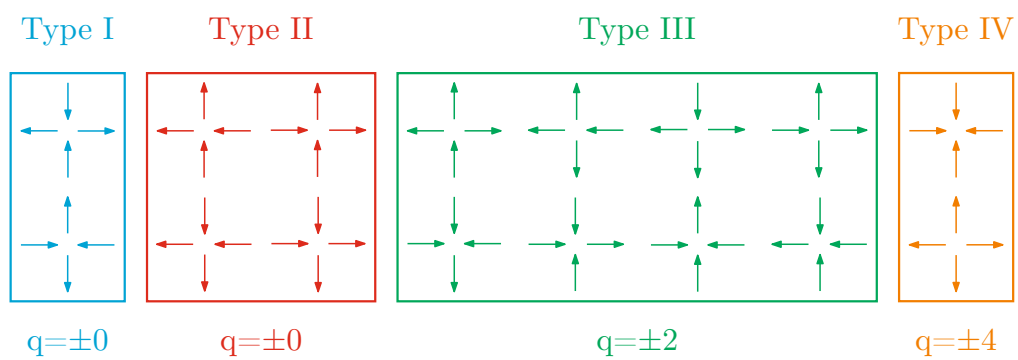

Figure 4.2: All sixteen possible vertex configurations divided into four types. The q is the associated magnetic charge of each type.

By considering the spin reversal symmetry (two configurations with all spins with opposite directions are equivalent) and rotational invariance (two configurations rotated by $n \cdot \frac{\pi}{4}$, where $n \in \mathbb{Z}$ are equivalent), the vertex configuration can be divided into four different types:

- *Type I* - There are two possible Type I vertices configurations where the first nearest neighbours' interactions are satisfied. Two spins are pointing into, and two are pointing outside the Type I vertex. The total magnetisation is zero.
- *Type II* - Type II vertices also have two spins pointing into the vertex and two outside. However, the Type II configuration is polarised, and the magnetisation is non-zero. In this configuration the second nearest neighbours' interactions are satisfied. There are four possible Type II vertices.
- *Type III* - there are Type III vertex configuration has eight possible configurations. Four have three spins pointing inside the vertex and one outside, and four with one spin pointing inside and three outside vertex. The magnetisation of the Type III vertex is non-zero.
- *Type IV* - There are two possible configurations of the Type IV vertex. All spins point inside or outside the vertex. The magnetisation of the Type IV vertex is zero.

The charge q (sum of spins pointing in and out of the vertex) of individual vertices is 0 for ice-rule-obeying Type I and Type II configuration, ± 2 for Type III configuration and ± 4 for Type IV.

The energies of individual types of vertices can be calculated as a sum of the coupling strength constant of each satisfied interaction (negative) and unsatisfied interaction (positive):

$$\varepsilon_I = -4J_1 + 2J_2 \tag{4.22}$$

$$\varepsilon_{II} = -2J_1 + 2J_1 - 2J_2 = -2J_2 \tag{4.23}$$

$$\varepsilon_{III} = -2J_1 + 2J_1 - J_2 + J_2 = 0 \tag{4.24}$$

$$\varepsilon_{IV} = 4J_1 + 2J_2 \tag{4.25}$$

In the description of the thermodynamic profile of the sixteen vertex model, let us assume that the J_1 coupling constant is bigger than J_2. It is a reasonable assumption when we consider that the spins sharing the J_1 constant are closer to each other. In this case, the energies of the types of the vertices are ordered as follows: $\varepsilon_I < \varepsilon_{II} < \varepsilon_{III} < \varepsilon_{IV}$. The ground state configuration of the sixteen vertex model with the $J_1 < J_2$ condition is made out from Type I vertices only - this ground state is referred to as the antiferromagnetic. As the system is heated up, the second ordered phase transition [78] occurs, and the high-energy phase is reached. In this phase, all vertices types are present proportionally to the possible realisation of each type.

4.1.2. Six vertex model

The six vertex model is a model which considers only the existence of the configurations which follow the ice-rule [7, 12]. Therefore only possible vertex configurations are Type I and Type II, as shown in Figure 4.3. The other types are disregard. However, since the symmetry of the vertex is broken and the coupling constant between the first nearest neighbours J_1 and the second nearest neighbour J_2 are generally not equivalent, there are three different realisations of the six vertex model:

Slater-KDP model where the $J_1 < J_2$, therefore, Type II vertices have lower energy and are ground state configurations and Type I are excitations.

Ice model, where the $J_1 = J_2$ and, therefore, the energies of both Type I and Type II are equal, and both types are ground state configurations.

The third possible realisation of the six vertex model is *F model*, where $J_1 > J_2$ and Type I vertex configuration is ground state one and Type II vertices are excitations.

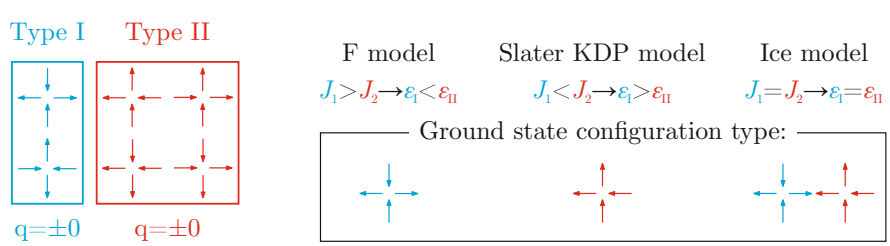

Figure 4.3: The six vertex model. Depending on the relation between the J_1 and J_2 coupling constant there are three realisation of the six vertex model.

F model

In the case that the J_1 coupling strength constant is bigger than J_2, the system is described by the F model. In this model, the energy of the Type I vertices is smaller than the Type II. One of the two possible ground state phases is shown in Figure 4.4 a).

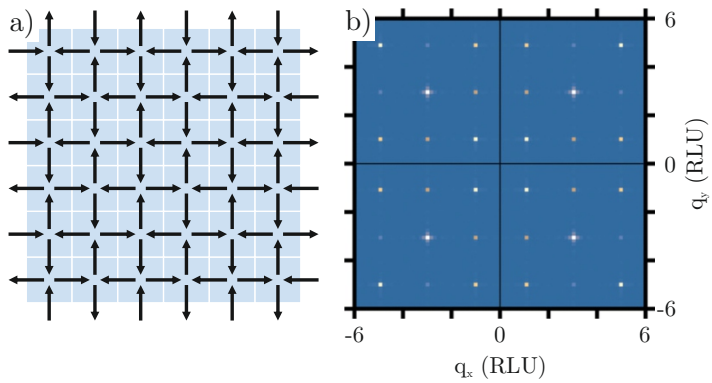

Figure 4.4: a) Example of real space ground state configuration of F model, the Type I vertices are perfectly ordered across the lattice. b) Example of F model MSF, where Bragg peaks indicate complete order. Images were taken and modified from [18].

The ground state phase is two times degenerated and perfectly ordered. Therefore, the MSF associated with this model show high intensive Bragg peaks all over the reciprocal space.

In 1967, Lieb [79] solved the F model and showed that the phase transition from the ground state to the high-energy phase is of infinite order [21] with order parameter which is infinitely smooth [80]. The high-energy phase of the F model is the mixture of the Type I and Type II vertices with the ratio 1:2, the same as in the Slater KDP model.

The specifics of this model will be discussed in more detail in section 4.4, where experimental analysis of the unique phase transition will be provided.

Slater KDP model

In Slater KDP model [81], the J_1 is smaller than J_2. Therefore the energy of the vertices $\varepsilon_I > \varepsilon_{II}$. The system minimises its total energy if all vertices are Type II, as shown in Figure 4.5 a).

Even though only Type II vertices are present, the orientation of the ferromagnetic lines spanning across the lattice is random (there is no ordering pattern). The ground state is degenerated. And the associated MSF does not show Bragg peaks, but the line patterns [18].

The thermodynamic profile of the Slater KDP model has two phases separated by first-order phase transition [82]. When the system is heated, the high-energy excitation of Type I starts to appear. The resulting high-energy phase of Slater KDP is a mixture of Type I and Type II vertices with the ratio 1:2 caused by the fact that there are two times more possible vertices of Type II.

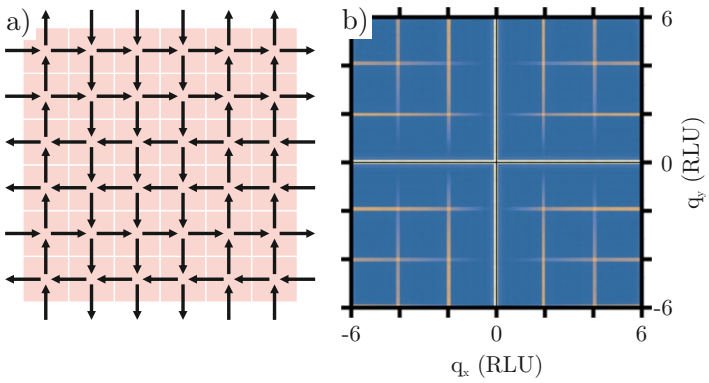

Figure 4.5: a) Example of real space ground state configuration of Slater KDP model, the Type II vertices are everywhere, but no ordering pattern is present. b) Example of MSF of Slater KDP model. Images were taken and modified from [18].

Ice model

When the coupling strength constant J_1 and J_2 are equal, the Ice model describes the system. The energies of Type I and Type II vertices are equal; therefore, the ground sate is made of a mixture of both types, as shown in Figure 4.6 a). This model perfectly describes the physics of the Ice. With the six-time degenerated ground state vertex configuration, the systems capturing the physics of the Ice models are true artificial spin ices.

The Ice model is, in fact, the high-energy phase of both Slater KDP and F model, and as such, there are no phase transitions. The ground state of this model is degenerated and disordered but correlated. Its pairwise correlations decay algebraically with the distance. Therefore the system described by the Ice model captures the physics of spin-liquids. An example of the MSF associated with the Ice model is shown in Figure 4.6 b).

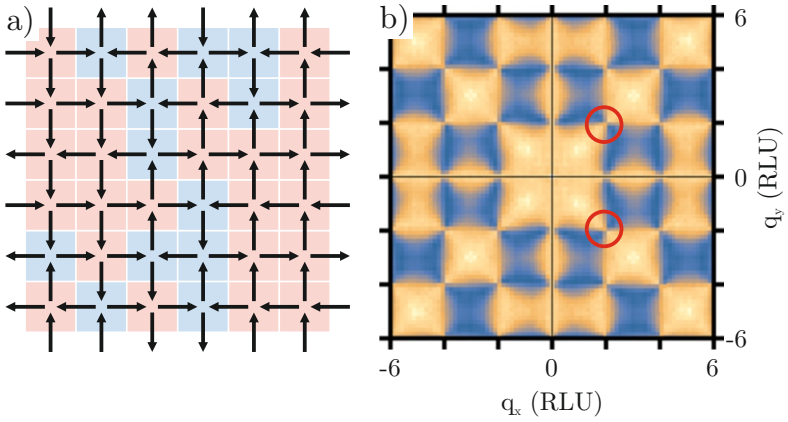

Figure 4.6: a) Example of real space ground state configuration of Ice model, the Type I and Type II vertices are disordered all across the lattice. b) Example of Ice model MSF. Images were taken and modified from [18].

The MSF of Ice model is typical of a cooperative frustrated paramagnet and the algebraic nature of the spin-spin correlations in real space translates into singularities in reciprocal space, the so-called pinch points [20, 83–85], highlighted by the red circles [18].

4.2. Artificial realisation of square models

In 2006 Wang et al. [11] fabricated systems made from small single-domain permalloy nanomagnets arranged to mimic the square geometry of the pyrochlore crystal edge projection. The schema of such a lattice is shown in Figure 4.7 a) together with b) AFM and c) MFM measurement result.

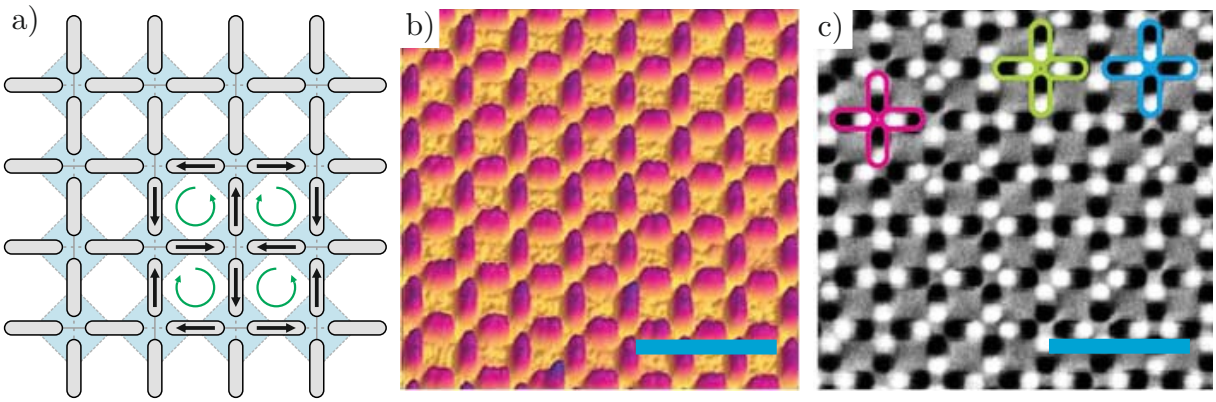

Figure 4.7: a) Square lattice schema resulting from the edge projection of pyrochlore crystal. The ground state vertex configuration forms alternating closed loops of magnetic flux with alternating chirality. b) AFM measurement of Wang's lattice, permalloy nano magnets forming the square lattice. c) Corresponding MFM signal from Wang's lattice. The nanomagnets are single-domain, and the black/white contrast indicates the orientation of magnetisation in the nanomagnet. There are vertices of Type I (pink), Type II (blue) and Type III (green) present. The blue scale bar is $1\,\mu$ long. Figures b) and c) are taken and edited from [11]

In the MFM measurement output, there are visible Type I, Type II and Type III vertices. Examples of them are highlighted in pink, blue and green colour respectively. The sample was demagnetised by filed-driven demagnetisation protocol.

Wang's experiment showed how it is possible to make an artificial spin system that fits the sixteen vertex model predictions relatively nicely. It could be expected to observe the physics of spin liquid in this system. However, due to the inequality of the coupling strength constant, which led to the lifting of the degeneracy of the system, this system failed to achieve a spin liquid state.

Instead, the square systems exhibit perfectly ordered antiferromagnetic ground state configurations made of Type I vertices everywhere. This configuration is characterised by alternating loops of closed magnetic flux, which are shown in Figure 4.7 a) [31,33,37,86]. At high temperatures, the system has paramagnetic ordering, which leads to the random vertex configuration of all types since the thermal energy overcomes the coupling constant. This effect allows the spin to fluctuate without limits. Nevertheless, Wang's study triggered a wealth of studies of artificial spin systems. Due to the perfectly ordered and well-described ground state of square spin systems, lattices were used to improve demagnetisation protocols [25,27,30,31], studying effects of thermal fluctuations [37,87], and understanding the behaviour of charge excitations (Type III defects) in ordered background [88,89] in and many more.

4.2.1. Presence of type III vertices

All studies so far that tried to reach any realisation of the six vertex models still had a non-negligible number of Type III vertices present. It can be said that instead of working in the framework of the six vertex models, it was always low-energy sixteen vertex model. However, this effect offers an interesting playground for studying the behaviour of Type III excitations. There are two very different types of Type III vertex configuration.

If the Type III vertex configuration exists in the ordered and uncharged background, these configurations should be called Type III *defects*. They are always linked to their counterpart[25] via series of spins [11,31,87,90,91]. These spins break the otherwise perfectly ordered ground state by making domain walls of the excited vertex configurations.

Examples of such situations are shown in Figure 4.8 a) where the Type III defects exist in ordered Type I background and are linked by the Type II vertex excitations (i.e. $\epsilon_I < \epsilon_{II}$). In b), the background is made out of saturated Type II vertices, and the link between the Type III defects is made out of Type I vertices (i.e. $\epsilon_I > \epsilon_{II}$). All the spins which reversal would lead to mutual annihilation of the Type III vertices are highlighted in orange colour. The path of the orange spins is usually called the Dirac string. The Type III defects cannot move without raising the energy of the system unless the movement is causing contraction of the Dirac string.

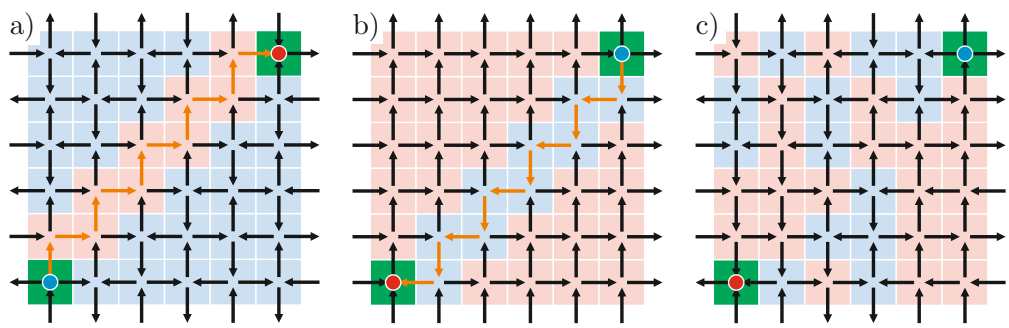

Figure 4.8: Examples of Type III defects present in the ordered: a) Type I background, b) Type II background and disordered c) spin liquid background. The Type III defects in the ordered background are coupled by a domain wall made of high-energy vertex configuration in case of a) and b). The defects in c) are decoupled. Taken and edited from [56].

Both examples a) and b) would have perfectly ordered MSF signals in reciprocal space. Completely different situations occur if the background is disordered spin liquid as shown in Figure 4.8 c). Suppose the system has a disordered background made of Type I and Type II vertices with the same energy (i.e. $\epsilon_I = \epsilon_{II}$). Both types are ground state configurations, and none of them is excitation. In this case, the Type III vertices are free to move since the movement of Type III will only cause the transformation of Type I into Type II or vice versa, and the system's total energy remains unchanged. It is also impossible to determine the path of the Dirac string, which means that the Type III vertices are decoupled, and one can not even tell if the pair belongs together. With all these properties, Type III can be described as particle-like objects in the diffused background and can be called *monopoles*.

[25] Or to the edge of the lattice in case of finite systems.

Studying the behaviour of the Type III excitations is another motivation to fabricate artificial systems with the desired ground state or background configuration.

4.3. Tuning the coupling constant

After the pioneering work done by Wang et al. [11], Möller and Moessner [92] introduced theoretical proposition how to renew the degeneracy of Wang's system to reach the Ice model realisation. To do so, the J coupling strength constant needs to be tuned so that the ratio between the $J_1/J_2 = 1$. In the following sections there will be presented three different approaches, which successfully regained the degeneracy of the spin ice systems.

4.3.1. Z-shifted square lattice

The first approach is based on the Möller [92] proposition. By elevating one sub-lattice (all nanomagnets pointing in the same direction) of the artificial square spin system into the hight h above the other, it is possible to change the coupling strength J_1 between the first neighbour while keeping the J_2 at a constant value. The schema of this solution is shown in Figure 4.9 a), where the blue sub-lattice is shifted above the green one.

Experimental realisation of Möller and Moessner proposition was done by Perrin et al. [56]. A two-step lithography process was used to fabricate such lattices. In the first step, the non-magnetic Ti/Ag bases were fabricated with the height h, but only in one direction. The following second step was used to deposit of magnetic permalloy square lattice. The perfect alignment of the lithography procedure enabled one permalloy sub-lattice to be elevated above the other, as is shown in Figure 4.9 b).

To better understand the scaling of the problem, micromagnetic simulations were done to see how the ratio between the coupling strength constant J_1/J_2 depends on the height offset h. The simulation outcome is shown in Figure 4.9 c), where the ratio $J_1/J_2 = 1$ at the $h = 120\,\mathrm{nm}$ [93].

A Series of lattices were fabricated by Perrin et al. to experimentally probe the critical height for which the system appears to meet the condition for square spin liquid $J_1 = J_2$. The MSF calculated from results obtained by measurement of the lattices with height offset 0 nm, 60 nm, 80 nm and 100 nm is shown in Figure 4.9 d). In the MSF, it is visible how the Bragg peaks, which indicate the perfect antiferromagnetic ordering in lattice without elevation, are replaced by the disordered background pattern connected to the square spin liquid for the lattices with offsets.

The offset height $h = 100\,\mathrm{nm}$ is the critical height - two factors can cause this deviation from the simulations. Firstly the simulations only considered the first neighbour interactions. However, Brunn et al. [93] proved that the effect of long range dipolar interaction up to the seventh nearest neighbour is not negligible. Secondly, the field-driven demagnetisation protocol was used to bring the systems into their low-energy states. The kinetics associated with the spin dynamics during the demagnetisation prefer forming the polarised lines in the lattices. Therefore the impact of J_2 is artificially increased, causing the ratio $J_1/J_2 = 1$ towards the smaller offsets.

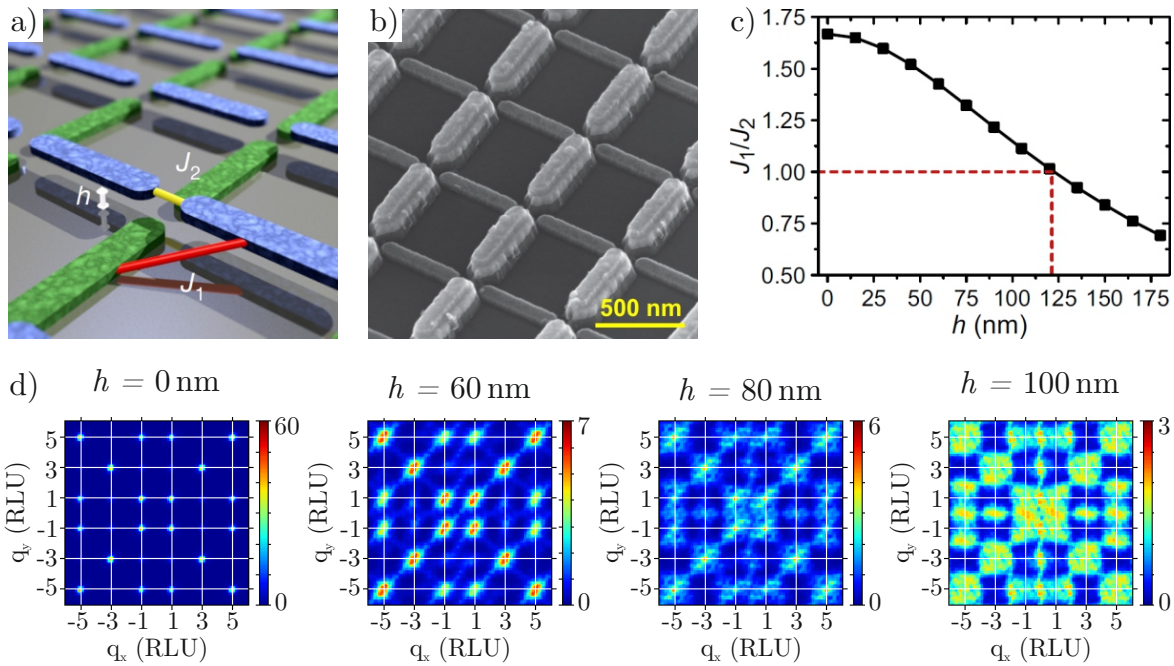

Figure 4.9: a) Schema of the square lattice with one sub-lattice shifted in z-direction above the green one. b) SEM image of a square lattice, one sub-lattice of permalloy nanomagnet is placed on non-magnetic titanium/gold bases. c) Simulation output showing the change in J_1/J_2 ratio depending on the h offset. It is shown that the ratio of $J_1/J_2 = 1$ for offset around 120 nm. d) MSF calculated from spin correlations of lattices with different offset h. It is shown that for the $h = 0$ nm, MSF indicates perfect antiferromagnetic ground state ordering, and as the h increase, the high intensive Bragg peaks fade and disordered background typical of Coulomb spin liquid starts to dominate for $h = 100$ nm which differs from the theoretically predicted value. Sub-figures a) and d) were taken from [56] and sub-figures b) and c) from [93].

4.3.2. Square lattice with interaction modifiers

Another approach to tuning the coupling strength constant was made by Östman et al. [94]. They found a way to tune the coupling constant effectively by adding a microscopic disc at the centre of the vertex, as shown in Figure 4.10 a). The discs play the role of an interaction modifier between the first and the second neighbours and have to be thin, so they have in-plane magnetisation and can be described as XY-like spins. Östman et al. studied the effect of the disc size on the vertex population. In Figure 4.10 b), the experiment results show how vertex population depend on the disc diameter and the related spacing between the disc and nanomagnets.

It is shown that for the lattice without discs, the vertex count of Type I is dominant, as expected, since it is a design similar to the Wang square lattice. The disc changes the vertex population radically, and the evolution of the population count shows that as the discs are larger, the population of Type II vertices increases. Around the disc diameter $D = 150$ nm, the Type I and Type II populations are equal. For the larger disc diameter, the Type II population dominate. The number of Type III vertices is steadily in-between $10 - 20\,\%$.

Calculated MSF for the lattices with $D = 150\,\text{nm}$ is shown in Figure 4.10 c) and it resembles that of the Ice model MSF. Östman approach is effective in designing lattices with variable ground states: antiferromagnetic ordering for none or small discs, ferromagnetic line pattern ordering for large discs and disordered ground state for the lattices with discs size around 150 nm.

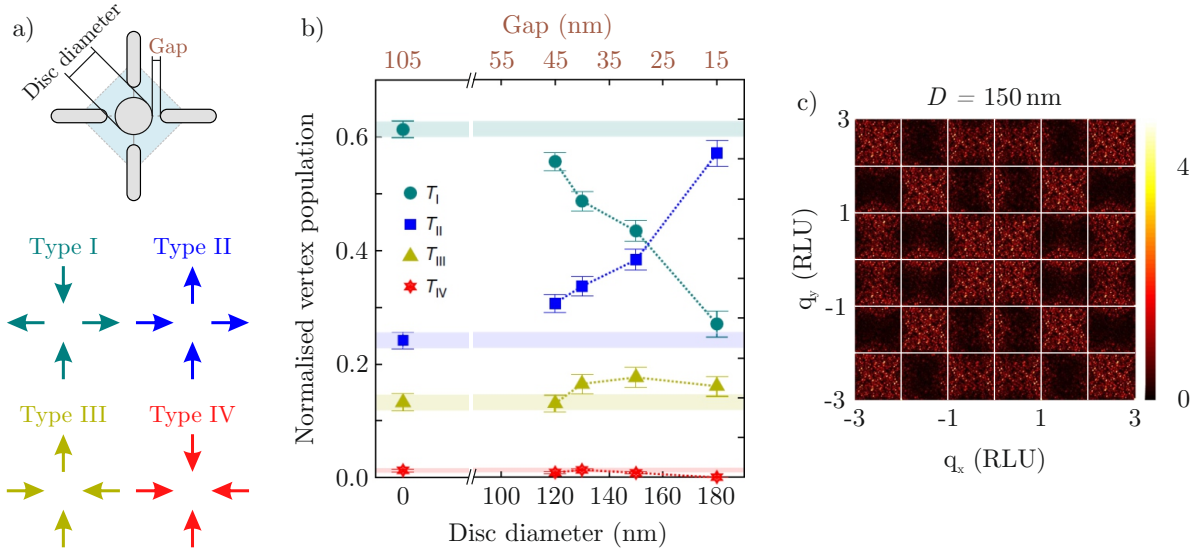

Figure 4.10: a) Schema of the modified vertex with the disc in the middle. b) Normalised vertex population dependence on disc diameter. The coloured stripes highlight the vertex populations count for the case where $D = 0\,\text{nm}$. For the lattice with disc diameter $D = 0\,\text{nm}$, the Type I vertices dominate and as the size of the disc's size increases, the Type II vertex population also increases. Around the diameter, $D = 150\,\text{nm}$, both types have similar population counts. For the large diameters, the energy of the Type II configuration is lower; therefore, this type dominates. c) MSF calculated from lattice with disc diameter $D = 150\,\text{nm}$, the disordered background of the MSF indicates that the lattice could be in a spin liquid state. All images taken and modified from [94].

Using the discs as the interaction modifiers is one possible way to effectively tune the coupling constant without fabricating non-planar geometry like the one described in section 4.3.1.

4.3.3. Square lattice with hole

Last but not least, in this thesis and [95], we present another way to tune the J coupling constant. Instead of having lattices made by single-domain nanomagnets that interact via dipolar interaction, we employ a similar strategy to the square lattice as we did with the kagome systems. The central idea of our approach is to connect the nanomagnets into one lattice. The system is transformed from a spin system where dipolar-driven many-body interactions are the driving force into one macro-object where the configuration at the vertex site is decided by competing micromagnetic energies. Thus we are effectively fabricating lattices suitable for studying vertex models since the lattice's driving force are micromagnetic forces forming the domain walls at the vertex site, and the vertices only interact with the shared nanomagnet.

An example of our lattice is shown in Figure 4.11 a). Part of the magnetic material has been removed from the vertex site, and only an empty hole remains. This defect plays a crucial role in tuning the energy of the domain walls at the vertex site. The resulting magnetisation configuration associated with each vertex type is shown in Figure 4.11 b). It can be seen that Type I domain wall forms an anti-vortex. Type II configuration resembles a homogeneously polarised domain wall across the vertex. Type III is similar to Néel transverse domain wall, and Type IV is a vortex domain wall.

The effect of the hole defect was theoretically analysed by micromagnetic simulations performed by Mumax3 code. The simulation parameters were set to resemble the real lattices. The spontaneous magnetisation was set $M_S = 8 \times 10^5$ A/m, the exchange stiffness was set to 10 pJ/m and damping coefficient $\alpha = 0.5$, hence the dynamics was not taken into account. Magnetocrystalline anisotropy was neglected since the material used in the experiment was permalloy. The simulation mesh size was set to $1 \times 1 \times 25$ nm.

The energy hierarchy of the vertex types can be finely tuned by changing the hole diameter at the vertex site as is shown in Figure 4.11 c), where results of micromagnetic simulations are plotted.

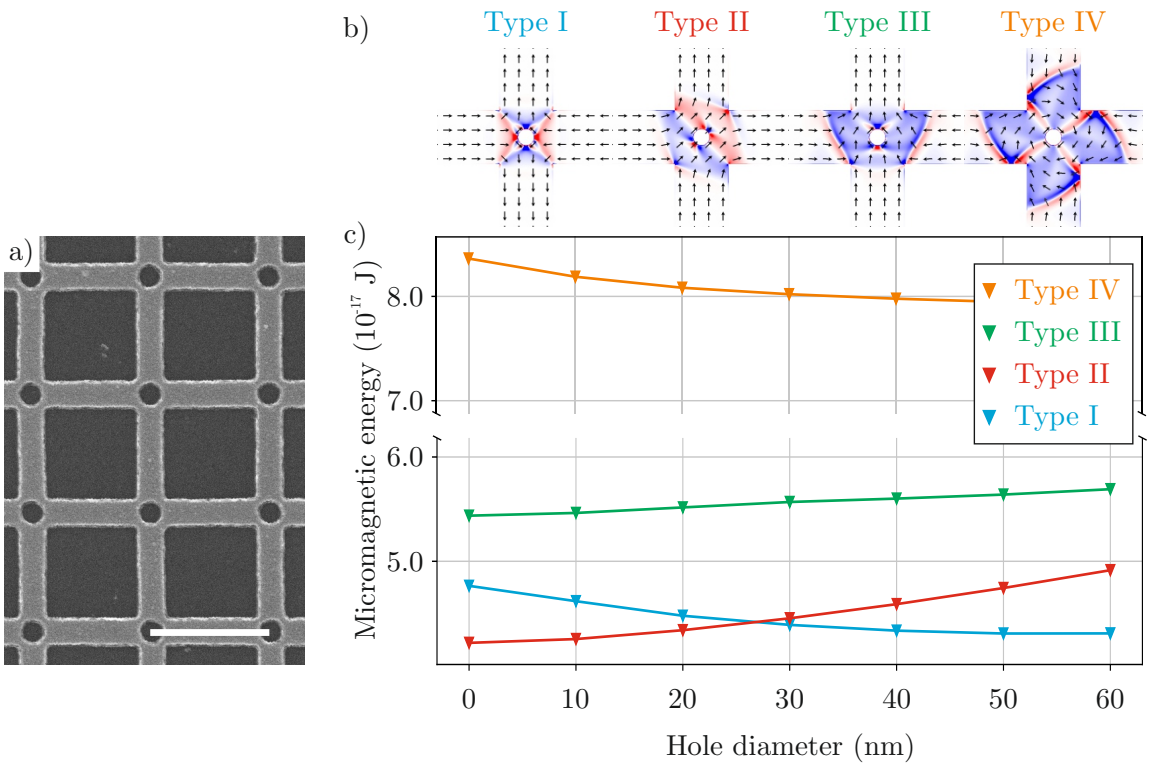

Figure 4.11: a) SEM image of one example of macrolattice with holes, the scale bar is 500 nm. b) Micromagnetic configurations of Type I, II, III and IV vertices. Black arrows show the direction of magnetisation. Blue and red contrast highlight the divergence of the magnetisation vector. c) Total energy of the vertex types depending on the hole diameter. Taken and edited from [95].

Energies of Type I and Type II vertices evolve opposite trends as the hole diameter increases. Type I magnetisation texture have an out-of-plane core in the centre of the domain wall. Therefore if the system has no hole or a small diameter, it costs more energy to stabilise Type I configuration. However, as the hole expands and the magnetic material

where the out-of-plane magnetisation should be stabilised is removed, the total energy of the Type I configuration decreases. With the presence of the large hole or entirely disconnected nanomagnets - this lattice prefers Type I vertices everywhere, similar to the Wang realisation as the interaction between first neighbours is stronger than between the second nearest neighbours.

Type II has the lowest energy in a fully connected grid without the hole's presence. As the hole diameter increases, so does the Type II energy. It is caused by an induced curl of the magnetic texture around the hole, which leads to increased exchange energy and the appearance of additional surface magnetic charges at the hole defect, leading to the increase of demagnetisation energy.

The energies of Type III and Type IV are always[26] higher for the simulated parameters than Type I and II. Type IV was never observed in well-demagnetised lattices, even for large holes. On the other hand, even though the energy of Type III vertices is always higher than Type I or Type II, the energy gap is still small to eliminate the presence of Type III configurations entirely.

Emulator of the six vertex model

The main advantage our approach compared to the rest of the studies is that the percentage of the Type III vertex in the population is lower than 1 % almost every time. Therefore most of the properties of the systems are unaffected by their presence (which is usually the case). Hence our system is close enough to the realisation of the six vertex model.

As seen from the evolution of the total vertex energy, the square lattice with a hole can have three possible ground states. While assuming that the high-energy configurations Type III and IV are fully suppressed, we can use our system as an emulator of the six vertex model. By changing the hole diameter, we can tune *fictional temperature* of the system. All measurements on our systems were done at room temperature, and the lattices are athermal. However, from the view of the energy gap between the ground state configuration and its possible excitations, it can be assumed that the system is warmer when the gap is smaller. The diameter of the hole functions as a temperature knob through which the system temperature can be adjusted. Hence if we fabricate lattices with identical parameters except for the hole diameter (which needs to variate), we can observe the system at different temperatures and observe how the system evolves.

The system prefers Type II everywhere for small hole diameters (or no hole), while Type I vertex configurations are excitations. In this realisation, the system can be described with the Slater KDP model, and by increasing the hole diameter, the energy gap between ground state configuration and excitations decreases up to the *critical hole diameter*, when the energy of Type II equals to Type I and the system reach its high-energy state, which is described by the Ice model. Starting from the Type II vertices everywhere, forming spanning ferromagnetic lines across the sample on lattices with small hole diameters and ending up with a liquid-like disorder phase on the lattice with the critical hole diameter. The hole diameter has a function of the heater in the Slater KDP. The fictional

[26] If the thickness of the nanomagnets is lowered to approx. 2 nm, the Type III configuration has lower energy than Type I for small holes.

temperature is proportional to the hole diameter, as is shown in Figure 4.12 in the red frame.

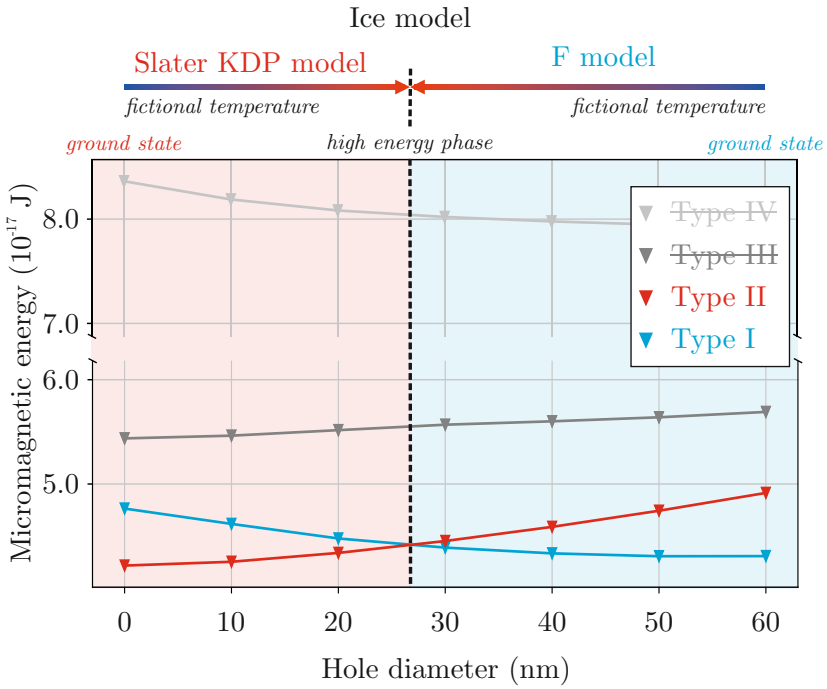

Figure 4.12: Schema of how emulator of individual six vertex model realisation works if the high-energy Type III and Type IV configurations are suppressed. The diameter of the hole can function as a thermostat for both Slater KDP and F model.

On the other hand, the systems prefer Type I vertices everywhere for large holes (or disconnected lattices). Large holes lead to the perfectly ordered ground state, while Type II vertices are the excitations of the system. The hole diameter also works as a regulator of the fictional temperature, but now the system is *heated* by the decrease of the hole diameter. Similar to the Slater KDP model's realisation, the system reaches the highest temperature on the lattice with the critical hole diameter.

To summarise, all three realisations of the six vertex model can be fabricated with the square lattice with holes. By using small lithography steps in the fabrication of the hole diameter, we can theoretically probe the thermodynamics of both Slater KDP and F models as they reach their high-energy ice-like disordered phase.

The experiment still needs to support our system's emulation of the Slater KDP model. To fabricate such small holes and systematically change their diameter by a few nanometres is beyond the limits of lithography techniques. On the other hand, the square lattice with holes has proven to help probe and better understand the F model [95].

Effect of the Field-Driven Demagnetisation and the Critical Hole Diameter

The critical hole diameter shown in both Figures 4.11 and 4.12, for which the energies of Type I and Type II configurations are equal, seems to be around 27 nm as deduced from micromagnetic simulations. However, this is not the value of the hole diameter for which we observe the ice-like disorder experimentally. MSF analysis of experimental results (shown in the following section) indicates that the disordered phase is observed for lattices

with 72 nm hole diameter. This offset is attributed to the field-driven demagnetisation protocol since the demagnetisation favours ferromagnetic line ordering. This effect is much stronger in our system than in standard disconnected square ice magnets [56] since the nanomagnets are connected in our system. Therefore, the domain walls responsible for the demagnetisation can travel across the lattice.

It can be said that the field-driven demagnetisation favours the formation of Type II vertices, therefore causing the need for the hole to be much bigger than in magneto-static simulations to compensate for the effect of the demagnetisation. This effect is beneficial since fabricating lattices with holes around the simulated values is extremely hard, if possible.

Another quite interesting observation we made from the experimental data analysis is that the range of the hole diameter for which the ice condition $J_1 = J_2$ is met is relatively narrow. Changing the diameter just by a few nanometers leads to detuning the ice condition. The critical hole diameter range approaches the lithography technique's limits. However, we could always see the Coulomb spin liquid regime on the lattices with the same critical hole diameter for a given set of fixed parameters during the fabrication procedure. Hence we emphasise that our results are robust and our approach is reproducible.

There are four main advantages of our approach:

1. With our approach, we can design lattices capturing all three realisations of the six vertex mode: Slater KDP for small hole diameter, F model for large hole diameters and Ice model for critical hole diameter.

2. Compared to the Perrin and Östman approaches, there is no need for the fabrication of three-dimensional arrays or extra thin layers. The fabrication is not trivial, but it can be done in one step lithography process.

3. The vertices in our lattices interact dominantly via shared nanomagnet. Thus our system is a good candidate as the vertex model simulator.

4. Last but not least, due to the connections at the vertex site, the stabilisation of the high-energy vertices (Type III and IV) and their count is lowered. The Type IV is fully eliminated[27]. The population of Type III vertices was reduced by a factor of ten compared to the Perrin and Östman approaches[28].

The combination of the ability to reach all realisation of the six vertex model, together with a small (negligible) number of the Type III defects, allows us to probe the low-energy manifold of the F model experimentally.

4.4. Experimental realisation of the F model

All the benefits of the square system with holes culminated in the attempt to visualise and analyse the infinite order phase transition of the F model in real space. Inspired by

[27]The measurement of Type IV which is shown 2.10 was only possible because the sample was severely damaged.

[28]In case of our systems, the percentage of Type III in the population is seldom higher than 1 %.

Nisoli's work [85], where the connection between the phase transition of the F model and the topological sectors is investigated, we decided to use Nisoli's description of the system via so-called *Faraday lines* (FL).

The motivation for our work is to investigate the infinitely continuous transition in real space, which was theoretically solved by Lieb [79], Kosterlitz and Thouless [96] and which now can be described by Faraday line representation introduced by Nisoli [85].

As mentioned in section 4.1.2, the F model has two distinguished properties: Firstly, the system is characterised by infinite order phase transition separating the antiferromagnetic ground state and high-temperature square ice phase. Secondly, the configurational space is divided into topological sectors [85,95]. Both these properties result from forbidding Type III and IV high-energy vertex configurations. Because of the non-existence of Type III and Type IV vertices, the system energies of the vertex I and II can be consider $0 = \epsilon_{\mathrm{I}} < \epsilon_{\mathrm{II}}$, the system exhibit only loop excitations made by clusters of Type II vertices.

4.4.1. Faraday lines

The example of the excited configuration of the F model is shown in Figure 4.13 where type II excitations (red background) separate the patches of type I vertices (blue/green) with opposite stagger parameter[29]. Only the type II vertices carry magnetic moments, which can be joined into the Faraday lines.

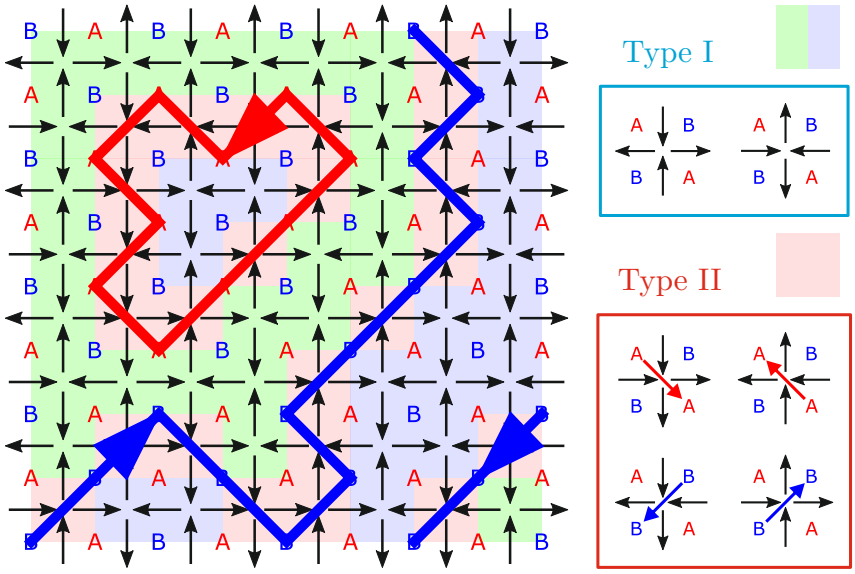

Figure 4.13: An example of an excited configuration of the F model. The type I vertices are depicted with a blue and green background, and the type II vertices are highlighted with red. The lattice can be divided into two alternating sublattices, A and B, as indicated by coloured letters A and B. Type I vertices are fully demagnetised. On the other hand, type II vertices carry magnetic moment, as indicated by the diagonal arrows. The arrow's colour is determined by parity depending on the sublattice they belong to (A is red, B is blue). Taken and edited from [95].

[29] Green and blue patches of the type I vertices are shifted by one vertex, hence incompatible and creating Type II vertex configuration.

By definition, in a six-vertex model, FL can only cross vertices diagonally; therefore, every single FL belongs only to one of the sublattices, A or B. The parity of the FL is derived from the sublattice the FL is sitting upon. Throughout this text, the colour code will not change, and FL with A or B parity have a red or blue colour. The FL with different parity cannot cross. Since only the type II vertices have non-zero energy, Faraday lines carry all the system's energy. Therefore they are elementary excitation of the F model [95], and the F model can be described as a loop gas [85].

FL are divided into two very different groups: Chiral closed loops (red FL in Figure 4.13). These types of loops are magnetisation-free. The inside of the closed loop has a vertices configuration with a total magnetisation of zero. Therefore the total magnetisation of the closed loop is always zero as well. This is true even for configurations where there are closed loops within the closed loops. Closed loops can be contracted to zero and do not interact with an external magnetic field since they do not contain any net magnetisation.

The second type of FL are system-spanning windings which carry all the net magnetisation. These FL cannot be contracted, forcing the system to fluctuate within a given topological sector [85, 97]. Examples of such FL are both blue FL shown in Figure 4.13.

FL with the same parity can be connected via *pinch-points*. An example of multiple connected FL can be seen in Figure 4.14 a), where three FL with the same parity (red colour) are placed onto a Type I vertex background. The pinch points are circled by a white circle in Figure 4.14 a). In Figure 4.14 b), the background texture was removed only to see the shape of FL. However, there is no way of knowing whether the FL is one closed loop or three separate closed FL as suggested in Figure 4.14 c) and Figure 4.14 d), respectively. FL configuration with n pinch-points have 2^n possible realisation.

So far, the attempts to probe the topological properties of the F model and its phase transition via two-dimensional lattices of interacting nanomagnets have failed. Even though the Wang lattice and other square geometries have the same ground state as the F model, their thermodynamics is described by the sixteen vertex model since the high-energy vertices (violating the ice-rule constraints) are present at a high rate. Types III and Type IV vertices are sources/sinks of magnetic flux, thus breaking the F model's properties.

In our work, we present how the F model can be approached. With our lattices with holes, we can probe and control the topological properties of the F model as the systems undergo the phase transition from the low-energy antiferromagnetic ground state into the high-energy ice-like phase. All this is possible because the number of Type III defects (which were not entirely suppressed) have marginal contribution since their vertex population is always less than 1 %.

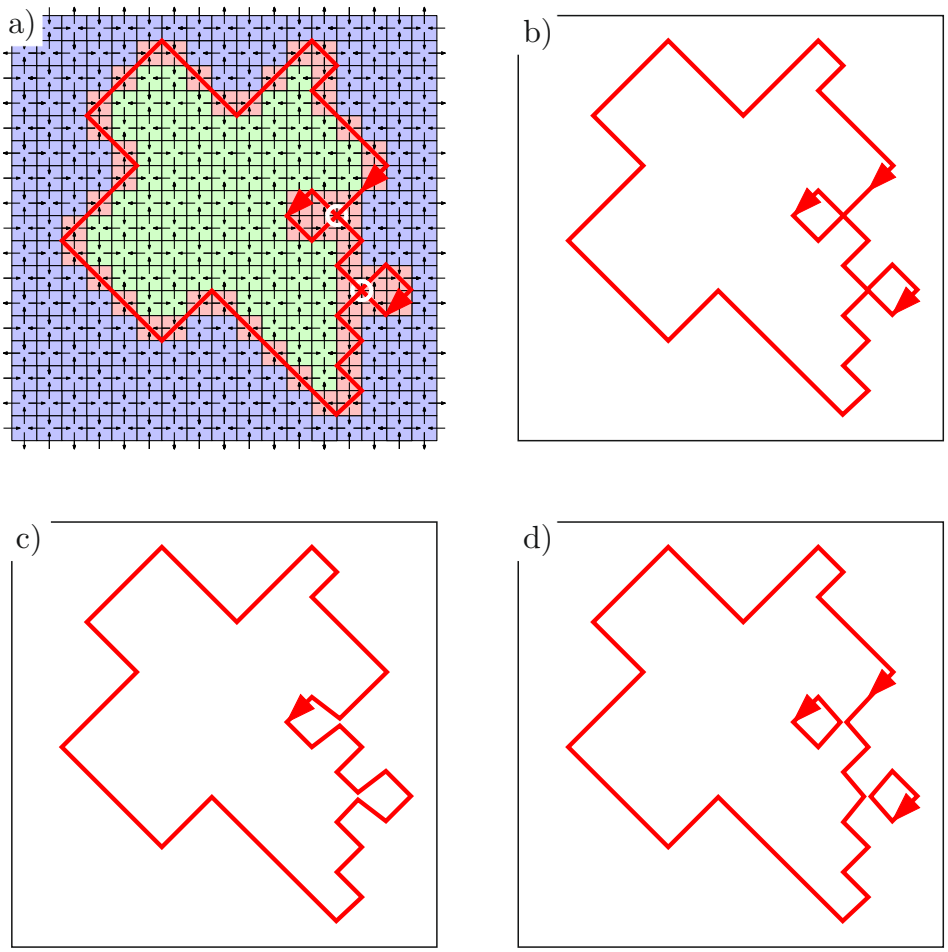

Figure 4.14: a) Example of FL configuration with two pinch-points (white circles). In the sub-paragraphs b), c), and d), different interpretations of the FL are visualised. Each cluster of FL connected with n pinch-points have 2^n possible realisation.

4.4.2. The experimental results

Our prediction has been tested on the series of square lattices with holes. The parameters of fabricated lattices are as follows: the nanomagnets' width is 100 nm, their thickness is 25 nm, and the vertex-to-vertex distance is 500 nm. The hole diameter changes from 70 to 120 nm. Each lattice contains 900 vertices. The material used for the fabrication of such lattices was permalloy. The demagnetisation protocol used to bring the lattices into their ground state configuration was 120 hours long.

For better statistics, several series of lattices were fabricated, all the fabrication parameters were the same for each series and all were exposed to the same demagnetisation protocol. The measurements were done on lattices with hole diameter $\phi = (120; 95; 90; 85; 80;$ and $72)$ nm. The reason for the gap between 120 nm and 95 nm hole diameter is that the changes on the lattices were small in this hole diameter region and the hole diameter 120 nm is the largest one which still does not disconnect the pseudo-spins forming the lattices.

The example of one series measurement visualised by FL interpretation is shown in Figure 4.15 a) together with the average MSF calculated from all series b).

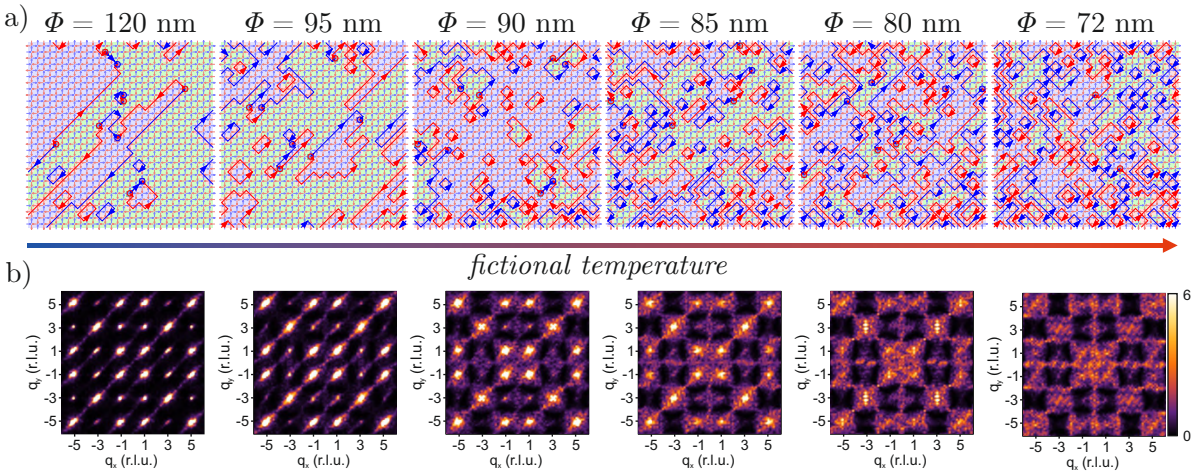

Figure 4.15: a) Real space FL visualisation and b) reciprocal space MSF analysis of the measured series of the lattices with different hole diameters. In the FL visualisation, we observe how two times degenerated antiferromagnetic background (blue and green) is made purely by Type I vertices, which are separated by FL made out of Type II vertices. The FL are blue or red depending on their parity, and their direction is visualised by a small arrow sitting on FL. Red and blue FL never connect, only if the Type III ice-rule-breaking vertex is present, as highlighted by the blue and red circles. Each MSF is averaged over four real space configurations with the same hole diameter (i.e., 3600 vertices) to get a better statistic. MSF covers ±6 reciprocal lattice units (RLUs), and all are scaled to the same intensity to visualise the evolution better. Taken and edited from [95].

The lattices with large holes are close to the antiferromagnetic ground state, and only a marginal percentage of vertices are other types than Type I. FL separates the two possible ground states with opposite stagger parameters of Type I. As the hole diameter decreases, so do the patches of the ground state and more system excitation (FL made by Type II vertices) starts to emerge. For the lattice with hole diameter 72 nm, the ratio between the populations of Type I and Type II vertices is almost 1 : 2 as the population of Type I is 35 % and Type II is almost 65 %. This population is comparable to what is expected from the square ice manifold. Since the change in the hole diameter is small and almost continuous, we can safely assume we are observing the snapshots of the phase transition between the F model antiferromagnetic ground state and its high-energy square ice phase.

As predicted by the simulations, the changes in the hole diameter lead to changes in the magnetic correlations. From the view of the energy gap between the Type I and Type II vertices, it can be said that the holes at the vertex site can be viewed as a heating knob. With the proper adjustments of the hole diameter, the system can be tuned into the Coulomb spin liquid phase [56, 58, 93, 94].

To support the claims about observing the phase transition, we compute MSF associated with all lattices. To improve the statistics, each MSF showed in Figure 4.15 b) were averaged over four different lattices (with the same parameters and exposed to the same demagnetisation protocol). Figure 4.15 b) also reveal gradual changes in the spin-spin correlation across the lattices. First, at the low temperature (large hole diameter $\phi \geq 95$ nm), we observe intense Bragg peaks in the MSF as the system is, for the most part, perfectly ordered. When the $80 \leq \phi \leq 95$ nm, there is visible coexistence of Brag peaks associated

with the ordering and ice-like disordered background. This background dominates as the Bragg peaks faint when heating the system. For the $\phi = 72\,\text{nm}$, the MSF shows a pattern associated with the square ice regime, i.e. diffused but structured [56, 93].

We want to emphasise that the magnetic correlations are affected even by the smallest step in the hole diameter (possible by the lithograph technique). The results we obtain are consistent over all the 24 lattices, proving the results are robust and series independent. In the figures 4.16 and 4.17, there is a complete measurement together with the FL visualisation and MSF analysis. We consistently start with large patches of antiferromagnetically ordered background for lattices with large hole diameters. We can reach the low-energy regime for lattices with $\phi = 72\,\text{nm}$.

To proclaim that we are working within the framework of the six-vertex model would be incorrect. The crucial benefit of our approach, resulting from the fact that the nanomagnets are connected, is the low percentage of Type III defects. Even with a long demagnetisation protocol, we still observe a non-zero population of the Type III vertices. These ice-rule-breaking configurations are always highlighted by a coloured circle and connect two FL with opposite parity. However, as mentioned before, the percentage of Type III vertices is typically 1 % or less, which is almost ten times less than in previous works with height offsets [56, 93], where field-driven demagnetisation was used.

The presence of Type III destroys the physics of the F model, however since we have such a small portion of the Type III defects, especially compared to the number of FL, we observe[30] we believe that our systems can be a good approximation of the F model.

Since our motivation is to describe the phase evolution of the F model and we believe that we are in good approximation to that model, we decided to use Nisoli's approach and analyse the FL. The FL we measured experimentally can be divided into two parts: Closed, chiral loops and open FL, where chirality is not defined. Open FL should not theoretically exist. However, since our systems have finite sites and non-periodic boundaries, the open FL span across the system and are anchored to the boundaries. Open FL carry the net polarisation. Both of these types of FL have defined parity. Chirality and parity are good indicators that our systems or demagnetisation protocol do not suffer from inherent bias.

The complex analysis of FL is shown in Figure 4.18. It is shown in the histogram in Figure 4.18 a) that both possible types of parity and chirality are equally populated in our experiment. Two main features were observed in the FL visualisation. The loop density is one of them. There is a visible increase in the loop density when the hole diameter decrease. This effect is evident for the smallest possible loops, in which the population increase in the order of magnitude through the series measurement as shown in Figure 4.18 b). This observation is direct evidence of the contraction of the FL as the system approaches its antiferromagnetic ground state [95].

The changes in the FL curvature were the second interesting feature observed due to the real space measurement. We plot average numbers of direction changes in Figure 4.18 c). When the system is approaching the ice regime FL have a meandering shape. On the other hand, when the antiferromagnetic patches are large, the FL are straight. This behaviour is probably a consequence of the tension of the antiferromagnetic background domains.

[30] There is typically ten times more FL than the Type III vertices when $\phi < 85\,\text{nm}$ [95].

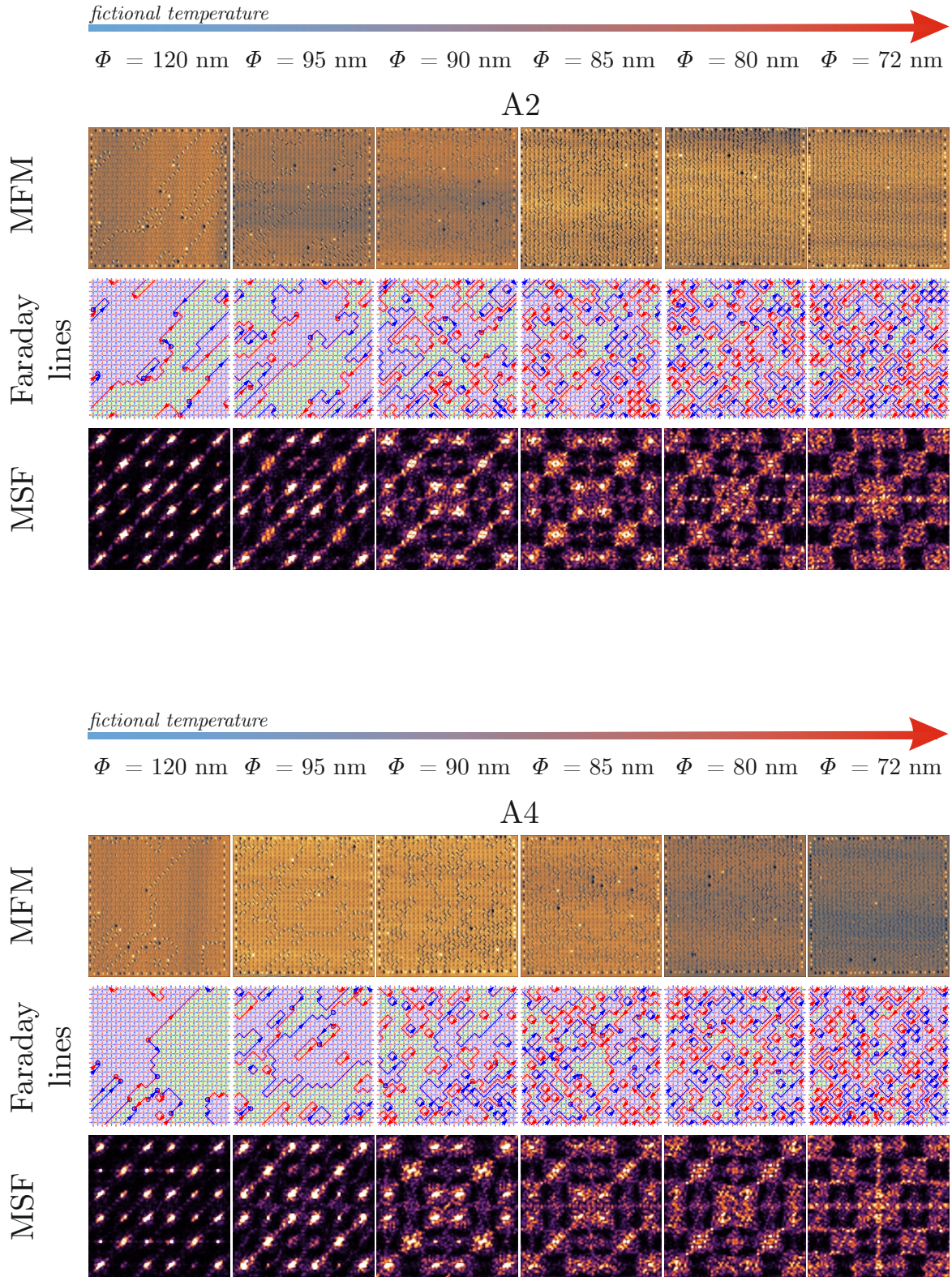

Figure 4.16: Two series of lattices: A2 and A4 analysed by magnetic force microscopy images and accompanied by the FL visualisation and MSF calculation for each specific lattice with different hole diameter, which represents fictional temperature of the system. Taken and edited from [95].

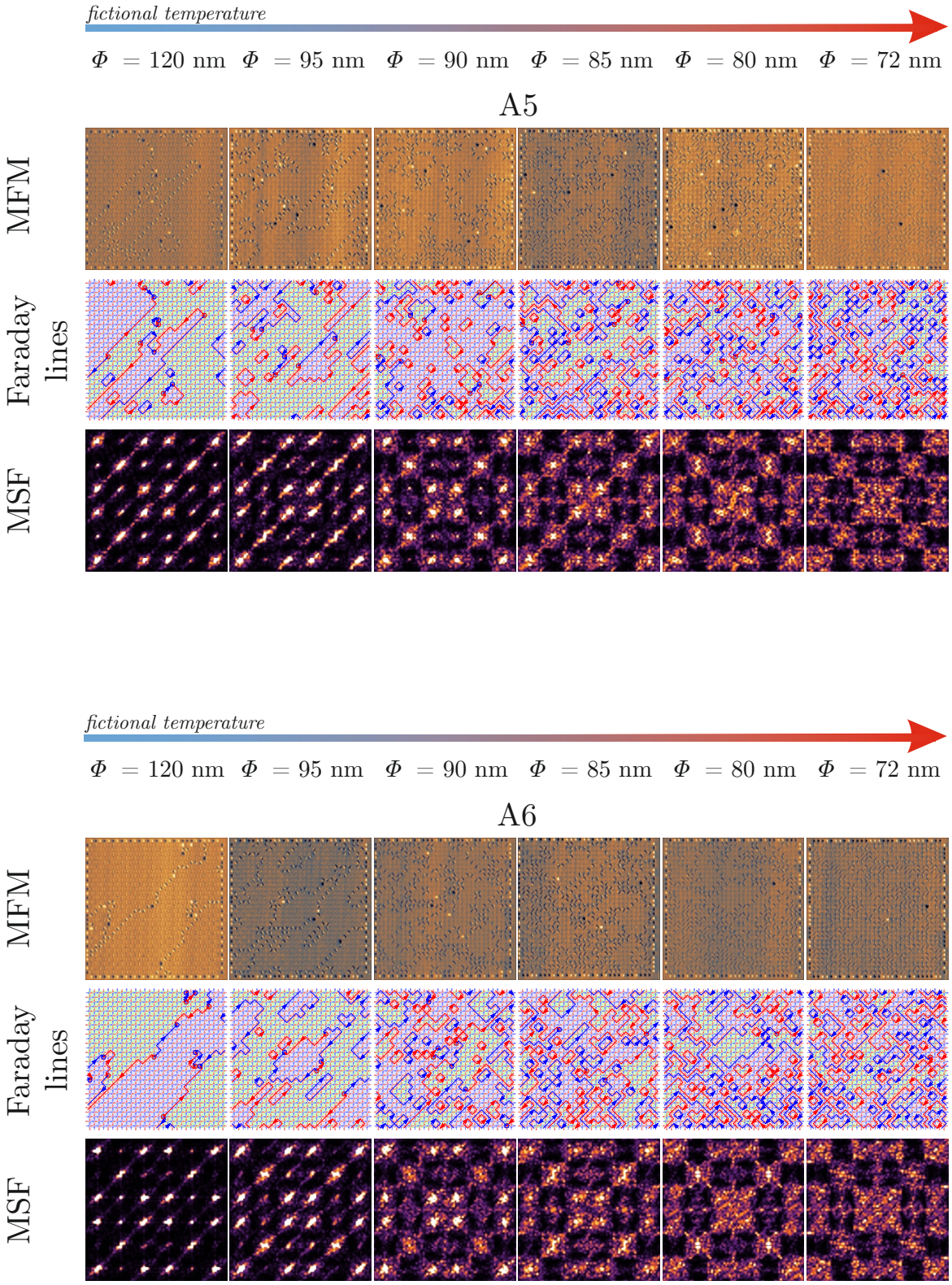

Figure 4.17: Two series of lattices: A5 and A6 analysed by magnetic force microscopy images and accompanied by the FL visualisation and MSF calculation for each specific lattice with different hole diameter, which represents fictional temperature of the system. Taken and edited from [95].

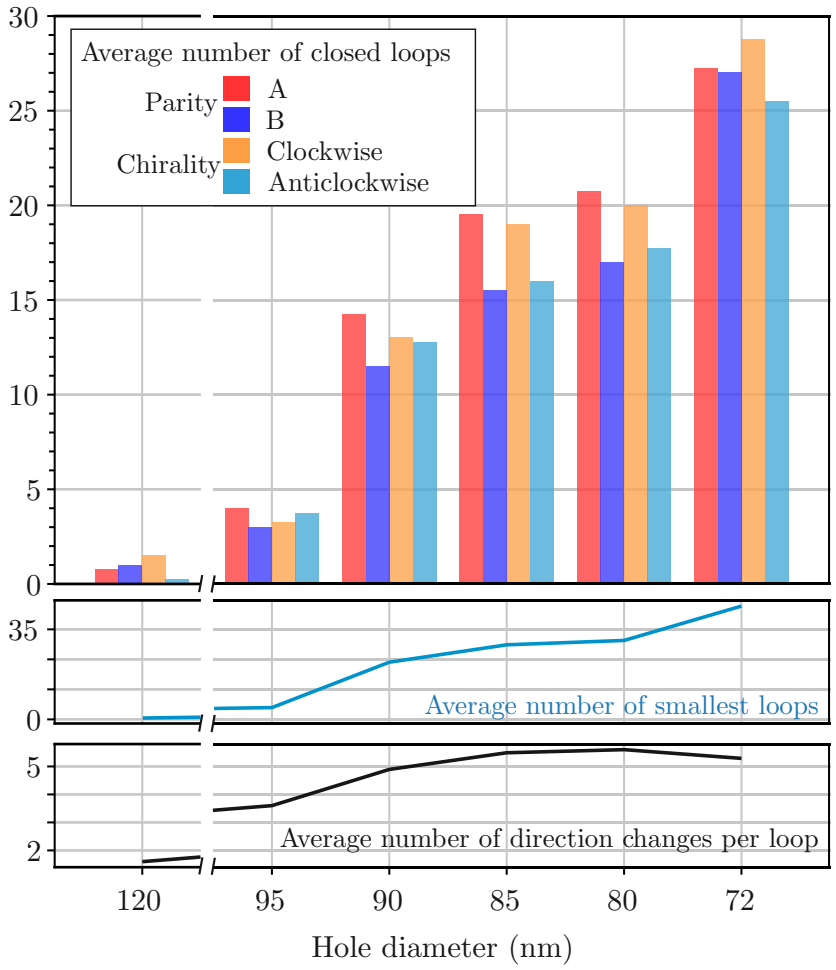

Figure 4.18: Analysis of the FL properties averaged from four lattices for each hole diameter. The Faraday loops are characterised by parity (A or B) and chirality (clockwise or anticlockwise). a) The histogram shows that both quantities are equally populated. Hence the experiment does not suffer from inherent or demagnetisation bias. b) An average number of the smallest possible Faraday loops, and c) an average number of changes in the direction of Faraday loops. Taken and edited from [95].

Type III defects in the antiferromagnetic ground state

The presence of the ice-rule-breaking type III vertices might be enough to destroy the topological properties of the FL. After energy analysis of the defect's local environment, we can prove that type III vertices are strongly connected to the Faraday lines as the system approaches its antiferromagnetic ground state. As can be seen in Figure 4.19 a) where two type III defects are present, there are only limited options of what the defects can do. There are three options:

1. The defect can move in by single spin flips around the FL and transforming the FL from parity A to B (or vice versa) until the two defects meet and recombine into a Type II vertex. The result of such defect movement can be seen in Appendix C. The resulting FL is a single parity and contains no defect.

2. The defect can propagate further into the antiferromagnetic background. An example of such a case is in Figure 4.19 b), where a defect can propagate in three

directions without increasing the system's energy. However, if it chooses the shown way, the next options are either to move back to the original place or increase the system's energy. Therefore it is statistically likely that the defects stay within the Type II domain wall.

3. The third option is a combination of the previous two. If two type II domain walls are in proximity but separated by Type I vertex, the defect can propagate through the background and then connect with the second domain wall.

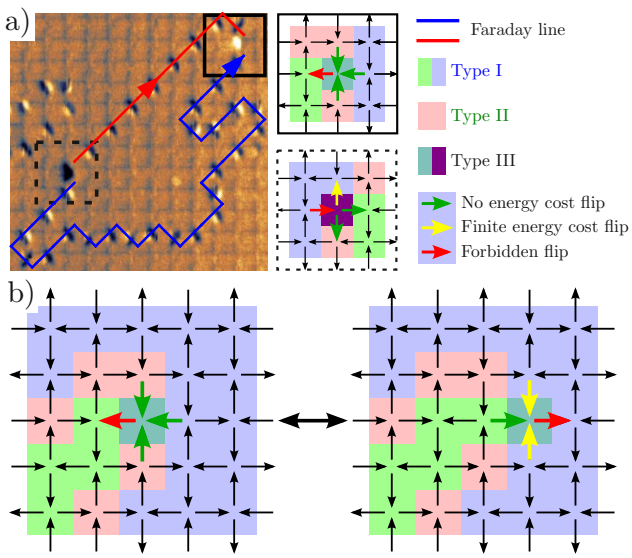

Figure 4.19: a) Pair of ice-rule-breaking type III defects connected by two FL of different parity together with a schema showing the local environment of the defects. The colour scheme illustrates the energy of individual spin flip connected to the defects: Green spin flips cost no energy, yellow spin flips would result in a configuration with higher energy than a pre-flip one, and red indicates spin-flips which would lead to the creation of Type IV vertex. b) Type III defect can propagate further into the Type I background. However, once the defect moves into the background, it is statistically likely to be pushed back into the Type II domain wall. Taken and edited from [95].

Type III defects are, in fact, immensely useful in bringing the system into its ground state. The system (without Type III vertices) can lower its energy only by collective spin-loop flips. However, these events are improbable in the experiment, which would mean that the system is frozen in the given configuration. On the other hand, if the system has Type III defects, these defects can move throughout the system and change its configuration (and lower its energy) during the demagnetisation process.

It is important to realise that all Type III vertices are confined to the FL and coupled with the defect of opposite magnetic charge or the lattice's edge.

The Type III vertices we observe in our measurement are relict of the demagnetisation protocol. However, since only a few residual Type III defects in our systems do not affect the properties of the FL majority, we conclude that our system is a good approximate of the F model.

Type III defects in the high-energy ice regime

In a previous section, we discussed how the Type III defects are connected to the FL and their ability to move throughout the system in the antiferromagnetic background. However, once the system is in the high-energy ice-like phase, tracking possible movements becomes more difficult. Since the Type I and Type II vertices have the same energy and the Type III vertices, do not feel the pressure of the background and are free to move. Another interesting fact is that the Type III vertices are decoupled, and no visible path connects them. As was explained in section 4.2.1.

In other words, the Type III vertices in the high-energy ice regime can be considered magnetic monopole quasi-particles. Comparison of the measurement and analysis of two lattices with different hole diameters is shown in Figure 4.20, where lattice hole diameters are a) $\phi = 120\,\mathrm{nm}$ and b) $\phi = 72\,\mathrm{nm}$.

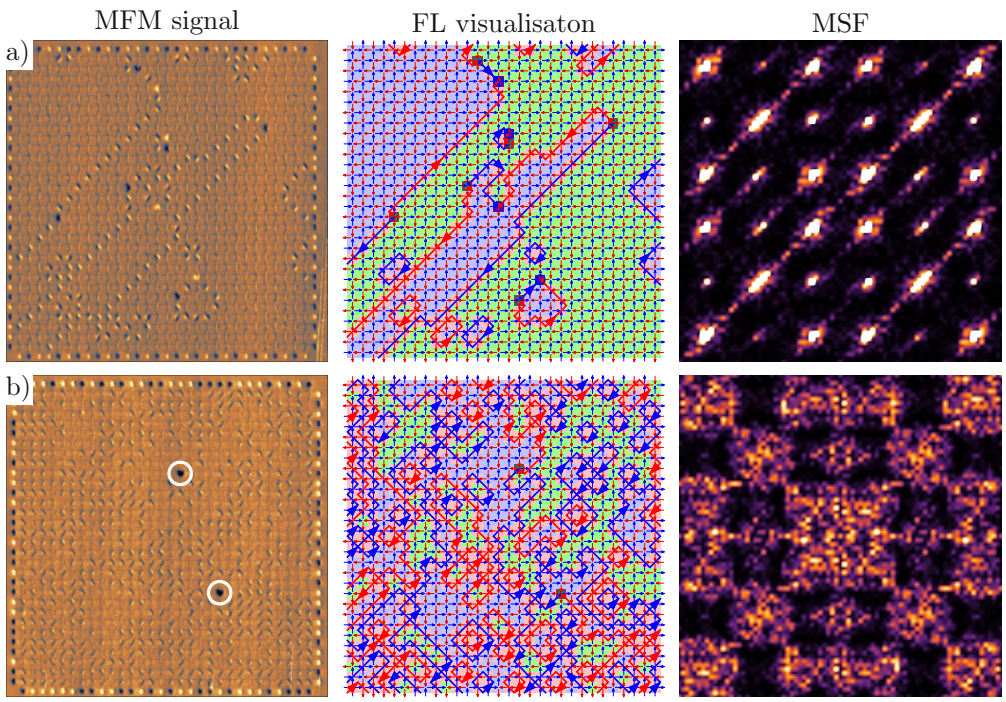

Figure 4.20: Comparison of MFM signal, FL visualisation and MSF of lattices with hole diameter a) $\phi = 120\,\mathrm{nm}$ and b) $\phi = 72\,\mathrm{nm}$.

In the case of the lattice with a large hole diameter, we observe several Type III vertices. All of them are connected to the lattice's edge or to the defect with an opposite charge, and they are tied to the Type II domain wall forming FL. On the other hand, in the lattice with a small hole diameter, there are two type III vertices (highlighted by the white circle). These two Type III vertices can freely move all over the lattice without feeling the background tension. Therefore we can see the real space measurement of magnetic monopoles in Figure 4.20 b).

4.5. Discussion and concluding remarks

In 2006 Wang et al. [11] made the first attempt to capture the physics of the spin ice crystals in two-dimensional square arrays of interacting nanomagnets. Due to the transformation of 3D pyrochlore crystal into the plane with edge projections, the interactions between the first J_1 and second J_2 neighbours were detuned.

In the past years, there have been attempts to correct this problem by changing the system's geometry by elevating one sub-lattice above the other to lessen the strength of the first neighbours [56, 93] or by adding interaction modifiers [94]. Both these solutions are described in section 4.3.

We are presenting another possible solution published in [95] and described in this chapter. Our approach relies on a different strategy than previous work. Instead of using the array of nanomagnets interacting via long range dipolar interaction, we transform the lattice into one macro-object, where all spins are connected—shifting from the spin-lattice into the vertex one. This transformation caused the dominant force to be no longer the dipolar interaction but micromagnetic forces competing at the vertex site. These forces can then be tuned at will with topological defects, in the case of our study, the holes at the vertex site.

By tuning the hole size at the vertex site, we can change the ground state configuration of the system. All three possible relations between the coupling strength J_1 and J_2 are achievable. If the system has large holes, the $J_1 > J_2$ and the antiferromagnetic background is reached. If the system has small holes, the system has a disordered background made by lines of spins going across the hole system since the relation between coupling strength is $J_1 < J_2$. However, the most interesting is finding out the critical hole diameter where $J_1 = J_2$. A system with the critical hole diameters regains the degeneracy of pyrochlore crystal and then can be used to study its rare spin configurations in real space.

Our concept is proven both numerically and experimentally. The lattices we design to capture the physics of the pyrochlore crystal in the two dimensions are a nice playground for probing the vertex models in real space with imaging techniques such as MFM.

Not only can we change the system's ground state by topological parameters, but we also believe that by fabricating a series of lattices with only small changes, we can probe the phase transition of individual models. The benefit of our approach is that the density of high-energy vertex configurations is in order of 1 % or less, which allows us not only to probe sixteen vertex model but approach the physics of six vertex model realisations as well.

We managed to use our systems to probe the topological phase transition of the F model, and we managed to observe the behaviour described by Nisoli [85] as much as the limitation of having a finite-size sample allows us.

The highlights of our work presented in this chapter are that we made the first attempt to emulate the F model experimentally. We also reached the high-temperature Coulomb spin liquid with residual topological defects (Type III vertices) below 1 %. Furthermore, similar to the research on the kagome lattices, we can use an external geometrical parameter as a heating knob to tune the temperature of the studied model at will.

Our work lays the ground for further studies of the F model, where the phase transition analysis can still be improved and for the study of the magnetic monopole dynamic and other behaviours.

Chapter 5: Concluding remarks

Artificial systems are a powerful tool to probe the behaviour of exotic physical phenomena in laboratory-controlled environments. With advanced fabrication techniques, we can now design new macro atoms that can be characterised in real space. Then simply by playing with geometrical parameters, we can tune the Hamiltonians of such systems. In this work, we studied the physic of geometrically frustrated magnetic artificial systems called spin-liquids.

The presented work briefly overviews the origin of artificial systems and frustrated materials. A description of the peculiar behaviour of frozen water and its puzzling properties is provided, as well as its similarity to the magnetically frustrated spin ice systems. Artificial spin ice systems are specially designed to mimic the behaviour of real natural materials but as two-dimension systems, which can serve as an almost unlimited playground for researching the statistical models and exotic physics of spin liquids and magnetic monopoles.

We focused our research on two types of artificial spin systems: kagome and square dipolar spin systems. Both systems are designed to allow us to directly measure the individual spin degree of freedom in a real space with imaging techniques such as MFM.

The main problem of the Kagome dipolar spin system that we addressed in this work was the inability of the system to undergo the phase transition into its low-energy manifold. This problem is caused by the dynamical freezing [63], and we could bypass it by imprinting the desired phase into the topography of the lattice. Even though we destroyed the system's symmetry, we could prove that our modified systems were not stuck at one effective temperature and could be heated up and shifted in the thermodynamic profile. We still observe both correlation coefficients and MSF, which perfectly correspond with the theoretical prediction for the Kagome dipolar spin ice system. We were able to design lattices, where only by use of the field-driven demagnetisation protocol, the spins were self-ordered into configurations belonging to the long-range order and spin liquid 2 phase. The ability to imprint any thinkable spin configuration comes at the cost of changing the system's Hamiltonian and related thermodynamic profile. The unanswered question concerning the kagome lattice with notches is, how is it possible to observe a perfect fit with the thermodynamics of kagome dipolar spin ice when the Hamiltonians are different?

Our approach that relies on drastically changing the system's geometry could be helpful in the domain wall propagation-based devices. The ability to finely tune the probability of direction propagation of domain walls can be utilised within the magnetic logic gates of next-generation magnetic neural computations.

While we did break the symmetry of the kagome dipolar system when using the notches to imprint desired phases, it was the other way around with the square system. The square dipolar spin system lost its symmetry during the transformation process from the three-dimensional crystals. By connecting the system and tuning the energies of the vertices, we regained the lost degeneracy and restored the system symmetry. We tuned the system to capture the physics of Coulomb spin liquid, which is characterised by the low-energy loop dynamic.

Compared to the previous work, we were able to design systems where the high energy vertex configurations (which are responsible for killing the loop dynamics) are diminished

to the count smaller than 1 %. We provided an elegant way to restore the degeneracy of the dipolar square system. We also found a direct application of our system as the experimental emulator of celebrated the celebrated six-vertex model.

By carefully tuning the hole's diameter and starting from the proper configuration, we provided the first attempt to visualise the phase transition of the F model in real space. Not only were we successful in proving the theoretical concepts of the Faraday lines defined by Nisoli [85] (as much as the finite size systems allowed us), but we also provided new observations about the model behaviour during the phase transition that were not deduced theoretically such as a role of the background tension on the properties of the Faraday lines.

Due to its properties, the square lattice with a hole is suitable for further research of the F model. Plenty of questions remain unanswered, such as the role of the monopole dynamics in the ice regime, a fluctuation between the topological sectors, response to the external magnetic field and so on.

We provided a thorough investigation of the F model evolution on the lattices with large to intermediate hole diameters. However, there is still the second part of our simulated prediction, dealing with the Slater KDP model. Our square system with small holes could also provide a suitable research platform for experimentally exploring this eluding model.

Our research is based on a bold assumption which we were able to support with the experimental result; we are assuming that the following ways of probing the systems will yield comparable results. Instead of probing the behaviour of one system (with one Hamiltonian) at different temperatures, we explore the behaviour of different systems (different Hamiltonians caused by different notch or hole sizes) at the same temperature (after the same demagnetisation protocol). We believe that in the framework of our experiment, these approaches are somewhat interchangeable. Therefore we can provide the thermodynamic profiling of our systems.

The reason we were able to address these scientific problems successfully is our innovative strategy. Instead of fabricating the systems where the dipolar interactions between all elements try to minimise the system energy, with our design, we switched from the spin systems to the vertex systems. The simplicity of this approach allowed us to bypass the many-body interaction and focus solely on tuning the micromagnetic energies forming domain walls at the vertex sites. We even discovered that from the point of view of the energy gap between the ground state configuration and system excitation, both topological defects (notch and hole) could serve as a system heater. We tied the external geometrical parameter with the internal temperature of the system. All this while working at room temperature with athermal systems.

We want to emphasise that this approach is not restricted to kagome or square lattice use. Almost any currently studied lattices with in-plane magnetisation [98, 99] can be modified similarly to our systems.

If the lattice is connected and the system has asymmetrical vertices, using the notches with the proper parameters can help tune the favourable spin configurations without any additional symmetry breaking. The lattices which could be easily modified with the notch are, for example, Santa Fe, Tetris, Brickwall or Shakti lattices.

When there is a need for recovering or retaining the symmetry in the systems with symmetrical vertices, one might consider using hole (or even square) defects to tune the energy of the incurred vertex configuration, for example, in Square, Toroidal, kagome, Voretex, Pentagonal and Dice lattices.

In all the lattices mentioned above, the easy way to imprint desirable configurations can be used to study the interface of individual phases.

All the research done in this thesis was done on athermal systems using magnetic field-driven demagnetisation only. It would be fascinating to try to probe these systems experimentally with thermal demagnetisation, especially when real-time measurement is possible. Visualising the real-time evolution of the systems would help to understand the mechanism behind dynamics. It is unlikely (though not impossible) to design an experiment where the researchers could observe the real loop dynamics, thermally active systems are a promising territory where this exotic mechanism could be found.

Reference list

[1] S. Blundell, *Magnetism in condensed matter*. New York: Oxford University Press, 1. ed., 2001.

[2] C. Kittel, *Úvod do fyziky pevných látek*. Praha: Academia, 1. ed., 1985.

[3] J. Fuka and B. Havelka, *Elektřina a magnetismus*. Praha: Státní pedagogické nakladatelství, 3. ed., 1979.

[4] B. Sedlák and I. Štoll, *Elektřina a magnetismus*. Praha: Academia Karolinum, 3., v nakl. karolinum 2. ed., 2012.

[5] O. Fruchart, *Lectures notes on Nanomagnetism*. Grenoble: SPINTEC, november 4, 2016 ed., 2016.

[6] W. F. Giauque and M. F. Ashley, "Molecular rotation in ice at 10 k. free energy of formation and entropy of water," *Physical review*, vol. 43, no. 1, p. 81, 1933.

[7] L. Pauling, "The structure and entropy of ice and of other crystals with some randomness of atomic arrangement," *Journal of the American Chemical Society*, vol. 57, no. 12, pp. 2680–2684, 1935.

[8] A. Y. Klimenko, "Teaching the third law of thermodynamics," *The Open Thermodynamics Journal*, vol. 6, 2012.

[9] M. Tanaka *et al.*, "Domain structures and magnetic ice-order in nife nano-network with honeycomb structure," *Journal of applied physics*, vol. 97, no. 10, p. 10J710, 2005.

[10] M. Tanaka *et al.*, "Magnetic interactions in a ferromagnetic honeycomb nanoscale network," *Physical Review B*, vol. 73, no. 5, p. 052411, 2006.

[11] R. F. Wang *et al.*, "Artificial spin ice in a geometrically frustrated lattice of nanoscale ferromagnetic islands," *Nature*, vol. 439, 2006.

[12] J. D. Bernal and R. Fowler, "A theory of water and ionic solution, with particular reference to hydrogen and hydroxyl ions," *The Journal of Chemical Physics*, vol. 1, 1933.

[13] R. L. Stamps and R. E. Camley, *Solid State Physics*. Academic Press, 2014.

[14] M. Harris *et al.*, "Geometrical frustration in the ferromagnetic pyrochlore $Ho_2Ti_2O_7$," *Physical Review Letters*, vol. 79, no. 13, p. 2554, 1997.

[15] A. P. Ramirez *et al.*, "Zero-point entropy in 'spin ice'," *Nature*, vol. 399, no. 6734, pp. 333–335, 1999.

[16] S. Bramwell *et al.*, "Spin correlations in ho 2 ti 2 o 7: a dipolar spin ice system," *Physical Review Letters*, vol. 87, no. 4, p. 047205, 2001.

[17] H. Kadowaki *et al.*, "Neutron scattering study of dipolar spin ice ho 2 sn 2 o 7: frustrated pyrochlore magnet," *Physical Review B*, vol. 65, no. 14, p. 144421, 2002.

[18] N. Rougemaille and B. Canals, "Cooperative magnetic phenomena in artificial spin systems: spin liquids, coulomb phase and fragmentation of magnetism," *The European Physical Journal B*, vol. 92, 2019.

[19] J. Villain, "Insulating spin glasses," *Zeitschrift für Physik B Condensed Matter*, vol. 33, no. 1, pp. 31–42, 1979.

[20] C. L. Henley, "The Coulomb phase in frustrated systems," *Annual Review of Condensed Matter Physics*, vol. 1, 2010.

[21] E. H. Lieb, *Exact Solution of the F Model of an Antiferroelectric*, pp. 453–455. Berlin, Heidelberg: Springer Berlin Heidelberg, 2004.

[22] A. Vansteenkiste *et al.*, "The design and verification of MuMax^3," *American Institute of Physics*, vol. 4, 2014.

[23] A. Broers, "Resolution limits for electron-beam lithography," *IBM Journal of Research and Development*, vol. 32, no. 4, pp. 502–513, 1988.

[24] W. Hu *et al.*, "Sub-10 nm electron beam lithography using cold development of poly (methylmethacrylate)," *Journal of Vacuum Science & Technology B: Microelectronics and Nanometer Structures Processing, Measurement, and Phenomena*, vol. 22, no. 4, pp. 1711–1716, 2004.

[25] R. F. Wang *et al.*, "Demagnetization protocols for frustrated interacting nanomagnet arrays," *Journal of Applied Physics*, vol. 101, 2007.

[26] C. Nisoli *et al.*, "Ground state lost but degeneracy found: The effective thermodynamics of artificial spin ice," *Physical review letters*, vol. 98, no. 21, p. 217203, 2007.

[27] X. Ke *et al.*, "Energy minimization and ac demagnetization in a nanomagnet array," *Physical review letters*, vol. 101, no. 3, p. 037205, 2008.

[28] E. Mengotti *et al.*, "Building blocks of an artificial kagome spin ice: Photoemission electron microscopy of arrays of ferromagnetic islands," *Physical Review B*, vol. 78, no. 14, p. 144402, 2008.

[29] J. Li *et al.*, "Comparing artificial frustrated magnets by tuning the symmetry of nanoscale permalloy arrays," *Physical Review B*, vol. 81, no. 9, p. 092406, 2010.

[30] J. Morgan *et al.*, "Linear field demagnetization of artificial magnetic square ice," *Frontiers in Physics*, vol. 1, p. 28, 2013.

[31] J. Morgan *et al.*, "Thermal ground-state ordering and elementary excitations in artificial magnetic square ice," *Nature Physics*, vol. 7, no. 1, pp. 75–79, 2011.

[32] J. Cumings, "Artificial ice goes thermal," *Nature Physics*, vol. 7, no. 1, pp. 7–8, 2011.

[33] A. Farhan *et al.*, "Direct observation of thermal relaxation in artificial spin ice," *Physical review letters*, vol. 111, no. 5, p. 057204, 2013.

[34] A. Farhan *et al.*, "Thermally induced magnetic relaxation in building blocks of artificial kagome spin ice," *Physical Review B*, vol. 89, no. 21, p. 214405, 2014.

[35] K. Hofhuis *et al.*, "Real-space imaging of phase transitions in bridged artificial kagome spin ice," *Nature Physics*, pp. 1–7, 2022.

[36] V. Kapaklis *et al.*, "Melting artificial spin ice," *New Journal of Physics*, vol. 14, no. 3, p. 035009, 2012.

[37] V. Kapaklis *et al.*, "Thermal fluctuations in artificial spin ice," *Nature nanotechnology*, vol. 9, no. 7, pp. 514–519, 2014.

[38] U. Arnalds *et al.*, "Thermalized ground state of artificial kagome spin ice building blocks," *Applied Physics Letters*, vol. 101, no. 11, p. 112404, 2012.

[39] F. Montaigne *et al.*, "Size distribution of magnetic charge domains in thermally activated but out-of-equilibrium artificial spin ice," *Scientific reports*, vol. 4, no. 1, pp. 1–5, 2014.

[40] S. Porthun, L. Abelmann, and C. Lodder, "Magnetic force microscopy of thin film media for high density magnetic recording," *Journal of magnetism and magnetic materials*, vol. 182, no. 1-2, pp. 238–273, 1998.

[41] P. Eaton and P. West, *Atomic force microscopy.* Oxford university press, 2010.

[42] U. Hartmann, "Magnetic force microscopy," *Annual review of materials science*, vol. 29, no. 1, pp. 53–87, 1999.

[43] Z. Budrikis, P. Politi, and R. Stamps, "Vertex dynamics in finite two-dimensional square spin ices," *Physical Review Letters*, vol. 105, no. 1, p. 017201, 2010.

[44] I. A. Chioar *et al.*, "Nonuniversality of artificial frustrated spin systems," *Physical Review B*, vol. 90, no. 6, p. 064411, 2014.

[45] I. A. Chioar *et al.*, "Kinetic pathways to the magnetic charge crystal in artificial dipolar spin ice," *Physical Review B*, vol. 90, 2014.

[46] Y. Perrin, *Réseaux artificiels à frustration géométrique.* PhD thesis, Université Grenoble Alpes, 2016.

[47] G. Wannier, "Antiferromagnetism. the triangular ising net," *Physical Review*, vol. 79, no. 2, p. 357, 1950.

[48] I. Syôzi, "Statistics of kagomé lattice," *Progress of Theoretical Physics*, vol. 6, no. 3, pp. 306–308, 1951.

[49] K. Kanô and S. Naya, "Antiferromagnetism. the kagomé ising net," *Progress of theoretical physics*, vol. 10, no. 2, pp. 158–172, 1953.

[50] A. J. Macdonald, P. C. Holdsworth, and R. G. Melko, "Classical topological order in kagome ice," *Journal of Physics: Condensed Matter*, vol. 23, no. 16, p. 164208, 2011.

[51] S. Zhang *et al.*, "Perpendicular magnetization and generic realization of the ising model in artificial spin ice," *Physical review letters*, vol. 109, no. 8, p. 087201, 2012.

[52] I. A. Chioar, N. Rougemaille, and B. Canals, "Ground-state candidate for the classical dipolar kagome ising antiferromagnet," *Physical Review B*, vol. 93, no. 21, p. 214410, 2016.

[53] N. Rougemaille *et al.*, "Artificial kagome arrays of nanomagnets: a frozen dipolar spin ice," *Physical Review Letters*, vol. 106, no. 5, p. 057209, 2011.

[54] S. Zhang *et al.*, "Crystallites of magnetic charges in artificial spin ice," *Nature*, vol. 500, no. 7464, pp. 553–557, 2013.

[55] B. Canals *et al.*, "Fragmentation of magnetism in artificial kagome dipolar spin ice," *Nature communications*, vol. 7, no. 1, pp. 1–6, 2016.

[56] Y. Perrin, B. Canals, and N. Rougemaille, "Extensive degeneracy, Coulomb phase and magnetic monopoles in artificial square ice," *Nature*, vol. 540, 2016.

[57] O. Sendetskyi *et al.*, "Magnetic diffuse scattering in artificial kagome spin ice," *Physical Review B*, vol. 93, no. 22, p. 224413, 2016.

[58] A. Farhan *et al.*, "Emergent magnetic monopole dynamics in macroscopically degenerate artificial spin ice," *Science advances*, vol. 5, no. 2, p. 6380, 2019.

[59] G. Möller and R. Moessner, "Magnetic multipole analysis of kagome and artificial spin-ice dipolar arrays," *Physical Review B*, vol. 80, no. 14, p. 140409, 2009.

[60] G.-W. Chern, P. Mellado, and O. Tchernyshyov, "Two-stage ordering of spins in dipolar spin ice on the kagome lattice," *Phys. Rev. Lett.*, vol. 106, p. 207202, 2011.

[61] Y. Qi, T. Brintlinger, and J. Cumings, "Direct observation of the ice rule in an artificial kagome spin ice," *Physical Review B*, vol. 77, no. 9, p. 094418, 2008.

[62] J. Colbois *et al.*, "Artificial out-of-plane ising antiferromagnet on the kagome lattice with very small farther-neighbor couplings," *Physical Review B*, vol. 104, no. 2, p. 024418, 2021.

[63] V. Schánilec *et al.*, "Bypassing dynamical freezing in artificial kagome ice," *Physical Review Letters*, vol. 125, 2020.

[64] L. Anghinolfi, H. Luetkens, J. Perron, M. Flokstra, O. Sendetskyi, A. Suter, T. Prokscha, P. Derlet, S. Lee, and L. Heyderman, "Thermodynamic phase transitions in a frustrated magnetic metamaterial," *Nature communications*, vol. 6, no. 1, pp. 1–6, 2015.

[65] M. E. Brooks-Bartlett *et al.*, "Magnetic-moment fragmentation and monopole crystallization," *Physical Review*, vol. 4, 2014.

[66] J. C. Gartside *et al.*, "Realization of ground state in artificial kagome spin ice via topological defect-driven magnetic writing," *Nature Nanotechnology*, vol. 13, 2018.

[67] N. Rougemaille *et al.*, "Chiral nature of magnetic monopoles in artificial spin ice," *New Journal of Physics*, vol. 15, no. 3, p. 035026, 2013.

[68] S. Gliga *et al.*, "Spectral analysis of topological defects in an artificial spin-ice lattice," *Physical review letters*, vol. 110, no. 11, p. 117205, 2013.

[69] V. Nguyen *et al.*, "Competing interactions in artificial spin chains," *Physical Review B*, vol. 96, no. 1, p. 014402, 2017.

[70] Y. Perrin, B. Canals, and N. Rougemaille, "Quasidegenerate ice manifold in a purely two-dimensional square array of nanomagnets," *Physical Review B*, vol. 99, no. 22, p. 224434, 2019.

[71] K. Zeissler, S. Walton, S. Ladak, D. Read, T. Tyliszczak, L. Cohen, and W. Branford, "The non-random walk of chiral magnetic charge carriers in artificial spin ice," *Scientific reports*, vol. 3, no. 1, pp. 1–7, 2013.

[72] D. Sanz-Hernández *et al.*, "Tunable stochasticity in an artificial spin network," *Advanced Materials*, vol. 33, no. 17, p. 2008135, 2021.

[73] K. Omari *et al.*, "Toward chirality-encoded domain wall logic," *Advanced Functional Materials*, vol. 29, no. 10, p. 1807282, 2019.

[74] H. Arava *et al.*, "Engineering relaxation pathways in building blocks of artificial spin ice for computation," *Physical Review Applied*, vol. 11, no. 5, p. 054086, 2019.

[75] W. Yue *et al.*, "Crystallizing kagome artificial spin ice," *Physical Review Letters*, vol. 129, no. 5, p. 057202, 2022.

[76] S. Kempinger *et al.*, "Imaging the stochastic microstructure and dynamic development of correlations in perpendicular artificial spin ice," *Physical Review Research*, vol. 2, no. 1, p. 012001, 2020.

[77] R. J. Baxter, *Exactly solved models in statistical mechanics*. Elsevier, 2016.

[78] O. Sendetskyi *et al.*, "Continuous magnetic phase transition in artificial square ice," *Physical Review B*, vol. 99, no. 21, p. 214430, 2019.

[79] E. H. Lieb, "Exact solution of the problem of the entropy of two-dimensional ice," *Physical Review Letters*, vol. 18, no. 17, p. 692, 1967.

[80] R. Baxter, "Spontaneous staggered polarization of thef-model," *Journal of Statistical Physics*, vol. 9, no. 2, pp. 145–182, 1973.

[81] J. C. Slater, "Theory of the transition in kh2po4," *The Journal of Chemical Physics*, vol. 9, no. 1, pp. 16–33, 1941.

[82] J. Nagle, "Proof of the first order phase transition in the slater kdp model," *Communications In Mathematical Physics*, vol. 13, no. 1, pp. 62–67, 1969.

[83] M. Zinkin and M. Harris, "Local mean field calculation of the frustrated pyrochlore spin structure," *Journal of magnetism and magnetic materials*, vol. 140, pp. 1803–1804, 1995.

[84] C. Henley, "Power-law spin correlations in pyrochlore antiferromagnets," *Physical Review B*, vol. 71, no. 1, p. 014424, 2005.

[85] C. Nisoli, "Topological order of the rys f-model and its breakdown in realistic square spin ice: Topological sectors of faraday loops," *Europhysics Letters*, vol. 132, no. 4, p. 47005, 2020.

[86] J. Porro *et al.*, "Exploring thermally induced states in square artificial spin-ice arrays," *New Journal of Physics*, vol. 15, no. 5, p. 055012, 2013.

[87] Z. Budrikis *et al.*, "Domain dynamics and fluctuations in artificial square ice at finite temperatures," *New Journal of Physics*, vol. 14, no. 3, p. 035014, 2012.

[88] C. Phatak *et al.*, "Nanoscale structure of the magnetic induction at monopole defects in artificial spin-ice lattices," *Physical Review B*, vol. 83, no. 17, p. 174431, 2011.

[89] S. Pollard, V. Volkov, and Y. Zhu, "Propagation of magnetic charge monopoles and dirac flux strings in an artificial spin-ice lattice," *Physical Review B*, vol. 85, no. 18, p. 180402, 2012.

[90] C. Nisoli, "Effective temperature in an interacting vertex system: theory and experiment on artificial spin ice," *Physical review letters*, vol. 105, no. 4, p. 047205, 2010.

[91] Z. Budrikis, P. Politi, and R. Stamps, "Diversity enabling equilibration: disorder and the ground state in artificial spin ice," *Physical review letters*, vol. 107, no. 21, p. 217204, 2011.

[92] R. Möller, G. Moessner, "Artificial square ice and related dipolar nanoarrays," *Physical Review Letters*, vol. 96, 2006.

[93] O. Brunn, Y. Perrin, B. Canals, and N. Rougemaille, "Signatures of farther neighbor couplings in artificial square ice," *Physical Review B*, vol. 103, no. 9, p. 094405, 2021.

[94] E. Östman *et al.*, "Interaction modifiers in artificial spin ices," *Nature Physics*, vol. 14, no. 4, pp. 375–379, 2018.

[95] V. Schánilec *et al.*, "Approaching the topological low-energy physics of the f model in a two-dimensional magnetic lattice," *Physical Review Letters*, vol. 129, no. 2, p. 027202, 2022.

[96] J. M. Kosterlitz and D. J. Thouless, "Ordering, metastability and phase transitions in two-dimensional systems," *Journal of Physics C: Solid State Physics*, vol. 6, no. 7, p. 1181, 1973.

[97] D. M. Arroo and S. T. Bramwell, "Experimental measures of topological sector fluctuations in the f-model," *Physical Review B*, vol. 102, no. 21, p. 214427, 2020.

[98] S. H. Skjærvø, , *et al.*, "Advances in artificial spin ice," *Nature Reviews Physics*, vol. 2, no. 1, pp. 13–28, 2020.

[99] X. Zhang *et al.*, "Emergent strings in santa fe artificial spin ice," in *APS March Meeting Abstracts*, vol. 2021, pp. C39–003, 2021.

Appendices

Appendix A - Mumax^3 simulation scripts

Kagome vertex with notch

The following script shows simulation parameters for the notch rule-obeying spin configuration for the kagome vertex with the notch. The script contains one cycle for x, which is the *depth of the notch* parameter, starting from $x = 0$ to $x = 300\,\text{nm}$ with step $50\,\text{nm}$. The script is copyable, but some special characters need to be fixed. To change the script to simulate the notch rule-breaking configuration, change the magnetisation of regions 1 and 3.

```
//Mesh properties-----------------------------------------------
Nx := 1024;
Ny := 1024;
Nz := 1;

sizeX := 2048e-9;
sizeY := 2048e-9;
sizeZ := 25e-9;

SetGridSize(Nx, Ny, Nz);
SetCellSize(sizeX/Nx, sizeY/Ny, sizeZ/Nz);

//structure-----------------------------------------------------
w:=250e-9;                  //width
lg:=750e-9;                 //length

//notch---------------------------------------------------------
x:=0e-9;                 //Depth of  the  notch
alf:=(30*pi/180);         //angle of the  notch

//simulation properties-----------------------------------------
smu:=5;
stime:=10e-9;

//image output--------------------------------------------------
k:=50;
m_crop:=crop(m,k,Nx-k,k,Ny-k,0 ,Nz);
MFMLift=80e-9;
MFM_crop:=crop(MFM,k,Nx-k,k,Ny-k,0 ,Nz);

//table settings------------------------------------------------
tableaddvar(smu, "Smooth", " ");
tableaddvar(lg, "Length", "m");
tableaddvar(k, "Crop", "pix");
tableaddvar(stime, "simulation time", "s");
tableaddvar(alf,"Top angle","rad");
tableaddvar(x,"Dent depth","m");
tableadd(E_exch);
tableadd(E_demag);
tableadd(E_total);
```

```
//==============================================================
//Core of simulation
EdgeSmooth = smu;

//kagome structure
l:=lg+1/3*(w*cos(30*pi/180));
bary:=((rect(w,l)).add(circle(w).transl(0,l/2,0))).transl(0,l/2,0);
barrr:=bary.rotz(-120*pi/180);
barrl:=bary.rotz(120*pi/180)
barrrl:=barrr.add(barrl);
kagome:=barrrl.add(bary);

for x; x<301e-9; x=x+50e-9{
     print(x);
     //alf:=(30*pi/180)
//for alf; alf<(96*pi/180); alf=alf+(30*pi/180){

veta:=(120*pi/180-alf/2+30*pi/180);
qwe:=tan(60*pi/180)/sin(alf/2)-1/sin(veta);
xx:=(x/sin(veta))/qwe;

b:=xx+x;
a:=xx*tan(60*pi/180)*2;
base:=rect(a,b);
c:=sqrt(a*a/4+b*b);
alp:=asin(a/(2*c));
trir:=rect(c,c).rotz(alp).transl(a/4+c/2*cos(alp),c/2*sin(alp),0);
tril:=rect(c,c).rotz(-alp).transl(-a/4-c/2*cos(alp),c/2*sin(alp),0);
notch:=base.sub(trir).sub(tril).transl(0,-2/3*w*sin(60*pi/180)+b/2-a/2*tan(30*pi/180),0);

kanotch:=(kagome.sub(notch)).transl(0,-l/6,0);

setgeom(kanotch);

//Definition of regions
defregion(3, (rect(w,3/2*l).transl(0,l/2,0)).transl(0,-l/6,0));
defregion(1,bary.rotz(-120*pi/180).transl(0,-l/6,0));
defregion(2,bary.rotz(120*pi/180).transl(0,-l/6,0));
defregion(4,rect(3/2*w,3/2*w).transl(0,-l/6,0));
defregion(5,circle(1.2*w).transl((l)*cos(30*pi/180),-l/6-(l)*sin(30*pi/180),0));
defregion(6,circle(1.2*w).transl(-(l)*cos(30*pi/180),-l/6-(l)*sin(30*pi/180),0));
defregion(7,circle(1.2*w).transl(0,-l/6+(l),0));

save(regions);

//material
Msat  = 800e3;
Aex   = 10e-12;
alpha = 0.4;


//Region's magnetzation
m.setRegion(1, uniform(1, -1, 0));        //right
m.setRegion(2, uniform(-1, -1, 0));         //left
m.setRegion(3, uniform(0, -1, 0));         //up
m.setRegion(4,RandomMag())
```

```
m.setRegion(5, uniform(1*cos(30*pi/180), -1*sin(30*pi/180), 0));
m.setRegion(6, uniform(-1*cos(30*pi/180), -1*sin(30*pi/180), 0));
m.setRegion(7, uniform(0, -1, 0));

frozenspins.setRegion(5, 1)
frozenspins.setRegion(6, 1)
frozenspins.setRegion(7, 1)
//Simulation
relax();

run(stime);
snapshot(m_crop);
snapshot(MFM_crop);
tablesave();
 RandomMag()
//}
}
```

Square vertex with hole

An example of the script used to simulate the square vertex with the hole is shown below. The script simulates Type I vertex configuration and calculates its energy for different sizes of the hole. The parameter c is the hole diameter, and the script contains one cycle for the c going from 0 nm to 120 nm with a 5 nm step. To change the vertex configuration, you must edit the magnetisation of regions $1 - 4$, which represent the magnetisation of individual nanomagnets and $6 - 9$, which freezes the spins at the end of nanomagnets, to prevent unwanted switching.

```
Nx := 512;
Ny := 512;
Nz := 1;

sizeX := 512e-9;
sizeY := 512e-9;
sizeZ := 25e-9;

w:=100e-9;
l:=512e-9;
c:=0e-9;
k:=60;

smu:=5;
stime:=5e-9;

SetGridSize(Nx, Ny, Nz);
SetCellSize(sizeX/Nx, sizeY/Ny, sizeZ/Nz);

m_cropfive:=crop(m,k,Nx-k,k,Ny-k,0 ,Nz);
MFM_cropfive:=crop(MFM,k,Nx-k,k,Ny-k,0 ,Nz);
EdgeSmooth = smu;

//table settings
tableaddvar(smu, "Smooth", " ");
tableaddvar(stime, "simulation time", "s");
tableaddvar(c, "Hole_diam", "nm");
tableadd(E_exch);
tableadd(E_demag);
tableadd(E_total);


for c; c<121e-9; c=c+5e-9{
     //print(c);

      barx:=rect(2*l,w);
      bary:=rect(w,2*l);
      circ:=circle(c);

      vert:=barx.add(bary);
      verth:=vert.sub(circ);
      setgeom(verth);


       defregion(1, rect((2*l-w)/2,w).transl((2*l+w)/4,0,0));
       defregion(2, rect((2*l-w)/2,w).transl(-(2*l+w)/4,0,0));
```

```
    defregion(3, rect(w,(2*l-w)/2).transl(0,(2*l+w)/4,0));
    defregion(4, rect(w,(2*l-w)/2).transl(0,-(2*l+w)/4,0));
    defregion(5, rect(w,w));

    defregion(6, rect((2*l-w)/2,w).transl((2*l+w)/2.4,0,0));
    defregion(7, rect((2*l-w)/2,w).transl(-(2*l+w)/2.4,0,0));
    defregion(8, rect(w,(2*l-w)/2).transl(0,(2*l+w)/2.4,0));
    defregion(9, rect(w,(2*l-w)/2).transl(0,-(2*l+w)/2.4,0));
    save(regions);

    //permalloy
    Msat   = 800e3;
    Aex    = 10e-12;
    alpha = 0.5;


    //Vertex simulation
    m.setRegion(1, uniform(1, 0, 0));           //right wing
    m.setRegion(2, uniform(-1, 0, 0));           //left wing
    m.setRegion(3, uniform(0, -1, 0));           //up wing
    m.setRegion(4, uniform(0, 1, 0));           //down wing
    m.setRegion(5, RandomMag());
    m.setRegion(6, uniform(1, 0, 0));           //right wing
    m.setRegion(7, uniform(-1, 0, 0));           //left wing
    m.setRegion(8, uniform(0, -1, 0));           //up wing
    m.setRegion(9, uniform(0, 1, 0));           //down wing

    frozenspins.setRegion(6, 1)
    frozenspins.setRegion(7, 1)
    frozenspins.setRegion(8, 1)
    frozenspins.setRegion(9, 1)

    MFMLift=80e-9;
    relax();


    //snapshot(m);
    //snapshot(MFM);
    run(stime);
    snapshot(m_cropfive);
    snapshot(MFM_cropfive);
    tablesave();

}
```

Appendix B - Fabrication procedure: lattice with holes

Sample fabrication procedure of the square system with holes arrays was done partially in Nanofab Institut Néel and partially at CEITEC Brno University of Technology:

a) **Preliminaries** - The cleaning of the substrate was done to remove impurities from the surface. The silicone substrate was first exposed to an ultrasonic bath in acetone for 3 minutes at room temperature. Secondly, it was exposed to another ultrasonic bath in isopropyl alcohol (IPA) to remove the acetone on the surface. After that, the sample was placed on a hot plate for 1 minute at the temperature 150 °C to remove any droplets from the surface.

b) **Spin-coating of resist layer** - Positive resist PMMA 2% was spin-coated onto the sample. To achieve a thickness of resist around $120 - 150$ nm spin-coating speed of the rotation was 4000 rpm with an acceleration 4000 rpm/s for 60 s. After the resist was applied, the sample was placed on the hot plate for 5 minutes at the temperature of 180 °C to strengthen the resist.

c) **Resist exposure** - For resist exposition, we used lithograph *Nanobeam Nb5*. The nominal dosage was $10\,\mathrm{C/m^2}$ with the step size and current optimised for fast and precise exposure. Nominal values of nanoisland parameters were length 500 nm; width 100 nm and hole diameter $0-155$ nm. Each lattice is made by 30×30 vertices.

d) **Development of the resist** - The sample was first immersed into MIBK:IPA 1:3 for 60 s to remove the exposed resist after the development sample was risen in demi-water and dried by nitrogen.

e) **NiFe deposition** - The next step was to deposit 25 nm of the NiFe layer onto the sample. The deposition was done in *Electron beam evaporator BESTEC* at CEITEC BUT.

f) **Lift-off** - The last step of the sample fabrication procedure is removing the rest of the resist together with all material deposited on it. The sample was put into a solvent compatible with the chosen resist to dissolve unexposed resist. The lift-off procedure was done in an hourglass with the sample lying upside down, so the gravity helps remove the unexposed resist.

Special thanks belong to my colleague Ondřej Brunn, who helped me with the sample fabrication, especially with lithograph operations.

Appendix C - Type III vertex movement

While the square spin system is in the low-energy phase, where the Type III defects are confined to the FL, their movement is severely limited. In Figure 21 a) there is a detail of MFM figure capturing two FLs joined together by two Type III defects. The measured vertex configuration and hypothetical situation of how the black Type III vertex should move to transform the blue Faraday line into the red one are shown in Figure 21 b), c) and d).

The movement of the defect is, in this case, caused by the spin flips, which does not increase the system's total energy. Only spin flips resulting in the same or lower number of type II vertices are allowed. Three different snapshots, capturing different stages of the defect movement together with the total vertex population, shows how the transformation process would look. It can be seen that as the defect moves, the number of Type II vertices decreases. Thus the movement of the defect lowers the total energy of the system.

Since the loop spin flips (collective switching of join spins) are not possible in the real system, the defect movement like the one depicted in Figure 21 is the closes to the loop flip event we can get.

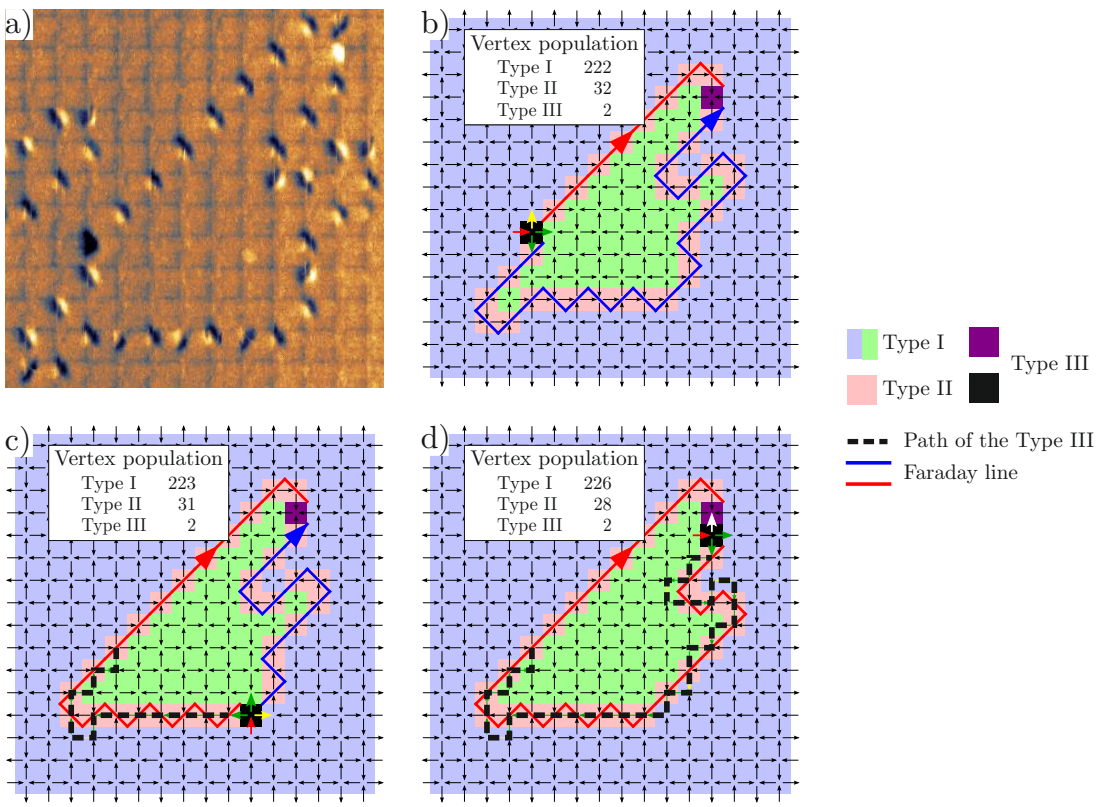

Figure 21: a) Measured pair of FLs connected by two type III defects.The hypothetical movement of the black type III defect in following the path of the least energy resulting in the transformation of blue FL in the red one. Three snapshots of the process together with the vertex population of the system are shown in b), c) and d). Taken and edited from [95].

List of abbreviations

AFM	Atomic force microscopy
AM	Antiferromagnet/ic
DW/DWs	Domain wall/s
EBL	Electron beam lithography
EBPVD	Electron beam physical vapour deposition
FL/FLs	Faraday line/s
FM	Ferromagnetic
HH	Helmholtz-Hodge
kdIa	Kagome dipolar Ising antiferromagnet
kdsi	Kagome dipolar spin ice
kIa	Kagome Ising antiferromagnet
kmIf	Multi-axial kagome system
ksi	Kagome spin ice
LRO	Long range order phase
L-TEM	Lorentz transmission electron microscopy
MFM	Magnetic force microscopy
MSF	Magnetic structure factor
PEEM	Photoelectron emission microscopy
PM	Paramagnetic phase
SEM	Scanning electron microscopy
SL1	Spin liquid 1 phase
SL2	Spin liquid 2 phase
SPM	Scanning probe microscopy